Title
Next-Generation Isotope Production via Deuteron Breakup

Author
Morrell, Jonathan

Publication Date
2021

Peer reviewed|Thesis/dissertation

Next-Generation Isotope Production via Deuteron Breakup

by

Jonathan Morrell

A dissertation submitted in partial satisfaction of the

requirements for the degree of

Doctor of Philosophy

in

Engineering - Nuclear Engineering

in the

Graduate Division

of the

University of California, Berkeley

Committee in charge:

Professor Lee A. Bernstein, Chair
Professor Rebecca Abergel
Professor Karl van Bibber
Professor Paul Renne

Spring 2021

Next-Generation Isotope Production via Deuteron Breakup

Abstract

Next-Generation Isotope Production via Deuteron Breakup

by

Jonathan Morrell

Doctor of Philosophy in Engineering - Nuclear Engineering

University of California, Berkeley

Professor Lee A. Bernstein, Chair

As part of the next generation of cancer treatment, targeted alpha therapy (TAT) has demonstrated the potential to improve patient outcomes by targeting cancer cells with highly cytotoxic α-emitters. These are prized for their ability to efficiently kill cancer cells, while dealing minimal damage to nearby healthy tissue. When properly paired with a positron-emitting radionuclide, a rapid bio-assay of the therapeutic agent can be performed using positron emission tomography (PET), enabling micro-dosimetry and personalized treatment planning. One of the main challenges associated with these treatments is the production of the α-emitting radionuclides in quantities which are relevant to widespread clinical use.

In this work, we seek to improve the understanding of the isotope production pathways for ^{225}Ac, one promising candidate for TAT, and ^{134}Ce, which is a positron-emitting analog of actinium. The main pathway which we explored was through the ^{226}Ra(n,2n) reaction, which produces the ^{225}Ac generator isotope ^{225}Ra. Thick target deuteron breakup was utilized as a high intensity, variable energy neutron source for inducing this reaction.

A parameterized hybrid model for the double differential neutron spectra from thick target deuteron breakup was developed, and the optimal parameters for the model were determined through a fit to selected literature data. Measurements of the spectrum were performed on a beryllium target at 33 and 40 MeV deuteron energies, using the activation and time-of-flight techniques, and these measurements were compared to the hybrid model and literature data. Additionally, production cross sections for several other emerging radionuclides were measured using the activation technique, with the deuteron breakup neutrons.

The ^{226}Ra(n,2n) reaction cross section was measured with the breakup spectra from 33 and 40 MeV deuterons on beryllium, using the activation method and α spectroscopy. These measurements were compared to the predictions of the TENDL-2015 and ENDF/B-VII.1 evaluations. A chemical separation of the produced ^{225}Ac was performed following both

irradiations, to evaluate the separation capabilities of the DGA and AG50 cation exchange resins, as well as to search for any co-produced impurities such as ^{227}Ac or fission products.

Additionally, measurements of the ^{139}La(p,6n)^{134}Ce cross sections from 35–60 MeV were performed using the stacked-foil activation technique. Thick target yield calculations showed this to be a promising pathway for ^{134}Ce production, which is a positron-emitting chemical analog to ^{225}Ac. Several other ^{139}La(p,x) reaction channels were also measured, which are useful for quantifying impurities and for evaluating nuclear reaction models. These measurements were compared to the predictions of the TALYS, EMPIRE and ALICE nuclear reaction codes, which showed that the default pre-equilibrium models were insufficient, providing motivation for further study of these processes.

Finally, a comparison study was performed between several of the most promising ^{225}Ac production routes. The ^{232}Th(p,x)^{225}Ac pathway showed generally good yields, but was shown to contain significant ^{227}Ac, which may have negative long term side-effects, depending on the bio-chemistry of the complexed actinium molecule. The ^{232}Th(p,4n)^{229}Pa pathway had a high purity, but poor yields. Pathways involving directly irradiating ^{226}Ra targets with charged particles or photons were shown to have engineering issues regarding target heating, that must be overcome if they are to be pursued further. And the ^{226}Ra(n,2n) pathway using secondary neutrons from deuteron breakup was shown to have high purity, and had yields comparable to ^{232}Th(p,x) if a radium target of 10–50 grams is used.

The primary goals of this thesis are to improve the understanding of deuteron breakup, both through measurements and modeling, and to highlight its potential applicability for isotope production purposes. It is the hope that this will inspire a more widespread adoption of technology utilizing deuteron breakup as a neutron source, and will lead to an improvement in the supply of ^{225}Ac available for research and clinical applications.

Contents

List of Figures

List of Tables

Acknowledgments

Foremost, I would like to express my deepest thanks to my advisor, Dr. Lee Bernstein, without whom this work would not have been possible. Lee has been a true mentor to me, and has served as a constant source of guidance, inspiration, encouragement and support. His personality is infectious, and his love for science, discovery and teaching are clear to everyone around him. Lee has been a friend to me, and has opened countless doors through which I've found new opportunities for scientific exploration, personal growth, and professional development. I have him to thank for introducing me to the isotope production team at Los Alamos National Lab, with whom I am excited to soon be joining as a post-doctoral researcher. Lee gave me the opportunity to teach in NE 101, which was a tremendous pleasure, boosting my confidence in my own knowledge and abilities, and teaching me how to teach, which is a skill that I have grown to thoroughly appreciate. Through Lee I've been introduced to hundreds of esteemed nuclear scientists and engineers around the world, and have been given the opportunity to present my work in front of them. I can't thank him enough for this, and I'm sure I've only seen the start of the benefits that I will reap from these interactions. Finally, Lee has always made himself available. Whether it's answering a simple question, or engaging in an hours long scientific discussion, Lee has always been excited to help me in my work, and I can't thank him enough for his guidance. I hope that this isn't the end, but rather a new beginning in our collaboration and friendship.

I also must express an extreme amount of gratitude to the other members of my thesis committee: Dr. Karl van Bibber, Dr. Paul Renne, and Dr. Rebecca Abergel. Karl and Paul, it was a pleasure working with you on the geochronology project at the HFNG. While you may claim to have brought me on because of my "previous experience", I can assure you that I left that project with infinitely more. It was a load of work, and a load of fun, and I'm incredibly grateful that I was able to contribute in a meaningful way. I can't wait to see what the future holds for the HFNG. Rebecca, you also deserve my personal thanks for your contribution to the actinium production experiment forming the basis of chapter 4. That experiment would not have succeeded without the work performed at HERL, which couldn't have happened without you. I also need to thank all four of you for the extreme amount of patience, guidance and effort which you have provided me for the completion of this dissertation. This work was a great challenge for me, and I couldn't have completed it without you.

I also need to thank the scientists, engineers, operators and support staff of the 88-Inch Cyclotron and the Heavy-Elements Research Lab (HERL) who enabled me to collect the experimental data needed for the completion of this work. Brien Ninemire, Nick Brickner, Tom Gimpel, Scott Small and Devin Thatcher: thank you all for providing a reliable beam for these experiments. Many of these beams set new performance records for the recent history

of the machine, and you all rose to the occasion admirably. In addition to Dr. Abergel, I'd like to thank Wayne Lukens, Korey Carter and Kathy Shield, who were all extremely helpful in performing the alpha spectroscopy and chemical separations at HERL. I'm also indebted to Saed Mirzadeh and Justin Griswold of Oak Ridge National Laboratory for supplying the radium used in our experiments.

I would also like to acknowledge the funding sources for my time, as well as the materials and cyclotron beamtime required to perform these experiments. This research was supported by the Isotope Program within the U.S. Department of Energy's Office of Science, carried out under Lawrence Berkeley National Laboratory (Contract No. LAB16-1588 NSD).

Within the nuclear data group, so many of you have helped me along the way. I want to thank Jon Batchelder, for lending his expertise and insight, and for helping with the hands-on work in almost every portion of this dissertation. I want to thank Josh Brown and Thibault Laplace for their contributions to the time-of-flight measurements, and their guidance in the analysis and interpretation of my results. Shamsuzzoha Basunia, your attention to detail is noteworthy, and was invaluable in the analysis of the lanthanum results. I also want to thank Bethany Goldblum, Darren Bluel and Aaron Hurst for their knowledge and valuable discussions.

Among my fellow graduate students, I want to thank you all for your friendship, support, and your assistance in this work: Amanda Lewis, Morgan Fox, Eric Matthews, Catherine Apgar, Austin Lo, Mauricio Unzueta, Mitch Negus, Sami Lewis, Maria Simanovskaia, Tyler Bailey, Josh Rehak, Joey Gordan, Jason Matheny, Christopher Brand, Justin Ellin, Franziska Schmidt, Tyler Nagel, and many others. I wish you all the best, and hope to continue working with you in the future. I would also like to thank all the students and staff who worked with me on the HFNG project. The experience I gained from that role was invaluable to my completion of this dissertation.

I owe a special debt of gratitude to Andrew Voyles, who has been both a friend and a mentor to me during my time here in Berkeley. Upon my arrival in Berkeley in 2017, Andrew quickly brought me up to speed with all of the finer details in stacked-target activation analysis, gamma spectroscopy, target preparation and characterization, and with all the state-of-the-art techniques in isotope production. Andrew spent many long nights helping to ensure that my experiments were set up and running successfully, and I would not be where I am today without his contributions. I hope that our collaborations will continue well into the future.

On a personal note, I want to thank my partner, Patricia Dominguez, for her support during this time. Your patience, kindness, and baked goods were all invaluable in my success. I can't thank you enough for your encouragement, and for helping me to stay focused and on track. To my roommate, Dagin Faulkner, thanks for putting up with me during this time, and for introducing me to the art of photography. You've been a great friend over the years.

Finally, I wish to thank my family for their love, support and encouragement throughout my entire life. To my parents, you made me who I am today, and I couldn't be more grateful. You taught me good working habits, many practical skills, and you've opened so many doors for me. To my brother Josh, you've always been my best friend, and I can't wait to see what's in store for your future. I wouldn't have gotten to this point without the three of you.

In closing, I present this work not alone, but rather standing on the shoulders of giants, to whom I am most grateful. It is because of the hard work, support, encouragement, inspiration and love of these people, and so many others, that any of this is possible.

Thank you all.

Jonathan T. Morrell
Berkeley, CA
May 2021

Chapter 1

Introduction

Since the first synthesis of monoclonal antibodies in 1975 and their first clinical use in 1986, much effort has been put into combating a broad range of diseases and conditions using this novel class of therapeutics [1]. As of 2014, the global antibody market was estimated at over $20 billion (USD), with over 30 monoclonal antibodies authorized for clinical use by the FDA [1]. The synthetically derived molecules mimic antibodies produced by the body's immune system to allow targeting of specific proteins expressed by various diseases. In combination with recent advances in genetic sequencing and computational biology, monoclonal antibody development has opened the doors to truly *personalized medicine*, enabling the treatment of diseases that may have previously been incurable, and with fewer adverse side-effects.

Unfortunately for cancer treatment, antibody therapy alone is rarely if ever curative, and is currently quite expensive [2]. This is due to the fact that most antibody treatments are not highly effective at killing the cancerous cells directly, but rather act by inhibiting their growth or preventing them from spreading [3]. This is changed dramatically, however, by binding the monoclonal antibody to a highly cytotoxic alpha-emitting radionuclide, which is much more effective at cell killing. This class of treatment is called targeted alpha therapy (TAT), which has demonstrated the potential for complete remission of even advanced, metastatic cancers [4]. Alpha-emitting radionuclides in particular are preferred over other (β/γ-emitting) radionuclides for therapeutic applications, because of their high linear energy transfer (LET) and short range. If properly targeted, TAT isotopes will do great damage to cancer cells within their ≈ 50 µm range, and spare the surrounding healthy tissue.

Another key component of targeted radionuclide therapy is the ability to image the progression or remission of a disease, as treatment is successively applied. Again taking advantage of the targeting capability of monoclonal antibodies, β^+-emitting isotopes can be delivered to disease sites within the body and imaged with positron emission tomography

(PET). The option to use a rapid-assay technique such as targeted-PET could, for example, allow a clinician to adjust the dosage of the therapeutic isotope based on the total mass of disease observed in the PET scan, thus mitigating side-effects by sparing healthy tissue. Because the most promising α-emitting therapeutic isotopes do not have any positron-emitting isotopes in their decay chain (with the singular exception of ^{149}Tb), performing this type of targeted-PET wherein the same antibody is used for imaging and treatment will require the use of PET isotopes which behave as chemical analogs to the appropriate TAT isotope. For example, the TAT isotope ^{211}At is a halogen, and could be used in conjunction with other (positron-emitting) radiohalogens such as ^{124}I or ^{18}F [5–7].

The high specificity and broad appeal of this treatment modality means that specific sets of isotopes may need to be carefully selected for different applications. There are a wide variety of FDA approved monoclonal antibody treatments for almost every major type of cancer [8], many of which have the potential to be used as a targeting vector in targeted alpha therapy. In light of this, no single TAT isotope is likely to be a "silver bullet" for cancer treatment, and a broad portfolio of radioisotopes in high availability will certainly be required to enable this next generation of therapy.

While the need for the availability of such isotopes is certainly clear, and will likely increase significantly in the future, the supply for therapeutic α-emitters is mostly limited to small doses for the purposes of clinical trials and R&D [9]. There are many challenges associated with producing α-emitters. There is the product itself, which is generally quite dangerous to handle. Virtually all α-emitters have atomic number greater than $Z = 83$ (bismuth), which makes finding a suitable production target challenging as there are no stable elements higher than bismuth. If thorium or uranium are chosen as targets, the effects of fission have to be considered, both in terms of radiopurity and safety. Some production pathways may require the use of exotic or high-energy beams, requiring specialized, expensive accelerators. In addition to the production challenges, the lack of stable isotopes makes separation and purification difficult, as the chemistry of these heavy elements may not be well understood, requiring further research.

Bearing these challenges in mind, it is the goal of this dissertation to improve the understanding of several of these production pathways. The first pathway studied was the production of the ^{134}Ce/^{134}La system through the ^{139}La(p,6n) reaction. This system is a potential *in vivo* positron generator, that can act as a chemical analog to the TAT isotopes ^{225}Ac and ^{227}Th. The next was the production of the therapeutic isotope ^{225}Ac through the (n,2n) reaction on ^{226}Ra, using a thick-target deuteron breakup neutron source. This elicited further study of other radionuclides that could be produced via deuteron breakup, such as ^{64,67}Cu and ^{44,47}Sc. Finally, the ^{226}Ra(n,2n) pathway for ^{225}Ac production was compared to several other pathways currently under development. It is the hope that this work will improve upon the nuclear data essential to optimizing these pathways, and enhance the

capabilities of isotope production centers to meet the present and future demand for this promising new paradigm of treatment.

1.1 Motivation

Targeted alpha therapeutics have demonstrated the potential to be highly efficacious at treating advanced, metastatic cancers, which are otherwise resistant to conventional therapy [10]. Conventional radiation therapy, in which an external x-ray beam is focused upon the cancer site, as well as chemotherapy, target cancer in a similar fashion. Both methods target rapidly dividing cells, and the treatment schedule is often timed to kill cells during a specific phase of the cycle, although some chemotherapy is considered cell-cycle nonspecific [11]. This is done to avoid the DNA repair checkpoints in the cell cycle. The drawback to these treatment methods is that the specificity is poor, and there is a high likelihood of damaging healthy tissue. This is particularly problematic for tissues with a cell-cycle time similar to the cancerous cells, as these are preferentially targeted by both methods, leading to severe side-effects.

For chemotherapy, there are many mechanisms by which cancer cells may become resistant to treatment [12]. For conventional radiation therapy, there are two main limitations. Perhaps the most obvious is that if a cancer metastasizes, an external x-ray beam simply cannot be focused on all of the tumors. The other limitation is that x-rays have a low linear energy transfer (LET), and below extreme doses will only damage cancer cells through single-strand breaks (SSBs) to the DNA. These can be enzymatically repaired by the cancer, which could prevent complete remission [12].

There are a number of advantages to targeted alpha therapy over conventional methods. The most important, particularly for metastatic cancers, is the targeting specificity. Even if only 1% of the targeting molecules bind to tumor cells, the overall dose to cancerous tissue will be much greater than a treatment with no specificity, as the cancer cells only make up such a small fraction of the total body mass. Alpha-emitting radionuclides are particularly attractive in combination with a targeting vector because alphas are a high-LET radiation. In the energy range relevant to nuclear medicine, alphas induce a far higher density of ionization along a given path length than electrons or photons. One possible exception is for Auger electrons, with energies on the order of 10 eV–10 keV. However Auger electrons have such a short range that they must be within the cell nucleus itself to damage DNA, and therefore require different targeting mechanisms than monoclonal antibodies, which bind to the cell surface [13]. Fast neutrons are also generally considered densely ionizing, as they will transfer energy (in the body) to protons through elastic scattering, which themselves are densely ionizing. Their path length is, however, too long to be of practical use, and

there are certainly no neutron emitting radionuclides with lifetimes compatible with targeted therapy. Boron neutron capture therapy, where the breakup of ^{11}B and ^{12}C (formed by neutron capture) into high-LET massive particles offers an attractive alternative, but efforts to introduce sufficient boron doping at tumor cells have had limited success [14].

The high ionization density of alpha particles causes them to induce double-strand breaks (DSBs) in DNA, significantly increasing the cell lethality as DSBs are much less likely to be repaired than SSBs [15]. Figure 1.1 gives a representative cell-survival curve, showing the effects of LET on the cell lethality. The two most significant features differentiating the two curves are that high-LET radiation, such as alphas, have a much higher lethality for a given dose rate than low-LET radiation, and that the relationship is linear for high-LET radiation and non-linear for low-LET radiation.

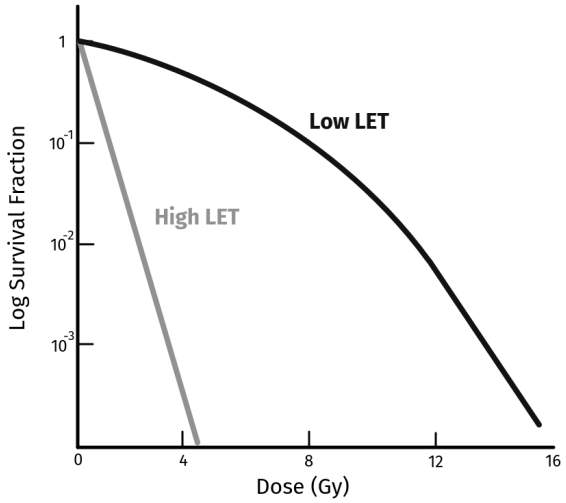

Figure 1.1: Representative cell survival curves for low and high LET radiation.

The fact that alphas are much more lethal means a smaller activity of α-emitting radionuclides are needed to kill the same proportion of cells as β/γ emitters. This effect is compounded by the much smaller range of alphas, which increases the local dose rate per decay by decreasing the volume (and mass) over which the energy is deposited. This is advantageous from a treatment standpoint, but only if the α-emitting radionuclides can be specifically targeted to cancerous tissue. If the specificity is poor, and particularly if the antibodies have specificity for any non-cancerous cells, this may be a limitation to this treatment method. Additionally, many candidate TAT isotopes have decay products with half-lives on the order of hours, which are not likely to remain bound to the targeting molecule after recoiling from the first α-decay since molecular binding energies are several orders of magnitude lower than typical recoil velocities for α-decay residual nuclides [5]. Depending on the

bio-distribution of these products, this could also represent a limitation to certain α-emitting therapies. The low activity required is, however, a significant advantage from an isotope production perspective, as less total activity will need to be produced to treat a given number of patients.

The linear relationship between dose and cell survival for alpha emitters is generally beneficial for therapy. The single strand breaking mechanism of low-LET radiation means that several techniques can be used to increase the specificity of the cell killing towards cancer cells; techniques which will have no impact on alpha therapy. For example, timing the dose fractionations around the mitosis phase of the cancer cell-cycles can increase selectivity, as the low-LET radiation will not do as much damage to healthy tissue in the resting phase of the cell cycle [15]. Combining this with hyperbaric oxygen treatment can also increase selectivity, as the normally hypoxic cancer cells will then be more likely to have DNA damage locked in by the increased oxygen [16]. High-LET radiation is not cell-cycle specific, as double strand breaks are generally irreparable regardless of the stage in the cell cycle, and will therefore not see any improvement in selectivity from these strategies. This is likely a net benefit for cancer treatment, as many late stage cancers become resistant to such methods through gene amplification, or by inhibiting cellular apoptosis [12].

1.2 Promising Therapeutic α-emitters

There are a number of properties to consider when evaluating the suitability of an α-emitting radionuclide for therapeutic applications. Foremost is that the lifetime of the α-emitter must be short enough such that it has a high probability of decaying while it is in close proximity to the tumor. If the lifetime is too long, the targeting molecule may be degraded or cleared from the body before α-emission can take place. However the half-life must also be long enough, such that it can be reasonably produced, transported to a hospital, and injected into a patient without excessive loss of activity. This typically means that either the isotope itself, or a parent generator isotope, has a lifetime on the order of several hours to a few days. Because alpha decay is a tunneling phenomenon, the lifetime is exponentially related to the inverse of the Q-value, meaning the lifetimes of α-emitters have a wide variation. Of the approximately 950 known α-emitting radionuclides, 66 have a half-live between 1 hour and 30 days, only 40 of which have $Z \leq 94$ (Pu) [17].

In addition, many α-emitters are part of decay chains with multiple decay products, which are typically α-emitters as well. This can enhance the therapeutic potential if these decay products are short-lived, essentially compounding the dose rate to cancer cells for each targeting molecule. However if these decay products have long lifetimes, they can potentially cause issues for therapy. When the parent alpha decays, the nucleus will recoil with an energy

Isotope	Half-Life	Decays	Availability
^{225}Ac	9.920 (3) d	4 α, 2 β^-	Limited
^{211}At	7.214 (7) h	1 α, 1 EC	Low (cyclotron production)
^{213}Bi	45.61 (6) m	1 α, 2 β^-	Limited (^{225}Ac generator)
^{212}Bi	60.55 (6) m	1 α, 1 β^-	High (^{232}Th decay)
^{223}Ra	11.43 (5) d	4 α, 2 β^-	Commercially available
^{227}Th	18.697 (7) d	5 α, 2 β^-	High (^{235}U decay)
^{149}Tb	4.118 (25) h	17% α, 7% β^+, 76% EC	Very low

Table 1.1: List of potential therapeutic α-emitting isotopes, and their properties. [19–24]

of several keV, thousands of times greater than chemical binding energies, and may be ejected from the chelator molecule connecting it to the antibody. The long-lived decay product is then free to move about the body, and depending on the bio-kinetics of the product element, could lead to excess dose to healthy tissue and adverse side-effects. Some α-emitters have β/γ-emitters in their decay chains which, while not being as efficacious as alphas, are not a significant concern either due to the low activities typical of alpha therapy.

Two other important considerations are chemical compatibility and the potential to produce the isotope in quantities relevant to clinical use. Some TAT isotopes can be put into a relatively simple chemical form, such as $^{223}RaCl_2$, which still has some targeting specificity without having a targeting vector, as it has a propensity to accumulate in the bone marrow where there may be nearby metastases. However, most cancers will need to be treated by binding the TAT isotope to a targeting vector, such as an antibody, through chemical labeling methods or the use of a chelating linker. Therefore, using an isotope of an element with which targeting vectors can be successfully labeled is a requirement. It should be noted that although developing chelators for TAT molecules is an ongoing area of research [18], it is quite challenging as many TAT candidates have no stable isotopes of the same element which can be used for research purposes to establish chemistry. Furthermore, it is worth noting that many of the most promising TAT isotopes can lead to collateral damage to healthy cells from the decay of their daughter products, following separation from their targeting molecule after the first decay.

The production considerations are also complex. A pathway must be chosen that produces sufficient quantities of the isotope, with an acceptable purity. There may be multiple possible pathways for production, but depending on the target availability or facility requirements, some pathways may be infeasible. Some isotopes may benefit from or require the production of generator isotopes, rather than the TAT isotope itself. There are also safety and engineering concerns that must be accounted for. These considerations are investigated in detail in Chapter 5, for the case of ^{225}Ac production.

Table 1.1 lists a number of α-emitters which have shown therapeutic potential, either clinically or in mouse models. Of this list, ^{223}Ra is the only alpha-emitting isotope that has been approved for clinical use (as $^{223}RaCl_2$) [25]. Radium exhibits similar biochemistry to calcium, concentrating in bone marrow, which will preferentially target tumors that have metastasized there [25]. Because the cancer cells are not directly targeted, this form of treatment is usually not considered curative, however it has been shown to significantly extend overall survival times and improve patient quality of life [25]. ^{223}Ra is readily available, as it is part of the ^{235}U decay chain. In secular equilibrium, natural uranium will contain approximately 1.56 mCi of ^{223}Ra per kilogram. A ^{231}Pa or ^{227}Ac generator can be used to provide a steady supply of this isotope in a clinical setting. Furthermore, the longest-lived decay product of ^{223}Ra, which emits 4 α-particles in its decay chain, is ^{211}Pb ($t_{1/2}$ = 36.1 (2) m), which has been demonstrated to not significantly migrate away from the tumor site [26].

Also part of the ^{235}U decay chain, ^{227}Th has shown very promising preclinical results [27]. Thorium-227 is the parent isotope of ^{223}Ra and therefore has similarly favorable decay properties. However unlike radium, thorium can form highly stable chelation complexes. It is therefore able to be linked to various targeting vectors, such as the anti-CD20 antibody rituximab [28], and is therefore much more efficacious than $RaCl_2$ at targeting and killing disease. An additional advantage to using a thorium based alpha-emitter is that thorium exhibits similar chemical behavior to the Ce^{IV} oxidation state of the positron-emitting ^{134}Ce, which means that ^{134}Ce can be used to perform a rapid PET bio-assay of the complexed ^{227}Th during treatment [29].

^{212}Bi is also readily available, as it is part of the ^{232}Th decay chain, at 110 µCi/kg in natural thorium. ^{224}Ra, ^{228}Th or ^{228}Ra could be used as a generator for this isotope. Often the parent isotope, ^{212}Pb is complexed to a chelator for delivery to cancer cells, as it has a half-life of 10.622 (7) h. This is advantageous because it delivers more dose per unit activity, and has a more convenient lifetime to prepare and administer to patients. There are also bio-chemical benefits to using ^{212}Pb, as it has been shown that any ^{212}Pb labeled peptides which do not localize to a tumor are cleared from the body, minimizing dose to healthy tissue [30]. Also, the recoil from the β^- decay of ^{212}Pb is only about 0.8 eV, which is low enough such that the resultant ^{212}Bi generally remains bound in the chelation complex [31].

^{211}At offers a number of advantages over some of the other candidate TAT isotopes. Its 7.2 hour half-life is long enough to be convenient to administer to patients, but also short enough to have a high probability of damaging cancer cells. As a halogen, the chemical properties of astatine are also advantageous, as there are a number of well-developed administration routes [5]. The major disadvantage of ^{211}At is that the production capacity is very limited [5]. Due to the short half-life, it must either be produced at or very close to the hospital where it's administered. The only viable production pathway for ^{211}At is via ^{209}Bi(α,2n), which means that most hospital cyclotrons, typically tuned to run low-energy protons for production

of ^{18}F and other PET isotopes, would not be able to produce ^{211}At. However, the ideal bombardment energy for this pathway is approximately 20 MeV (to avoid co-producing the ^{210}At contaminant), so it is possible that some of these cyclotrons could be re-purposed for ^{211}At production in the future [5].

^{225}Ac as a TAT isotope has been quite successful in clinical trials against metastatic castration-resistant prostate cancer (mCRPC), with some cases showing complete remission [4]. In a study where 14 patients were treated with ^{225}Ac bound to the PSMA-617 peptide, 11 saw a significant (>50%) decrease in prostate-specific antigen (PSA) concentrations, 9 of whom saw significant anti-tumor activity [10]. ^{213}Bi, one of the decay products of ^{225}Ac, has also shown clinical potential in treating neuroendocrine tumors [9]. The main challenge associated with both isotopes (as ^{213}Bi is produced from a ^{225}Ac generator) is the very limited supply. However unlike ^{211}At, ^{225}Ac has a ≈10 day half-life, such that it does not need to be produced locally [24, 32]. One of the goals of this dissertation is to evaluate the various pathways which have been proposed to increase the global ^{225}Ac supply.

Because alpha therapeutics are so heterogeneously distributed, micro-dosimetry of the distribution of α-emitting radioisotopes is often considered necessary to ensure the safety of TAT treatments. Doing this non-invasively will require a scan of some sort. Some TAT isotopes emit low-energy γ-rays in their decay, which might be compatible with single-photon emission computed tomography (SPECT). However, the photon emission rates for TAT treatments is likely too low to be used in such scans. Typical TAT treatment activities are in the 100 µCi range, whereas SPECT scans usually require 10–30 mCi of activity [33].

Instead, a preferred approach is to use a β^+-emitting isotope which can be chelated to the same bio-marker, and perform a positron emission tomography (PET) scan. In this dissertation, we will present measurements for the ^{139}La(p,6n) production pathway for ^{134}Ce, which is a positron emitting analog of ^{225}Ac. The TAT isotope ^{149}Tb, however, may not require the production of a separate positron-emitting isotope to perform this scan. ^{149}Tb decays through a 17% α branch as well as a 7% positron branch, meaning it could simultaneously provide therapy and the means to perform a rapid bio-assay of the therapeutic isotope. This could significantly aid in performing better treatment. While ^{149}Tb has shown potential for high-quality PET diagnostics in mouse models [34], it is unclear if the level of activity required for PET would induce adverse cytotoxicity.

1.3 Potential ^{225}Ac Production Pathways

The global supply of ^{225}Ac, which is currently based on a fixed inventory of ^{229}Th, is about 2 Ci per year [32]. When treating mCRPC, there is neither a well-established activity requirement per treatment cycle, nor is there an established number of required cycles. However

Pathway	Comments
$^{233}U/^{229}Th$ generator	Fixed supply (350 mCi globally) too limited for commercial use.
$^{232}Th(p,x)^{225}Ac$	High yields, but small (0.1–0.2%) ^{227}Ac impurity. Significant fission.
$^{nat}U(p,x)^{225}Ac$	Lower yields than ^{232}Th pathway, same drawbacks.
$^{226}Ra(p,2n)^{225}Ac$	Highest yield per unit beam power, but ^{226}Ra target handling and cooling extremely challenging.
$^{232}Th(p,4n)^{229}Pa$	Creates long lived ^{229}Th generator, but very low ^{225}Ac yields compared to other pathways.
$^{226}Ra(\gamma,n)^{225}Ra$	Very high purity ^{225}Ac, target handling and cooling still an issue (but less so than (p,2n)).
$^{226}Ra(n,2n)^{225}Ra$	Higher cross-section than (γ,n). Target handling still challenging, but no cooling required.
$^{228}Ra(n,\gamma)^{229}Ra$	Good pathway for ^{229}Th generator production, but very little ^{228}Ra target material available.

Table 1.2: Potential production pathways for ^{225}Ac.

based on pre-clinical studies [10], this could be estimated at 200 µCi per treatment cycle, and 4 cycles. At the current supply levels, this means that globally only 2,500 patients could receive treatment each year. If ^{225}Ac becomes an established treatment method for mCRPC, the ^{225}Ac supply level will need to be increased significantly. In the United States alone, over 34,000 men die from prostate cancer each year [35]. Additionally, if ^{225}Ac or its decay product ^{212}Bi are found to aid in the treatment of other cancers, the supply will need to increase even further.

The current supply of ^{229}Th ($t_{1/2}$ = 7932 (28) y), which is the source of the ^{225}Ac used in human studies so far, originates from ^{233}U ($t_{1/2} = 1.592 \times 10^5$ (2) y) that was produced many decades ago [32], and has therefore had time to decay into ^{229}Th. While this means that the supply of ^{229}Th is slowly increasing, it is nowhere near enough to meet the expected demands for ^{225}Ac in the near future. While more ^{233}U could be produced through the $^{232}Th(n,\gamma)$ pathway in a reactor, this would still require a long in-growth period, and is undesirable as producing the fissile ^{233}U isotope has associated weapon proliferation risks.

Instead, most of the focus of actinium production has been on accelerator based pathways. One pathway that has been very well characterized is via the $^{232}Th(p,x)^{225}Ac$ reaction, sometimes referred to as spallation [36]. While the cross section for this reaction is modest, ranging from about 5–15 mb for energies above 50 MeV, the high proton energies typically used for this route enable the use of very thick targets. For a 200 MeV proton beam, the range in thorium metal is about 4.6 cm. As a result, the ^{225}Ac yields for this route are quite high.

Unfortunately, the yield of the contaminant isotope ^{227}Ac is also quite high; the atom ratio of produced ^{225}Ac/^{227}Ac is about 3:2. Because of the extremely long half-life of ^{227}Ac (21.772 (3) y), this corresponds to a radioisotopic purity of about 99.95% [37]. Through the entire decay sequence of ^{227}Ac, 5 α and 3 β^- particles are emitted, which could cause long-term adverse side-effects. Whether this is a significant issue mainly depends on the biostability of the chelating molecule and targeting vector [38]. While free actinium is retained by the body, chelated actinium, with and without the targeting molecule, are excreted, albeit at different rates [38]. Further studies still need to be performed about the long-term effects of this contaminant isotope. Additionally, the ^{225}Ac/^{227}Ac ratio will decrease with decay time, which may complicate clinical use as not all patients will receive ^{225}Ac of the same radiopurity.

Another currently pursued pathway is through the (p,2n) reaction on ^{226}Ra [39]. While this target is very challenging to work with in large quantities, as it is highly radioactive due to its half-life of 1600 years, it is the closest target in mass to ^{225}Ac that can be acquired in quantities of several grams. ^{226}Ra is part of the ^{238}U decay chain, and can be found in concentrations of 0.35 parts per million within natural uranium ores. There is also a large surplus of radium from used brachytherapy needles, that could be reprocessed for use as target material [40].

The ^{226}Ra(p,2n) reaction has a relatively large cross section, peaking above 600 mb at 15 MeV. This pathway is relatively free of contaminants, as both the nearby products ^{224}Ac ($t_{1/2}$ = 2.78 (17) h) and ^{226}Ac ($t_{1/2}$ = 29.37 (12) h) are short-lived relative to ^{225}Ac ($t_{1/2}$ = 9.920 (3) d). The major limitation of this approach is that most chemical forms of radium have poor thermal conductivity, which means the maximum proton beam current which could be safely dissipated in a radium target is likely quite low. Radium metal is highly reactive in air, and is not suitable [41]. Radium salts such as $RaCl_2$ or $Ra(NO_3)_2$ will have very poor thermal conductivity, although that could be somewhat offset by using a filler gas such as helium in the target. Even when dissolved in water, the thermal conductivity of these salts is still limiting, and this will significantly reduce the ^{225}Ac yield due to the decreased ^{226}Ra concentration. Radium could potentially be smelted into a hexaborane ceramic (RaB_6), as hexaboranes tend to have very high thermal conductivities and melting points [42]. However this has yet to be demonstrated, and would likely be afflicted by radon gas production from ^{226}Ra decay.

Another approach to actinium production would be to make the long-lived ^{229}Th generator through the ^{232}Th(p,4n) reaction. While the net production of ^{225}Ac through this pathway would be relatively low, it has the advantage of creating a high purity ^{225}Ac supply that is independent of accelerator production schedules. Because ^{225}Ac has a half-life of 9.9 days, and the treatment cycles will likely span multiple months, a lapse in ^{225}Ac supply from an accelerator shutdown would be very disruptive to treatments. Therefore a resilient supply

is quite attractive, especially if used in conjunction with other pathways.

^{226}Ra could also be used as a target material for high energy photons or neutrons, making the ^{225}Ra generator through (γ,n) or (n,2n) reactions, respectively. While the handling of radium targets is still a concern, the heat dissipated in the radium by (γ,n) is much less than the (p,2n) pathway, and for (n,2n) there is virtually no heating. These pathways have high radiopurity, as very little ^{227}Ac is generated, and even that can be chemically separated. The main limitation to these pathways is in finding a high-intensity, and high-energy source of photons or neutrons. In this dissertation, deuteron breakup is explored as a potential source for the ^{226}Ra(n,2n) pathway.

1.4 Organization of the Dissertation

The dissertation is organized in the following way.

Chapter 2 describes an experiment to measure the ^{139}La(p,6n)^{134}Ce cross section in the energy range of 35–60 MeV, using the stacked-target activation technique. ^{134}Ce is a proposed isotope for rapid *in vivo* bio-distribution assays of the chemically similar ^{225}Ac and ^{227}Th isotopes, which are used in targeted alpha therapy. ^{134}La, the 6.45 (16) minute decay product of ^{134}Ce, emits a positron in 64% of decays, which can be assayed via a PET scan. This work is useful for optimizing the production of ^{134}Ce in thick target irradiations. In addition, multiple other exit channels were measured, which were used for a basic comparison of pre-equilibrium modeling codes.

Chapter 3 describes measurements of the neutron spectra from thick target deuteron breakup, at 33 and 40 MeV incident deuteron energies, as well as proposing a parameterized hybrid model of deuteron breakup. One of the goals of this dissertation is to evaluate the use of deuteron breakup as a neutron source for isotope production, with an emphasis on ^{225}Ac production, and having an accurate model of the neutron source spectrum is essential for this purpose. As the available literature data on deuteron breakup are somewhat limited and inconsistent, measuring the breakup spectrum served to enhance confidence in this model over the application range considered.

Chapter 4 describes measurements of the ^{226}Ra(n,2n) cross section using a thick target deuteron breakup neutron source. The measurements were performed at 33 and 40 MeV incident deuteron energies on a beryllium target. The production rate of ^{225}Ra was quantified using α-spectroscopy of the decay products ^{221}Fr and ^{217}At, which was then used to determine a spectrum averaged cross section, calculated using the deuteron breakup model developed in chapter 3. These measurements resolved a discrepancy between the ENDF and TENDL evaluations for this cross section, and also served as a proof of principal that ^{225}Ac can be produced via this pathway in quantities relevant to therapeutic use.

In chapter 5, several pathways for ^{225}Ac production were evaluated in a comparison study. The purpose of this study was not to make conclusions about a "best" pathway, but rather to provide realistic production rate estimates based on a reference beam power, and to improve the understanding of the systematic trends associated with each pathway. The radiopurity of the ^{225}Ac product and thermal limitations were also evaluated.

Finally, in appendix A, additional details are provided on the mechanical design of the target used for the experiment in chapter 4.

Chapter 2

Measurement of ^{139}La(p,x) Cross Sections from 35–60 MeV by Stacked-Target Activation

In order to treat rapidly developing diseases like metastatic prostate cancer, targeted alpha therapeutics require non-invasive rapid assay techniques for imaging the growth or recession of the disease. One of the highest resolution imaging techniques for doing so is positron emission tomography (PET). Due to the back-to-back annihilation photons produced from the interaction of positrons with electrons in matter, coincidence imaging techniques can identify a ray along which the photons must have traveled to reach the detector. Summing many such rays can be used to provide a high-resolution image of the PET source distribution. Combining this with photon time-of-flight techniques can enhance this resolution even further. By labeling a bio-marker such as an antibody with a PET radionuclide, biological processes such as cancer progression can be observed with great detail.

Unfortunately, most α-emitting radionuclides don't contain a positron decay branch in any of their decay chains. Specifically, ^{225}Ac, the therapeutic α-emitter studied in this work, does not emit any positrons and only emits γ-rays further down the decay chain. While one could consider performing single-photon emission tomography (SPECT) with these γ-rays, the issue with delayed γ emission is that the recoil from the initial α decay is likely to have moved the daughter isotope away from the target site; negatively affecting the resolution and utility of the image. Additionally, the ^{225}Ac activities relevant to clinical use are likely too low for SPECT imaging.

Instead, we can make use of a positron-emitting isotope that acts as a chemical analog of the radiopharmaceutical for which we wish to know the bio-distribution. For the case of

^{225}Ac, the element cerium has been shown to have similar chemical behavior in its reduced Ce^{III} state [29]. The ^{134}Ce/^{134}La system has been chosen as an *in vivo* PET isotope generator, to act as an analog to ^{225}Ac. ^{134}Ce ($t_{1/2} = 3.16(4)$ d) decays by electron capture to the 6.45 (16) minute ^{134}La, which subsequently emits a 1.2 MeV positron in approximately 62% of decays [43]. The low recoil, short half-life of the daughter, and limited γ-emissions of this system make it an ideal candidate PET analog to ^{225}Ac.

This chapter details a measurement of the production cross sections for ^{134}Ce through the ^{139}La(p,6n) reaction, as well as any other radionuclides co-produced in the 35–60 MeV proton energy range studied. This measurement was performed using the stacked-target activation technique, with a variance minimization procedure performed to optimize the energy assignments and beam currents associated with each foil. The results were compared to default calculations performed with several state-of-the-art nuclear reaction codes, as a brief exploration of the role that pre-equilibrium has in nuclear reaction modeling. These results will be useful in determining the optimum irradiation parameters for bulk isotope production of ^{134}Ce from thick targets.

Relevant Publications:

J.T. Morrell, A.S. Voyles, M.S. Basunia, J.C. Batchelder, E.F. Matthews, L.A. Bernstein, *Measurement of ^{139}La(p,x) cross sections from 35–60 MeV by stacked-target activation.* Eur. Phys. J. A. **56**, 13 (2020) doi:10.1140/epja/s10050-019-00010-0

 Some of the figures and content in this chapter have been altered to better fit the page formatting, but all changes made to the published journal article are purely stylistic in nature.

2.1 Abstract

A stacked-target of natural lanthanum foils (99.9119% ^{139}La) was irradiated using a 60 MeV proton beam at the LBNL 88-Inch Cyclotron. ^{139}La(p,x) cross sections are reported between 35–60 MeV for nine product radionuclides. The primary motivation for this measurement was the need to quantify the production of ^{134}Ce. As a positron-emitting analogue of the promising medical radionuclide ^{225}Ac, ^{134}Ce is desirable for *in vivo* applications of bio-distribution assays for this emerging radio-pharmaceutical. The results of this measurement were compared to the nuclear model codes TALYS, EMPIRE and ALICE (using default parameters), which showed significant deviation from the measured values.

2.2 Introduction

Proton-induced nuclear reactions in the several tens of MeV incident energy range are commonly used for the production of radionuclides with minimal contaminants, making them a compelling production pathway for diagnostic and therapeutic medical radionuclides [44]. Well-characterized nuclear data for many of these reactions are scarce, yet are critical for researchers wishing to optimize production schemes for these radionuclides [45].

In this work we measured cross sections for the ^{139}La(p,x) reactions, with a particular interest in the (p,6n) reaction on ^{139}La (99.9119% n.a.) for the production of ^{134}Ce, a medically relevant radionuclide. In addition, the data from this experiment provide insight into reaction mechanisms and nuclear properties, including pre-equilibrium particle emission and nuclear level densities, making it useful for benchmarking nuclear reaction modeling codes [45–47].

Motivation

Actinium-225 is a promising candidate for new alpha-emitting therapeutic radio-pharmaceuticals [48]. Actinium-225 has a relatively short half-life of 9.9203 (3) days, and decays to ^{209}Bi (stable) through the emission of 4 α and 2 β^- particles [22,24,49–51]. The short range of these α particles is prized for sparing nearby healthy tissue while delivering a lethal dose to the site of disease [52]. There are no long-lived products in the decay chain, with the longest activity being the 3.2 h ^{209}Pb [51]. These properties make ^{225}Ac a very compelling candidate for targeted radionuclide therapy [48]. In developing biological targeting vectors for the delivery of ^{225}Ac, their selectivity must be quantified using biodistribution assays [53]. The standard for these assays is positron emission tomography (PET), which isn't possible with ^{225}Ac due to the lack of positron emission in its decay chain.

Instead, ^{134}Ce has been proposed as a positron emitting analogue of ^{225}Ac, for potential use in rapid-throughput *in vivo* biodistribution assays. Cerium-134 decays with a half-life of 3.16 (4) days, which is the closest of the β^+-emitting Cerium radionuclides to the 10 day half-life of ^{225}Ac [24,43]. PET imaging of the ^{134}Ce uptake is performed through the daughter radionuclide ^{134}La, which β^+ decays with a short half-life (6.4 minutes) [43].

One proposed mechanism for the production of ^{134}Ce is through the ^{139}La(p,6n) reaction, using targets of natural lanthanum, which have a 99.9119% natural isotopic abundance of ^{139}La. This reaction is poorly characterized in the 35–60 MeV energy region, and the predictions of the extensively-used TALYS [54] and EMPIRE [55] nuclear reaction modeling codes differ by an order of magnitude. The discrepancies in predictions from these modern codes have profound implications for the design of targets for not only the production of ^{134}Ce, but also for the production of other radionuclides utilizing energetic proton-induced

reactions. The objective of this paper is to report on a new set of cross section measurements performed using the stacked-target activation technique. This information will be used to not only quantify the production of ^{134}Ce, but to gauge the accuracy of several different nuclear reaction models used to predict intermediate light-ion reactions in the energy range below 60 MeV.

2.3 Methodology

In this work we used the stacked-target activation technique, in which one can measure a reaction cross section by quantifying the activity induced within a thin foil of known areal density, using a beam of known intensity [56, 57]. In a single irradiation, many foils can be placed in a "stack" (along with monitor foils), yielding cross section measurements at multiple energies by lowering the energy of the primary beam as it traverses the stack. In this experiment "degrader" foils were also included in the stack, to further reduce the beam energy between target foils, such that the measured cross sections fell within the 35–60 MeV range.

Following irradiation, the end-of-bombardment (EoB) activities of the various proton-induced reaction products were determined by counting the γ-rays emitted from each foil, using a well-calibrated high-purity germanium (HPGe) detector. The reaction cross sections (leading to a particular product) were then calculated from the EoB activities. Many of the produced radionuclides included decay feeding from a parent also produced in the ^{139}La(p,x) reaction. Where this contribution was separable, we have reported independent cross sections, however in cases where the parent decay was unable to be measured we have reported cumulative cross sections.

The proton beam current incident upon the stack was estimated using a current integrator. However, the beam current used in the calculation of the cross section was determined more precisely using natural copper and aluminum monitor foils for each lanthanum foil in the stack. These foils have multiple reaction channels with well-characterized cross sections [58].

The flux-averaged proton energy associated with each cross section was determined using a Monte Carlo model based on the Anderson & Ziegler stopping power tables [59]. This model was optimized to give the best energy assignments using the monitor foil activation measurements, consistent with the technique proposed by Graves *et al.* in 2016 [56]. The areal density of each foil in the stack was determined by repeated measurements of the mass and area of each foil.

Description of Experiment

The lanthanum foils used in this experiment were of 99% purity and were purchased from Goodfellow Corporation (Coraopolis, PA 15108, USA). The foils were cold rolled to 25 μm thickness, cut to 1" by 1" squares, and sealed in glass ampules with an inert cover gas (to prevent oxidation). Just prior to the experiment these ampules were opened, and the foils were removed and cleaned with isopropyl alcohol. The dimensions and masses of these foils were measured, and they were sealed in 3M 5413-Series Kapton polyimide film tape – each piece of tape consists of 43.2 μm of a silicone adhesive (nominal 4.79 mg/cm^2) on 25.4 μm of a polyimide backing (nominal 3.61 mg/cm^2). The copper and aluminum monitor foils were cut from 25 μm-thick sheets into 1" by 1" squares, and were also measured and sealed in Kapton tape. These foil packets were then secured over the hollow aperture of 2.25" by 2.25" aluminum sample holders (see fig. 2.1), which protected the foils during handling and centered them in the beam pipe. Ten sets, each consisting of a single aluminum, copper and lanthanum foil packet, were prepared in this manner for cross section measurements at ten different energies.

Figure 2.1: Photo of an individual foil packet secured to the aluminum sample holder (left) and the entire foil stack (right). The front of the stack (facing the beam) is oriented towards the right in this photo.

Multiple plates of 6061-aluminum, also 2.25" by 2.25", were placed in between each set of foil packets to degrade the beam energy by a few MeV between each foil packet, allowing

cross section measurements over a range of proton energies from 35–60 MeV. Additionally, stainless steel plates (approximately 100 mg/cm^2) were placed at the front and back of the stack. Post-irradiation dose mapping of the activated stainless plates using radiochromic film (Gafchromic EBT3) confirmed that the proton beam was centered on the samples, and that the entirety of the ≈1 cm-diameter primary proton beam was contained well within the 1" by 1" borders of the foil packets. This method is consistent with previously established techniques [56, 57].

A single ORTEC GMX Series (model GMX-50220-S) High-Purity Germanium (HPGe) detector was used in this experiment. The detector is a nitrogen-cooled coaxial n-type HPGe with a 0.5 mm beryllium window, and a 64.9 mm diameter, 57.8 mm long crystal. The energy and photopeak efficiency of the HPGe detector used in this measurement were calibrated using four standard calibration sources of known activity (rel. error <1%): ^{137}Cs, ^{152}Eu, ^{54}Mn and ^{133}Ba. The photopeak efficiencies were also corrected for detector dead-time, as well as self-attenuation within the foils — using photon attenuation cross sections retrieved from the XCOM database [60].

Facility Overview

This experiment took place using a proton beam at the 88-Inch Cyclotron located at Lawrence Berkeley National Laboratory (LBNL) in Berkeley, California [61]. The 88-Inch Cyclotron is a variable-beam, variable-energy K=140 isochronous cyclotron, with a maximum recorded proton energy of 60 MeV and a maximum proton beam current of approximately 20 μA.

The 88-Inch Cyclotron facility has several isolated beamlines for a multitude of applications (see fig. 2.2). This experiment took place in Cave 0, which has a ∼3 m beamline that is shielded from any neutron radiation produced in the cyclotron vault. The target holder for the foil stack was mounted at the end of this beamline, downstream from two bending magnets and several focusing quadrupoles in the main cyclotron vault.

This experiment marked the first time in recent history that the 88-Inch Cyclotron had attempted extracting a 60 MeV proton beam. Due to RF-power and beam optics limitations, the result was extremely low transmission with only approximately 8 nA of beam current (≤0.1% transmission efficiency). A subsequent tune to Cave 0 exhibited significantly higher transmission, suggesting that better performance can be expected in future energetic proton runs. It was later determined by the monitor foil activation that the mean beam energy was approximately 57 MeV, and not 60 MeV as originally desired, further indicating that the initial tune was far from optimized for 60 MeV protons.

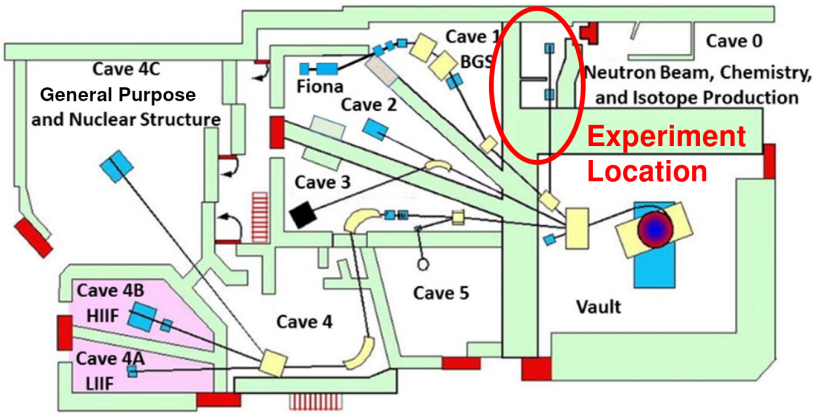

Figure 2.2: Graphical representation of the 88-Inch Cyclotron floor plan. The irradiation described here took place in Cave 0, which is circled above in red.

Irradiation and Counting

The foils were irradiated with 8 nA of proton beam current for 1 hour, 37 minutes and 24 seconds. The total collected charge of the beam was measured using a current integrator connected to the electrically-isolated target holder, which was used to determine that the beam current was stable over the duration of the experiment. This measurement of the beam current incident upon the target holder was also used to validate the beam current values determined using the monitor foil activation.

After irradiation, the foils were removed from the beamline and transferred to the HPGe counting lab approximately 15 minutes after EoB. Upon removal it was discovered that the third lanthanum foil showed excessive oxidation and had ruptured its Kapton encapsulation (prior to counting), indicating potential material loss. Therefore, in the interest of surety, no cross sections will be reported for this foil.

The foils were counted for four weeks following EoB. Each foil was counted multiple times, in order to reduce uncertainty and aid in isotope identification. This lengthy counting duration was necessary because the 604.6 and 606.8 keV γ-rays from the ^{135}Ce isotope significantly contaminated the 604.7 keV line emanating from the ^{134}Ce daughter isotope ^{134}La [43, 62]. Because the ^{134}Ce isotope has a longer half-life (3.16 days vs 17.7 hours), the 604.7 keV γ-ray was able to be resolved after the ^{135}Ce isotope had decayed to negligible levels [43, 62].

2.4 Data Analysis

The general procedure for calculating cross sections proceeded as follows. First, every γ line emitted from each isotope of interest was fit in each spectrum collected. The number of counts in each peak was used to determine the activity of the isotope at the time the spectrum was taken. These activities as a function of "cooling" time (time since EoB) were used to calculate the EoB activity, A_0, for that isotope. Each A_0 was then used to determine a cross section (for the lanthanum foil data) or a beam current (for the copper/aluminum foil data). The energy assignments for each foil were determined using the variance minimization approach proposed by Graves [56], as discussed in sect. 2.4. The NPAT code, developed at UC Berkeley [63], was used for spectrum analysis, fitting decay curves, and calculating the proton energy spectrum in each foil.

The uncertainties in the reported cross sections had five main contributions: uncertainties in evaluated half-lives and gamma intensities (≈1%), EoB activity determination (≈1%), detector efficiency calibration (≈3%), foil areal density (≈1%) and proton current determination (≈5%). Each contribution to the uncertainty was assumed to be independent and was added in quadrature.

Peak Fitting

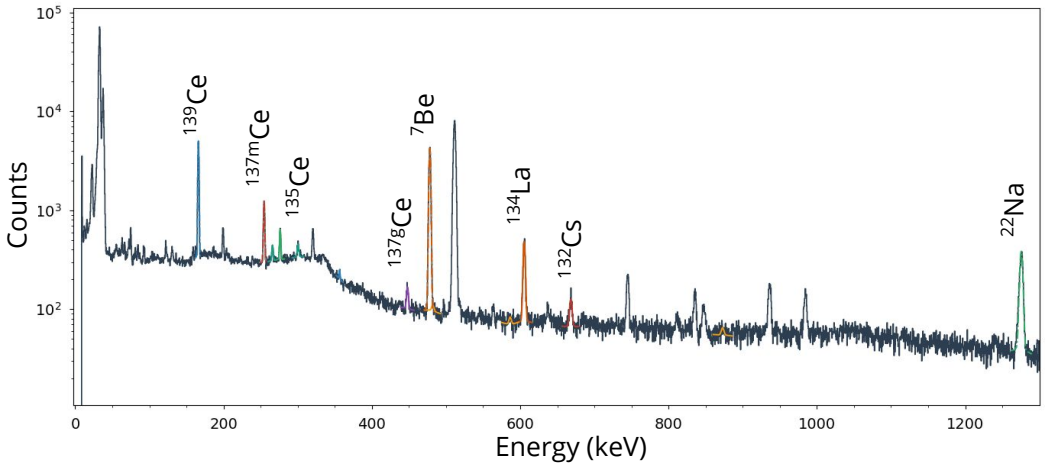

Figure 2.3: A γ-ray spectrum collected from the lanthanum foil activated with approximately 56 MeV protons.

The detector energy and efficiency calibration, as well as the induced activity in each sample, were determined by peak fitting to the individual spectra. Energy centroids and relative intensities were constrained with some uncertainty by the decay data from ENSDF

[17], also listed in Appendix 2.6. Each peak was fit with a skewed Gaussian function on top of a linear background [64]. As implemented in the NPAT code [63], the complete functional form of the peak fit, $F(i)$, as a function of channel number i is as follows.

$$F_{peak}(i) = m \cdot i + b + A \cdot [\exp(-\frac{(i-\mu)^2}{2\sigma^2}) + R \cdot \exp(\frac{i-\mu}{\alpha\sigma}) \operatorname{erfc}(\frac{i-\mu}{\sqrt{2}\sigma} + \frac{1}{\sqrt{2}\alpha})] \quad (2.1)$$

where $m \cdot i + b$ is the background component, $A \cdot \exp(-\frac{(i-\mu)^2}{2\sigma^2})$ is the (dominant) Gaussian component, and $A \cdot R \cdot \exp(\frac{i-\mu}{\alpha\sigma}) \operatorname{erfc}(\frac{i-\mu}{\sqrt{2}\sigma} + \frac{1}{\sqrt{2}\alpha})$ is the "tailing" component. Typical values of R and α are ≈0.2 and ≈0.9, respectively.

The number of counts in a photopeak fit using this functional form is given by

$$N_c = A\Big(\sqrt{2\pi}\sigma + 2R\alpha\sigma \exp(-\frac{1}{2\alpha^2})\Big) \quad (2.2)$$

An example of a measured γ-ray spectrum is shown in fig. 2.3, with photopeak fits superimposed on the spectrum.

Determining Foil Activities

To obtain the EoB activities for each proton-induced reaction product, in each foil, we determine the apparent activity from each photopeak that was observed and perform a fit to the decay curve generated from the appropriate Bateman equations [65].

For a single photopeak having N_c counts observed with efficiency ϵ from a radionuclide with decay constant λ and intensity I_γ, the apparent activity in a photopeak at some cooling time t_c after the end-of-bombardment is given by by

$$A(t_c) = \frac{\lambda N_c}{(1 - e^{-\lambda t_m}) I_\gamma \epsilon} \quad (2.3)$$

where t_m is the measurement time. If the population of this nucleus has no contribution from the decay of a parent, the activity A_0 can be determined using a fit to the equation

$$A(t_c) = A_0 e^{-\lambda t_c} \quad (2.4)$$

Eq. 2.4 is only valid for single-step decay pathways, and several activation products in this experiment exhibit multi-step decays. For example, ^{134}Ce decays to ^{134}La which then decays to the stable ^{134}Ba [43]. For these two-step decay chains, the decay curve will take the form

$$A_D(t_c) = A_{P_0} R_b \frac{\lambda_D}{\lambda_D - \lambda_P} (e^{-\lambda_P t_c} - e^{-\lambda_D t_c}) + A_{D_0} e^{-\lambda_D t_c} \quad (2.5)$$

where R_b is the branching-ratio, and the subscripts P and D indicate the parent and daughter isotopes respectively. An example of a fit to this exponential decay curve is shown in fig. 2.4. This calculation of the EoB activities required a measurement of the initial parent activity A_{P_0}, again using a fit to Eq. 2.4, which somewhat increased the uncertainty in the calculation of the initial daughter activities. However, most EoB activities were still quantified to approximately 1–3% relative uncertainty.

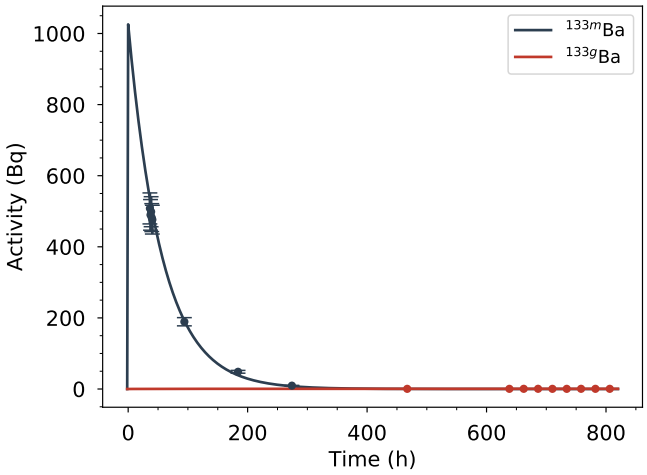

Figure 2.4: Example of a decay curve and associated exponential fit used to calculate the initial activity of the ^{133m}Ba and ^{133g}Ba isotopes in the 1^{st} lanthanum foil. The uncertainty in the activity was dominated by counting statistics and the evaluated half-life for most of the observed reaction products.

Current Monitors and Energy Assignments

Using the end-of-bombardment activities A_0 determined by the activation spectra and the measured areal densities ρr of each foil, we can calculate the proton beam current (in units of protons per second) I_p incident upon each monitor foil according to

$$I_p = \frac{A_0}{\bar{\sigma}(\rho r)(1 - e^{-\lambda t_i})} \tag{2.6}$$

where the factor $(1 - e^{-\lambda t_i})$ accounts for decay during a constant production interval t_i, and the flux-weighted cross section $\bar{\sigma}$ is given by

$$\bar{\sigma} = \frac{\int_0^\infty \sigma(E)\psi(E)dE}{\int_0^\infty \psi(E)dE} \tag{2.7}$$

where $\sigma(E)$ comes from the IAEA-recommended cross sections [66] and $\psi(E)$ is the energy spectrum of the proton flux.

This treatment accounts for the fact that the beam has a finite energy width that increases toward the back of the stack due to energy straggling of the beam. The proton flux spectrum $\psi(E)$ was determined using an Anderson & Ziegler-based Monte Carlo code, as implemented in NPAT [59, 63]. A plot showing the flux spectra for each foil in the stack, as predicted by the Anderson & Ziegler-based model, is shown in fig. 2.5.

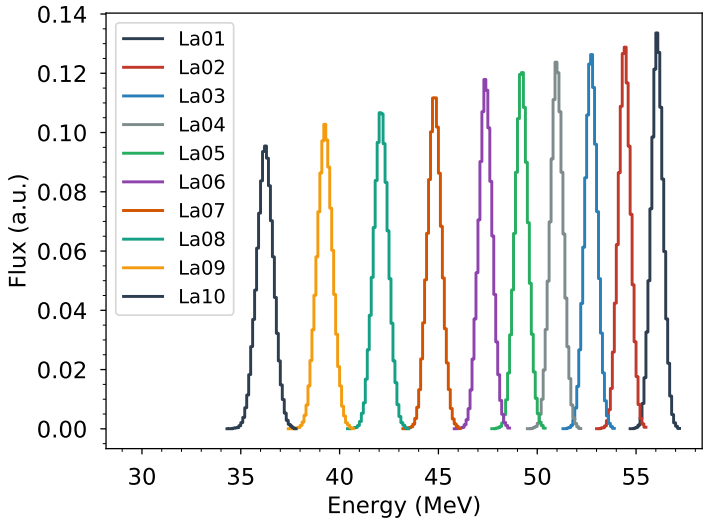

Figure 2.5: Plot of the calculated proton energy spectra for each lanthanum foil in the target stack.

Measured currents for the three copper monitor reactions and the two aluminum reactions are plotted in fig. 2.6, as well as a linear fit to these values, which was used to interpolate the beam current witnessed by the lanthanum foils. One would expect the proton beam current to decrease as it traverses the stack as the beam reacts, scatters and diffuses out of the path of downstream foils. However, only a very small decrease in beam current was observed; therefore, a linear fit proved sufficient for the interpolation.

As can be seen in fig. 2.6, the uncertainty in both aluminum monitor reactions was exceptionally large, particularly in the ^{27}Al(p,x)^{22}Na reaction. This was due to corrections for contaminating reactions in the silicone-based adhesive of the Kapton tape that sealed the foils (^{28}Si(p,x)^{22}Na and ^{28}Si(p,x)^{24}Na), as well as reactions on the aluminum frames. These corrections were performed by measuring the activities of the ^{22}Na and ^{24}Na isotopes in the Kapton sealing the neighboring lanthanum and copper foils, and subtracting this contribution from the aluminum foil data.

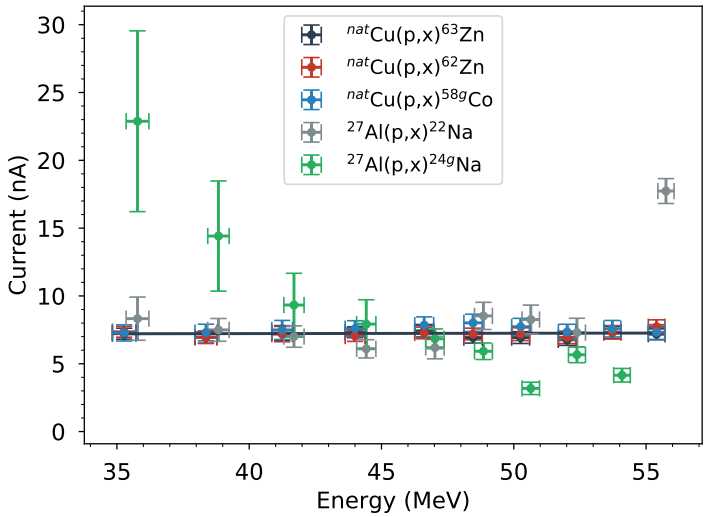

Figure 2.6: Plot of the proton beam current measured by each of the monitor foil reaction channels, along with a linear fit that was used to calculate the current for the lanthanum foils. The aluminum monitor channels are plotted only to illustrate the magnitude of the uncertainty due to contaminating reactions in the Kapton, and were not included in the final analysis.

Secondary neutron production could have also contributed to ^{22,24}Na activation. However, the secondary neutron flux predicted by an MCNP model of the experiment was 3–4 orders of magnitude lower than the proton flux, suggesting that it has a minor effect on the measured monitor reaction activities [67].

To prevent systematic errors, it was decided to remove the aluminum monitor channels from the analysis, however the (post-correction) results from these channels are still plotted in fig. 2.6, to illustrate the magnitude of the error induced by contaminating reactions in the aluminum frames and silicone adhesive.

Optimization of Energy Assignments

The flux-averaged proton energies and 1σ-widths of the proton energy distributions for each foil were first estimated using the Anderson & Ziegler formalism for proton transport (stack design listed in Appendix B). The apparent proton current in each monitor foil was measured using the IAEA-recommended cross sections for the ^{nat}Al(p,x)^{22}Na, ^{nat}Al(p,x)^{24}Na, ^{nat}Cu(p,x)^{62}Zn, ^{nat}Cu(p,x)^{63}Zn, and ^{nat}Cu(p,x)^{58}Co monitor reactions [66]. Disagreement in the apparent beam current between monitor channels was observed, particularly for the foils on the low-energy side of the stack, which was where the energy dependence of the monitor cross sections varied most strongly. This was indicative of incorrect characterization of the proton energy spectra incident on each monitor foil.

To correct this discrepancy, the effective density of the 6061-aluminum degrader foils was treated as a free parameter in the energy loss calculation, and was optimized with respect to the reduced χ^2 of the (linear) fit to the monitor reaction data. The minimum value of χ^2_ν yields the energy assignments which give the best agreement between the proton current derived from the various monitor reaction channels. This "variance minimization" technique was performed in a manner consistent with Graves (2016) and Voyles (2018) [56,57]. Afterwards, because the discrepancy was still quite large for foils in the high-energy portion of the stack ($\approx$30%), the incident beam energy was also treated as a free parameter and this same minimization was performed on density and incident energy simultaneously. This resulted in a more reasonable density change of -2%, for an average incident beam energy of 57 MeV.

It should be noted that this variance minimization approach does not necessarily imply that the degrader density was physically less or greater than was measured, but instead serves as a correction for stopping power characterization and enhanced energy loss due to unaccounted systematics in the original stack design. In essence, this method assigns energy spectra to each foil which best match the shape of the apparent monitor reaction cross sections to the shape of the IAEA-recommended charged-particle reference standards.

Fig. 2.7 shows the results of this minimization for an incident proton energy of 57 MeV. The reduced χ^2 of the linear fit to the monitor foil currents (shown in fig. 2.6) was used to determine the optimum energy assignments, based on the Anderson & Ziegler proton transport model, by varying the effective areal density of the 6061-aluminum degraders.

This minimization shows that the optimum energy assignments result from a -2% change in the effective areal density of the stack. Additionally, it implies that the average incident proton beam energy was 57 MeV, rather than the expected 60 MeV, an unexpected deviation from the initial estimates. This discrepancy could be attributable to a number of experimental factors. This was the highest-energy proton beam in recent history at the LBNL 88-Inch Cyclotron, and the cyclotron tuning solutions were observed to be significantly different than

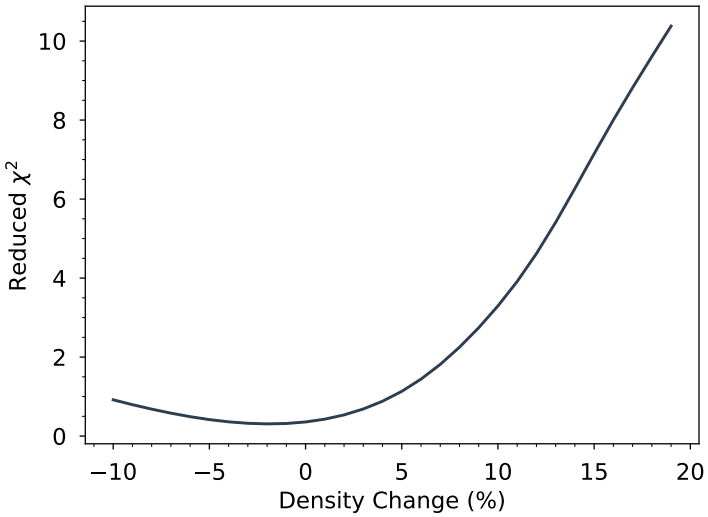

Figure 2.7: Plot of the reduced χ^2 figure-of-merit for the current monitor data, as the effective density of the degraders was varied.

for beams run more frequently at the facility. This is supported by the fact the transmission out of the cyclotron was very low, about 0.1%, and that a subsequent retune of the machine (after the irradiation) yielded a much better transmission.

This monitor foil variance minimization technique was also performed with the Monte Carlo code MCNP [67]. This corresponded to a 15% enhancement in the degrader areal density, which is significantly higher than comparable values in the literature [56, 57]. These results suggest a systematic issue in the low-energy charged-particle stopping power tables used by MCNP, and that a detailed comparison between the Anderson & Ziegler and MCNP stopping powers should be further explored in this intermediate energy range.

2.5 Results and Discussion

Using the end-of-bombardment activities, beam currents, and energy assignments determined in the previous section, the flux-averaged cross sections were calculated with the following equation

$$\sigma = \frac{A_0}{I_p(\rho r)(1 - e^{-\lambda t_i})} \tag{2.8}$$

The results of these cross section measurements are summarized in table 2.1, and are described in detail below.

These results were compared to the TENDL-2017 evaluation and predictions from the TALYS-1.9, EMPIRE-3.2 and ALICE-20 nuclear reaction modeling codes, all using default parameters [54, 55, 68]. The pre-equilibrium model used in the EMPIRE and ALICE calculations was the Hybrid Monte-Carlo Simulation module (HMS), while the TALYS code uses an exciton pre-equilibrium model [54, 55, 68]. Many of the excitation functions had a characteristic "compound peak" corresponding to energies between the threshold and the opening of the next significantly populated exit channel.

These measurements were also compared to the work of Tárkányi *et al.*, who performed a similar stacked target measurement on ^{nat}La in 2017 [69]. There were some discrepancies between the results of this work and the Tárkányi measurements, however there wasn't a clear systematic bias between one set of measurements and the other. Because the largest discrepancies were observed in channels featuring multi-step decay, it is most likely that differences in counting schedules and multi-step decay fits were the major sources of systematic discrepancies between the two experiments.

^{139}La(p,6n)^{134}Ce Cross Section

^{134}Ce undergoes electron capture decay to the ^{134}La ground state with a 98.9% branching ratio, with a 0.209%, 130.4 keV γ-ray being the strongest line [43]. The low-intensity and energy of this transition led us to choose the 604.721 keV (I_γ=5.04%) line in the decay of the daughter isotope ^{134}La to measure the ^{139}La(p,6n)^{134}Ce cross section. Because ^{134}La has a 6.45 minute half-life, all 604.7 keV γ's measured after several hours of decay time were attributable only to the decay of the initial ^{134}Ce population, regardless of the initial population of ^{134}La.

An additional complication was that ^{135}Ce produces multiple decay γ's very close in energy to the 604.7 keV line. Because of the 17.7 (3) hour half-life of ^{135}Ce, roughly two weeks of post-irradiation decay time were required to measure the ^{134}Ce activity without contaminating γ lines from ^{135}Ce.

The measured cross sections for the production of ^{134}Ce are plotted in fig. 2.8. The hybrid Monte Carlo simulation (HMS) pre-equilibrium model used by EMPIRE seems to slightly over-estimate the centroid energy of the "compound peak" seen in the measured data, whereas the exciton model used by TALYS underestimates the peak in the (p,6n) channel by 5–10 MeV. ALICE also uses a HMS model, and while it accurately estimates the centroid of the cross section it significantly overestimates the magnitude. This was not necessarily the case for all the measured reaction channels, but a similar trend could be seen for the (p,5n) channel as well (fig. 2.9).

	^{139}La(p,x) Production cross section (mb)					
E_p (MeV)						
	56.07 (31)	54.42 (32)	50.99 (33)	49.21 (34)	47.38 (35)	44.80 (37)
	42.09 (39)	39.25 (41)	36.23 (44)			
^{134}Ce$_i$						
	50.7 (88)	20.3 (97)	3.9 (25)	2.55 (38)	-	-
	-	-	-			
^{135}Ce$_c$						
	458 (23)	474 (23)	377 (17)	332 (15)	254 (14)	123.4 (30)
	29.00 (82)	2.90 (16)	0.493 (37)			
^{137m}Ce$_i$						
	79.9 (47)	89.2 (51)	95.9 (52)	112.4 (59)	124.5 (75)	148.3 (46)
	179.9 (52)	306 (14)	426 (14)			
^{137g}Ce$_i$						
	23.5 (51)	26.2 (57)	27.4 (68)	32.3 (80)	37.4 (74)	40.8 (78)
	48.7 (96)	77 (18)	114 (30)			
^{139}Ce$_c$						
	18.9 (12)	19.1 (19)	20.8 (17)	17.6 (16)	19.8 (17)	23.9 (11)
	23.29 (78)	31.7 (16)	29.9 (11)			
^{132}Cs$_i$						
	0.170 (14)	0.1114 (54)	0.0405 (57)	-	-	-
	-	-	-			
^{133m}Ba$_i$						
	12.54 (72)	13.89 (79)	13.74 (74)	13.76 (69)	12.57 (77)	9.21 (30)
	5.17 (15)	2.67 (24)	0.682 (81)			
^{133g}Ba$_i$						
	2.82 (67)	3.1 (16)	2.6 (13)	5.0 (11)	3.4 (12)	3.87 (93)
	1.77 (58)	-	-			
^{135}La$_i$						
	191 (61)	176 (77)	77 (38)	77 (39)	80 (57)	-
	-	-	-			

	^{nat}Cu(p,x) Production cross section (mb)					
E_p (MeV)						
	55.40 (32)	53.73 (33)	52.02 (34)	50.26 (34)	48.46 (35)	46.62 (36)
	44.00 (38)	41.25 (40)	38.37 (42)	35.28 (45)		
^{61}Cu$_c$						
	83.2 (27)	89.7 (33)	93.0 (18)	101.1 (31)	110.3 (37)	120.3 (35)
	142.4 (20)	164.7 (93)	183.3 (72)	182.7 (44)		

Table 2.1: Summary of cross sections measured in this work. Subsripts c and i indicate cumulative and independant cross sections, respectively.

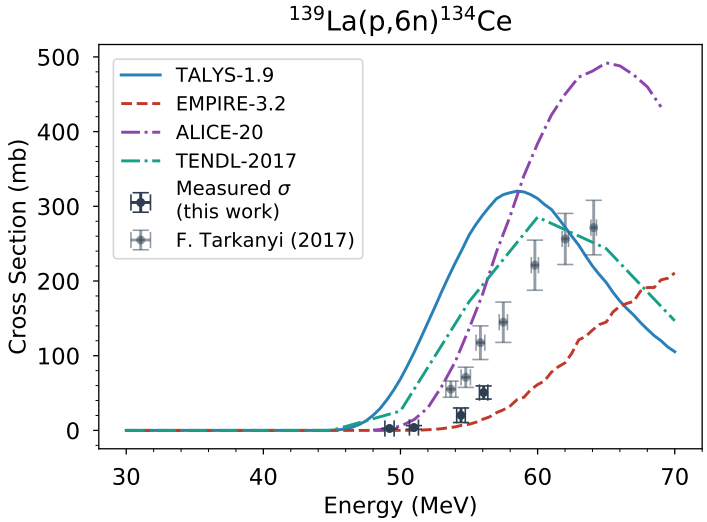

Figure 2.8: Measured cross sections for the ^{139}La(p,6n)^{134}Ce reaction.

This was likely attributable to differences in the pre-equilibrium models between the codes. Because particles emitted in pre-equilibrium carry a significant amount of energy out of the nucleus before compound nucleus formation, small differences in these models can greatly affect which compound nucleus is formed at a given incident proton energy, shifting the centroid energy of the "compound peak". And while the TENDL-2017 evaluation (based on TALYS-1.9 [54]) better matches data than the modeling codes, it still underestimates the energy of the peak in the cross section by about 5 MeV.

^{139}La(p,5n)^{135}Ce Cross Section

The ^{139}La(p,5n)^{135}Ce reaction was perhaps the most accurately quantified, due to a high number of intense γ emissions (*e.g.* 41.8% for the 265.56 keV line) and a 17.7 hour half-life. Because the ^{135m}Ce isomer ($t_{1/2}$=20 s) had completely decayed by the time the foils had been transferred to the counting lab, the reported cross sections for this reaction are cumulative.

The measured cross sections are plotted in fig. 2.9. While TALYS and EMPIRE approximately predicted the magnitude of this cross section, the energy at which it peaks is clearly miscalculated by the TALYS exciton model. This is not surprising given the lack of low-lying level information available in ^{135}Ce in the angular momentum range that would be populated in a (p,5n) channel, with data from only a single EC-decay of ^{135}Pr and a pair of (HI,xn) measurements [70–72]. It is worth noting that all three models predict similar intensities for both the (p,6n) and (p,5n) channels, which together account for more than 15% of the total reaction cross section. Due to the strong feeding of the (p,5n) channel up

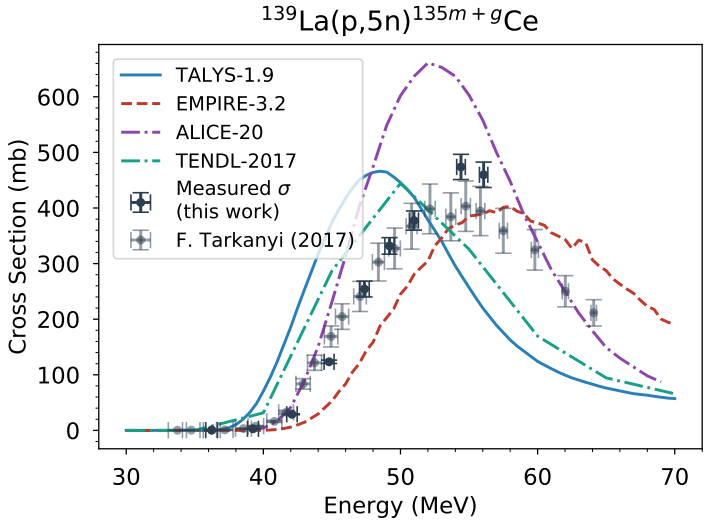

Figure 2.9: Measured cross sections for the ^{139}La(p,5n)^{135}Ce reaction.

to 65 MeV, a higher incident energy beam (at least 70 MeV) would be required to produce ^{134}Ce for medical applications without this major contaminant.

^{139}La(p,3n)^{137m,g}Ce Cross Sections

The decays of both the 34.4 hour isomer and the 9.0 hour ground state in ^{137}Ce were observed, which allows for the measurement of the independent cross sections (*i.e.* the isomer to ground state branching ratio) for this reaction.

The measured cross sections for the ^{139}La(p,3n)^{137m}Ce reaction are plotted in fig. 2.10 and the ^{139}La(p,3n)^{137g}Ce cross sections are plotted in fig. 2.11. In neither case is there a clear "best fit" among the models. Production of both the isomer and ground state shows better agreement with modeling codes than in the (p,5n) and (p,6n) reactions, and possibly an adjustment of the level density model or spin-cutoff parameters would bring the calculations into agreement with the data [73].

^{139}La(p,n)^{139}Ce Cross Section

Measurement of the direct reaction (p,n) was possible using the 80%, 165.85 keV γ emission from the ^{139}Ce ground state decay. This is reported as a cumulative cross section measurement, as the feeding from the short lived isomer ^{139m}Ce ($t_{1/2}$=58 s) could not be quantified before it had completely decayed away.

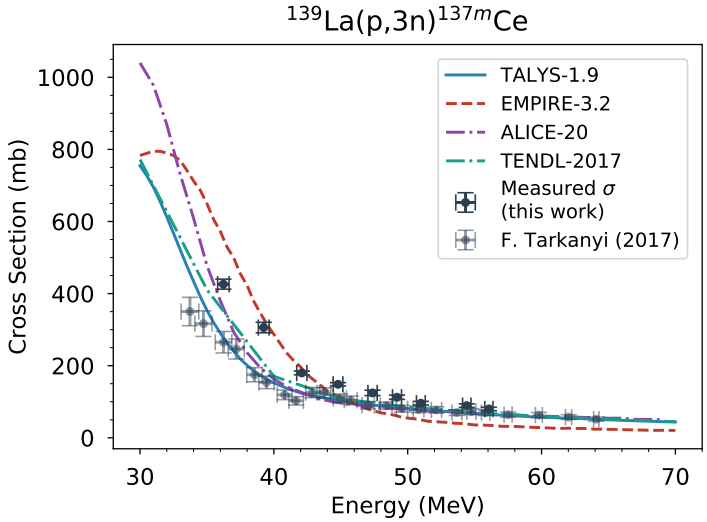

Figure 2.10: Measured cross sections for the ^{139}La(p,3n)^{137m}Ce reaction.

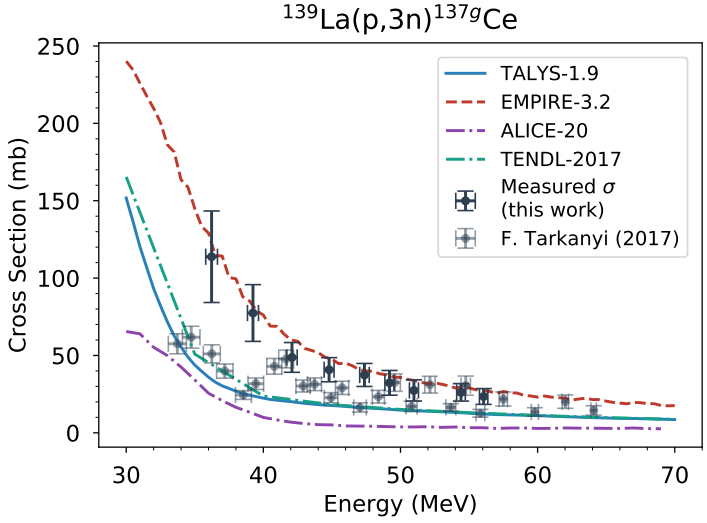

Figure 2.11: Measured cross sections for the ^{139}La(p,3n)^{137g}Ce reaction.

The measured cross sections for the ^{139}La(p,n)^{139}Ce reaction are plotted in fig. 2.12. All three models reproduce the shape of the excitation function, with ALICE being the most accurate at predicting the overall magnitude.

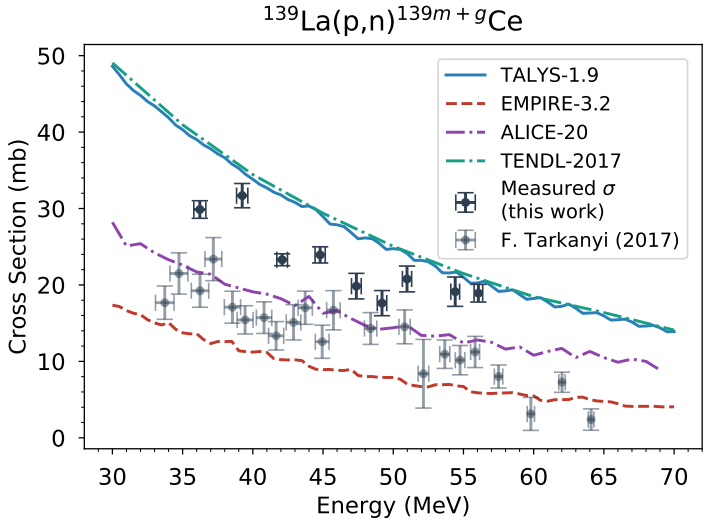

Figure 2.12: Measured cross sections for the ^{139}La(p,n)^{139}Ce reaction.

^{139}La(p,x)^{132}Cs Cross Section

Despite only producing activities on the order of 1–2 Bq, the ^{139}La(p,x)^{132}Cs reaction was measurable because its 6.48 day activity was longer lived than of most isotopes measured in this study, and because the 97.59%, 667.71 keV γ line was well isolated and could be counted for multiple days. This provides an opportunity to study the ability of the models to predict exit channels that represent a smaller component of the overall reaction cross section.

Fig. 2.13 plots the measured ^{139}La(p,x)^{132}Cs cross sections. EMPIRE over-predicted this cross section by almost a factor of 100, whereas the TALYS calculation was far more consistent with measurements, with the ALICE prediction in between the two. The significant discrepancies seen in EMPIRE calculations are common in weakly-fed reaction channels like this one (<0.1% of total cross section), whose behavior are extremely sensitive to more dominant channels [74].

^{139}La(p,x)^{133m,g}Ba Cross Sections

Another reaction where the decays of both an isomer (J_π=11/2$^-$) and the ground state (J_π=1/2$^+$) were observed was the ^{139}La(p,x)^{133}Ba exit channel. The main challenge in this measurement was to identify the ^{133}Ba ground state decays, which had low activities ($\approx$ 0.1 Bq) due to the 10.55 year half-life of that isotope, and due to contaminating peaks in the spectrum for the first few weeks after the irradiation. Fortunately, the isomer has a strong peak (17.69%) at 275.92 keV, which allowed its activity to be measured with <1%

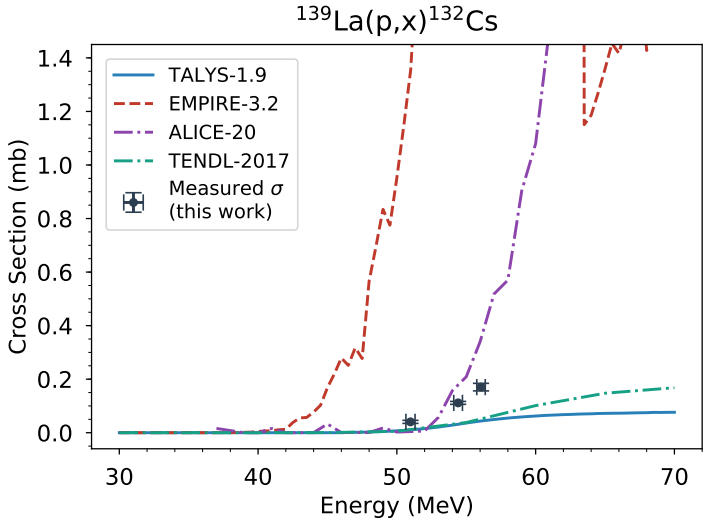

Figure 2.13: Measured cross sections for the ^{139}La(p,x)^{132}Cs reaction.

uncertainty. Multiple long counts enabled the identification of the ^{133}Ba ground state and separation of the ground state activity due to the population of the isomer. Neither ^{133}Ce ($t_{1/2}$=97 (4) m) nor ^{133}La ($t_{1/2}$=3.912 (8) h) were observed in this work, both of which emit strong characteristic γ lines which would have been observable with the HPGe detector used here. Therefore, the cross sections for the ^{139}La(p,x)^{133m,g}Ba reactions are reported in this work as independent.

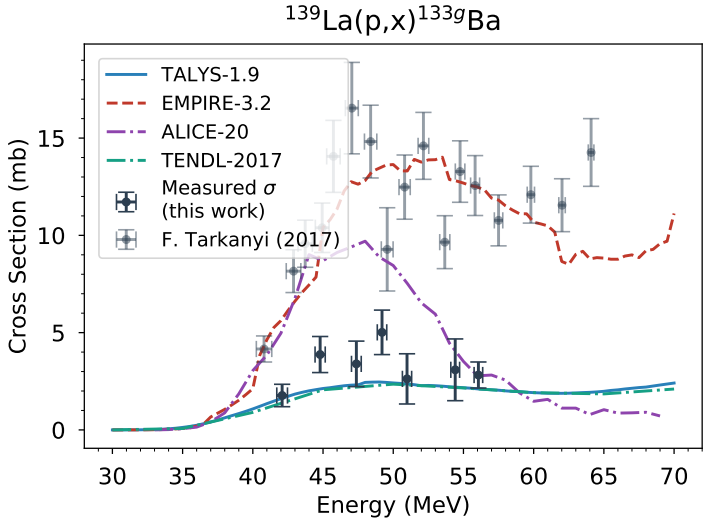

Figure 2.14: Measured cross sections for the ^{139}La(p,x)^{133g}Ba reaction.

Fig. 2.14 plots the measured ^{139}La(p,x)^{133g}Ba reaction cross sections. The relative uncertainties were very large due to the long half-life (10.55 y) [75] and the weak feeding of this channel.

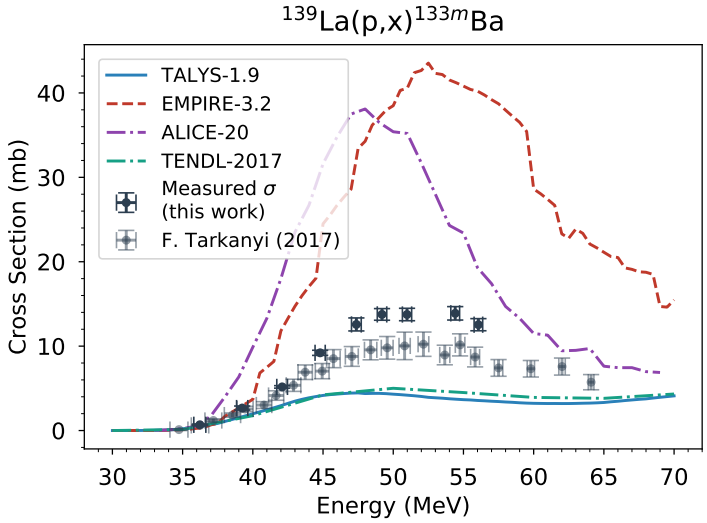

Figure 2.15: Measured cross sections for the ^{139}La(p,x)^{133m}Ba reaction.

Fig. 2.15 plots the measured cross sections for the ^{139}La(p,x)^{133m}Ba reaction. This measurement was much more precise due to the better counting statistics from the 275.925 keV line. Here again the results from EMPIRE were in better agreement with the location of the "compound peak" as a function of energy, although none of the three codes accurately predicted the magnitude of this relatively modest exit channel.

^{139}La(p,x)^{135}La Cross Section

The final cross section measured in the Lanthanum stack was in the ^{139}La(p,x)^{135}La reaction, which has relatively weak γ emissions but was able to be identified using the 1.52%, 480.51 keV γ line. The uncertainties in this measurement were ≈30% because the EoB ^{135}La activities were small compared to the in-feeding from ^{135}Ce decay.

Fig. 2.16 plots the measured cross sections for the ^{139}La(p,x)^{135}La reaction. The EMPIRE model once again predicts a larger magnitude than the other codes for this channel, however there is not a clear "best fit" among the three codes, particularly because of the large uncertainties in the measurements of this work.

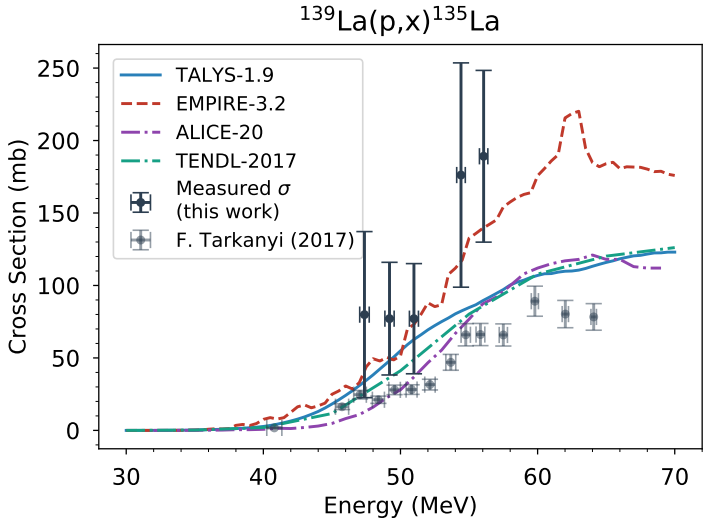

Figure 2.16: Measured cross sections for the ^{139}La(p,x)^{135}La reaction.

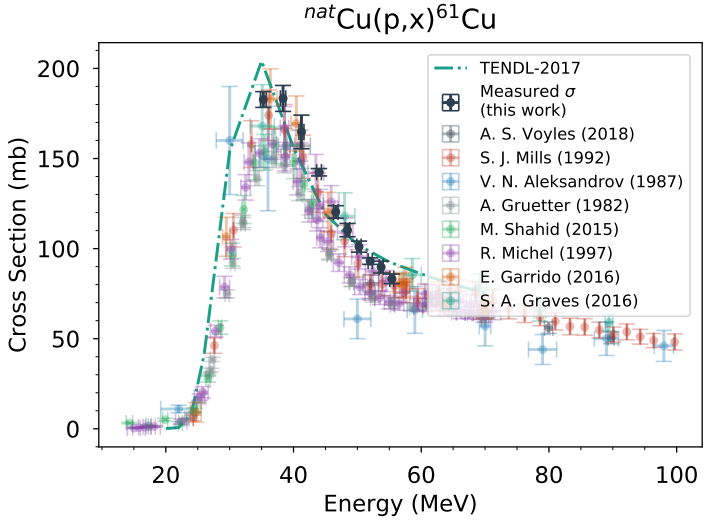

Figure 2.17: Measured cross sections for the ^{nat}Cu(p,x)^{61}Cu reaction [56, 57, 76–81].

^{nat}Cu(p,x)^{61}Cu Cross Section

In addition to their use in proton current determination, γ spectroscopy of the copper monitor foils provided a measurement of the ^{nat}Cu(p,x)^{61}Cu reaction through the observation of the 282.9 keV γ line (12.2%) in ^{61}Cu ($t_{1/2}$=3.339 (8) h). These measurements are plotted in fig. 2.17, in comparison with literature data retrieved from the EXFOR database [56, 57, 76–81].

This measurement is consistent with literature data compiled in EXFOR, both in the shape and magnitude of the excitation function, which builds confidence in the energy and current assignments determined in this work as well as the overall measurement and data reduction methodology. Because the cross sections in this experiment are measured relative to the 2017 IAEA-recommended monitor cross sections, this measurement may be particularly useful if the ^{nat}Cu(p,x)^{61}Cu reaction were to be included in a future evaluation, which may be unlikely due to the potential for secondary neutron contamination in this channel.

2.6 Summary and Conclusions

In this experiment, we measured the cross sections for nine ^{139}La(p,x) reactions using a 57 MeV proton beam stacked-target irradiation at the LBNL 88-Inch Cyclotron. These measurements are compared with the outputs of the TALYS, EMPIRE and ALICE nuclear reaction modeling codes, using default parameters. In many cases, all three codes had difficulty reproducing the magnitude of the cross sections, but TALYS consistently under-predicted the energy of the "compound peak", whereas the EMPIRE and ALICE predictions tended to better reproduce the shape of the excitation functions. Better agreement with the models was found for the more strongly-fed exit channels. This illustrates the current deficiencies in reaction modeling of pre-equilibrium particle emission, which are highly sensitive to the nuclear level density and spin-distribution models employed. This systematic issue will be the subject of a forthcoming publication.

Particular emphasis was placed on the production of ^{134}Ce, a radionuclide with applications as a positron-emitting analogue of ^{225}Ac, a promising medical radionulcide. The results of this study show that in order to produce significant quantities of ^{134}Ce from the ^{139}La(p,6n) reaction, a proton beam of higher energy would be more effective. The highest-energy proton beam available at the LBNL 88-Inch Cyclotron (60 MeV) produces unacceptable quantities of other long-lived cerium radionuclides, which must be avoided for biodistribution studies. Based on the present work, we believe that a proton beam of at least 70 MeV will be required to produce significant activities of ^{134}Ce without major contaminants.

Acknowledgments

We wish to acknowledge our thanks to the operators of the 88-Inch Cyclotron, Brien Ninemire, Nick Brickner, Tom Gimpel and Scott Small, for their efforts in setting a new "high-water mark" for the maximum proton energy extracted from the machine as well as for their assistance and support. We would also like to thank the members of the LBNL Nuclear

Data group and the Nuclear Engineering department at UC Berkeley, who contributed their time and knowledge towards the review of this experiment.

This work has been performed under the auspices of the U.S. Department of Energy by Lawrence Berkeley National Laboratory under contract No. LAB16-1588 NSD. This research is supported by the U.S. Department of Energy Isotope Program, managed by the Office of Science for Nuclear Physics.

Relevant Nuclear Data

Isotope	γ Energy (keV)	I_γ (%)	$T_{1/2}$
^{134}Ce	-	-	3.16 (4) d
^{134}La	604.721 (2)	5.04 (20)	6.45 (16) m
^{135}Ce	265.56 (2)	41.8 (14)	17.7 (3) h
^{137m}Ce	254.29 (5)	11.1 (4)	34.4 (3) h
^{137g}Ce	447.15 (8)	1.22 (3)	9.0 (3) h
^{139g}Ce	165.8575 (11)	79.95 (6)	137.64 (2) d
^{135}La	480.51 (2)	1.52 (24)	19.5 (2) h
^{133m}Ba	275.925 (7)	17.69 (25)	38.93 (1) h
^{133g}Ba	356.0129 (7)	62.05 (19)	10.551 (11) y
^{132}Cs	667.714 (2)	97.59 (9)	6.480 (6) d
^{61}Cu	282.956 (10)	12.2 (22)	3.339 (8) h
^{62}Zn	596.56 (13)	26.0 (20)	9.193 (15) h
^{63}Zn	669.62 (5)	8.2 (3)	38.47 (5) m
^{58}Co	810.7593 (20)	99.45 (1)	70.86 (6) d
^{22}Na	1274.537 (7)	99.940 (14)	2.6018 (22) y
^{24}Na	1368.626 (5)	99.9936 (15)	14.997 (12) h

Table 2.2: Principle γ-ray data from ENSDF [43, 62, 75, 82–91].

Stack Design

Foil Id	Compound	Δx (mm)	$\rho\Delta x$ (mg/cm^2)
SS3	316 SS	0.13	100.48 ± 0.46
La01	La	0.0275	14.59 ± 0.69
Al01	Al	0.027	6.58 ± 0.02
Cu01	Cu	0.029	22.13 ± 0.07
E1	Al	0.254	68.53 ± 5.08
La02	La	0.0278	15.55 ± 0.71
Al02	Al	0.0278	6.67 ± 0.12
Cu02	Cu	0.0293	22.23 ± 0.44
E2	Al	0.254	68.53 ± 5.08
La03	La	0.0315	15.12 ± 0.83
Al03	Al	0.027	6.7 ± 0.03
Cu03	Cu	0.031	22.24 ± 0.07
E3	Al	0.254	68.53 ± 5.08
La04	La	0.0288	14.95 ± 0.66
Al04	Al	0.027	6.68 ± 0.03
Cu04	Cu	0.0317	22.49 ± 0.42
E4	Al	0.254	68.53 ± 5.08
La05	La	0.027	15.07 ± 0.65
Al05	Al	0.027	6.64 ± 0.01
Cu05	Cu	0.0313	22.39 ± 0.42
E5	Al	0.254	68.53 ± 5.08
La06	La	0.026	14.32 ± 0.78
Al06	Al	0.0278	6.66 ± 0.23
Cu06	Cu	0.031	22.22 ± 0.05
E6+E7	Al	0.508	137.06 ± 10.16
La07	La	0.0258	14.21 ± 0.29
Al07	Al	0.0273	6.64 ± 0.12
Cu07	Cu	0.031	22.4 ± 0.05
E8+E9	Al	0.508	137.06 ± 10.16
La08	La	0.0283	15.64 ± 0.28
Al08	Al	0.0273	6.72 ± 0.13
Cu08	Cu	0.032	22.16 ± 1.2
E10+E11	Al	0.508	137.06 ± 10.16
La09	La	0.0268	12.67 ± 0.51
Al09	Al	0.0275	6.65 ± 0.14
Cu09	Cu	0.031	22.2 ± 0.72
E12+E13	Al	0.508	137.06 ± 10.16
La10	La	0.0278	16.14 ± 0.3
Al10	Al	0.027	6.73 ± 0.02
Cu10	Cu	0.031	22.5 ± 0.05
SS4	316 SS	0.13	101.26 ± 0.79

2.7 Additional discussion

Additional discussion of the experimental and analytical details for this work, which were excluded from the published journal article to preserve its scope, are included here.

Thick Target Yields on ^{139}La

It is of interest for bulk isotope production purposes to understand the yields of radionuclides produced in a thick target irradiation. To calculate the yields for a given radionuclide Y_i, with half-life λ_i, in units of activity per unit charge, we must integrate the reaction cross section σ_i, and the inverse stopping power $\frac{dE}{dx}$ over the entire energy range:

$$Y_i(E_{inc}) = \frac{\rho_N \cdot \lambda_i}{e} \cdot \int_0^{E_{inc}} \sigma_i(\epsilon_p) \Big(\frac{d\epsilon_p}{dx}\Big)^{-1} d\epsilon_p$$

where $\rho_N = \frac{\rho \cdot N_A}{M}$ is the number density of the target.

Figure 2.18 shows the thick target yields for the reaction products observed in this experiment, calculated using the TENDL-2015 cross sections.

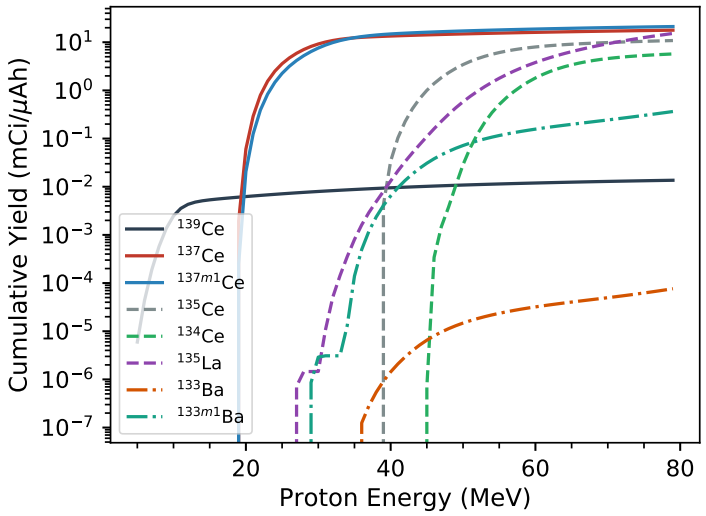

Figure 2.18: Cumulative (thick target) yields for radionuclides produced by proton reactions on ^{139}La.

The main impurity in ^{134}Ce production is likely to be ^{135}Ce, which emits several high-energy γ-rays in its decay. At high energies ^{133}Ce will also be produced, but with a half-life of only 97 (4) minutes, it is less of a concern.

As can be seen in the figure, most of the ^{135}Ce activity is produced in the range of about 40–60 MeV. While it will be impossible to produce ^{134}Ce completely free of ^{135}Ce, the radiopurity can be improved by irradiating a lanthanum target covering the energy window of 55–70 MeV. The radiopurity can be further improved with decay time, as the half-life of ^{135}Ce, 17.7(3) hours, is significantly less than the 3.16(4) day half-life of ^{134}Ce.

From figure 2.18 we see that the thick target yield for ^{134}La reaches about 5.7 mCi/µAh. If we consider an isotope production facility like LANL IPF [92], with about 250 µA of beam current, and a three day irradiation, a thick lanthanum target would produce about 75 Ci of ^{134}Ce. Considering that typical PET scans require on the order of 10 mCi per treatment, this three day irradiation could produce enough activity for up to 7,500 treatments.

Chapter 3

Characterizing the Secondary Neutron Spectrum from Deuteron Breakup

3.1 Introduction

THICK target deuteron breakup is one of the most intense accelerator-based sources of neutrons in the range of ≈10–100 MeV, with the potential for numerous scientific and industrial applications. At $\epsilon_d = 40$ MeV on a beryllium target, approximately 9% of the incident deuteron beam breaks up, and is "converted" into a forward-focused neutron beam. Another appealing characteristic of deuteron breakup is that the average energy of neutrons emerging from the reaction is approximately half of the incident deuteron energy. The fact that the energy and intensity of the outgoing neutron distribution are (approximately) proportional to the energy and intensity of the incident deuteron beam means that the neutron spectrum can be tuned to meet the requirements of a particular application.

However there is a pressing need for improving the characterization of the energy and angle distributions for neutrons from thick target deuteron breakup. Many of the available literature data are not of sufficient quality for the applications desired, and are often inconsistent with one another. In addition, most of the modeling efforts associated with deuteron breakup are either focused on (d,p) transfer reactions in thin targets, rather than on thick target neutron yields, or are simply inaccurate over the energy range and target materials appropriate for applications.

In this chapter, we present a parameterized, hybrid model for deuteron breakup that has been fit to a selection of literature data on thick beryllium targets, spanning an energy

range of ϵ_d = 16–50 MeV. The model was shown to extrapolate well to higher energies, as well as to other targets in a similar mass range. We also present new measurements of the double-differential neutron spectra acquired at ϵ_d = 33 and 40 MeV, which were performed using the time-of-flight and foil activation techniques.

Applications of Deuteron Breakup

The tunable energy spectrum and relatively high intensity of deuteron breakup make it an attractive neutron source for a variety of applications. One application that we will examine in this work is for isotope production, where it has the potential to play a unique role in comparison to other neutron sources. Nuclear reactors are very intense neutron sources, but are not tunable in energy and are generally only practical for (n,γ) reaction pathways. Neutron generators (both deuterium-deuterium and deuterium-tritium) are a relatively low cost source of high energy neutrons, but the energy is fixed and the neutron intensity is comparably low. Spallation neutron sources have a very high intensity, however they emit a broad range of neutron energies, only a small selection of which are likely useful for isotope production [93].

In comparison, the spectrum from a deuteron breakup neutron source could be optimized for a specific (n,p), (n,2n), (n,3n) or (n,α) reaction, selectively populating one isotope with a relatively high radiopurity. Also, because there is a strong energy-angle correlation in the breakup spectrum, different isotope production targets could be arranged at different angles, enabling simultaneous radionuclide production. In this chapter we will present cross section measurements of the ^{64}Cu, ^{67}Cu, ^{44}Sc and ^{47}Sc medical isotopes using a deuteron breakup source, however many other isotope production pathways are possible.

There are also many potential scientific applications of deuteron breakup. Because the neutron production is coupled to the incident deuteron beam, a pulsed accelerator (such as a cyclotron or linear accelerator) can be used to perform nuclear physics measurements using the time-of-flight (ToF) technique. This is useful for measuring reaction cross sections as a function of the incident neutron energy, for which there is a paucity of data in the fast neutron range of several MeV [94]. If the deuteron beam is scaled up significantly in intensity, the spectrum is suitable for neutron damage studies of fusion reactor materials [95], or for electronics damage and human dose considerations for space exploration [96]. While not a direct application of deuteron breakup, modeling the breakup reaction is important for interpreting (d,p) reaction data, often used in surrogate nuclear reactions for targets that are either difficult to acquire, or have a low reaction cross section [97]. There are also potential applications for active interrogation studies, or neutron induced transmutation of nuclear waste [98].

Background

Deuteron breakup has a long history of study, beginning in the 1930's when Oppenheimer proposed that deuterons having a kinetic energy larger than their nuclear binding energy (E_d = 2.225 MeV) could be disintegrated through Coulombic interactions in matter [99]. In the 1940's, measurements by Helmholtz, McMillan and Sewell [100] of Uranium target bombardment with high energy deuterons showed that neutrons from this process were emitted at approximately half the incident deuteron energy, and that this process was very forward-focused. Dancoff and Serber proposed two competing theories explaining these observations, the former based on Coulomb excitation of the deuteron [101], and the latter being a nuclear process in which the proton is "stripped" away from the neutron [102]. Dancoff also showed that for low-Z nuclei, the Coulomb breakup cross section would be much smaller than for the stripping process. This assertion is also maintained by more recent theoretical work [103], and is fairly intuitive as the cross section for Coulomb excitation is proportional to Z^2.

The theories of Dancoff and Serber represent the two competing reaction mechanisms responsible for deuteron breakup. The Dancoff theory of Coulomb excitation is one form of *elastic breakup* (EB), where no energy or particles are transferred to the target nucleus. In this case the breakup is not induced by a nuclear reaction, however nuclear-elastic breakup is also possible. The Serber theory of proton stripping is an example of a *nonelastic breakup* (NEB) reaction, in which either energy, a particle, or both are transferred to the target nucleus, which necessarily occurs through a nuclear interaction.

The essence of the Serber stripping theory is, as summarized by Potel *et al.* [97], "the product of the square of the Fourier transform of the ground state wave function of the [deuteron] projectile and the total reaction cross section of the unobserved fragment", which is the proton in this case. More simply, it assumes that the neutron momentum distribution before and after the interaction, in which the proton is stripped away from the deuteron, remains the same. This reproduces the basic kinematic behavior experimentally observed for breakup on light targets: that the neutron distribution emerges with an average energy of one-half that of the incident beam, and the angle distribution becomes more forward-focused as the incident energy is increased.

A more rigorous treatment of this process was given using direct reaction theory, in the works of Ichimura, Austern, and Vincent (IAV) [104] using the post-form of the distorted-wave Born approximation (DWBA) and Udagawa and Tamura (UT) [105] using the prior DWBA form. These theories preserve the essentials of the Serber model, but account for diffraction effects caused by interactions of the elastic breakup channel with the target nucleus [97]. More modern approaches make use of three-body descriptions of breakup, or will perform coupled-channel calculations which are capable of computing multi-step reaction

processes to high orders of accuracy. All of these described methods make use of optical-model potentials for the deuteron-target interacting system, the parameters of which can be tuned to reproduce experimental results. Other recent efforts in breakup modeling include semi-empirical formulae fitted to experimental data, such as the works of Kalbach [106] and Avrigeanu [107]. However these models have been shown to have poor agreement with neutron yield data on light targets [108], due to the fact that they were mostly fit to (d,p) reaction data on medium-mass nuclides. This served as the motivation for development of the hybrid breakup model presented in this work, which is specifically tuned to reproduce neutron yield data on low-Z targets, with an eye towards using the forward-focused neutrons as a beam in their own right.

In addition to (elastic and nonelastic) breakup, there are other nonelastic reaction processes which may contribute to neutron production. These are compound nucleus formation, pre-equilibrium, and direct reactions (aside from nonelastic breakup) leading to excited states in the product nucleus. It is argued that due to the different time scales for these reaction mechanisms, they can be treated as an incoherent summation, such that the resulting spectra from each mechanism can simply be added together [103]. On this basis, the modeling of these processes are generally performed independently from breakup, and can be calculated with a standard nuclear reaction model code (TALYS, EMPIRE, etc.) [54, 55].

As far as experimental measurements of breakup are concerned, most effort has been focused on (d,p) reaction data on medium-mass targets, often with the goal of providing nuclear structure insight. This is motivated by two factors. Experimentally, protons can be detected with much higher efficiency and energy resolution than neutrons, with the use of silicon charged particle detectors. This enables measurements on rare or enriched target materials, that may not be available in quantities larger than a few milligrams. The superior energy resolution means that more details of the underlying nuclear physics may be revealed, as reactions to specific states can be observed. The other motivating factor is that (d,p) reactions can act as a surrogate to (n,γ) reactions, which are important for a wide variety of applications [109]. The interpretation of these surrogate measurements is one of the principal motivations behind the development of more comprehensive theories for deutron breakup, such as the work of Potel *et al.* [97].

However in this work, we are primarily focused on applications for deuteron breakup as a high intensity, variable energy neutron source. For this purpose, of course (d,n) rather than (d,p) measurements are required, but also it is of importance that the measurements are on low-Z target materials, and preferably in the range of ϵ_d = 10–200 MeV. This is because the neutron yields improve significantly with increasing deuteron range. Lower Z targets, and higher energy deuterons, will have comparatively higher range. Above $\epsilon_d \approx$200 MeV, other reaction mechanisms such as spallation may become significant, which are not the focus of this work. Within this scope, most of the literature measurements are on thick beryllium

targets, in the energy range of 16–55 MeV. The majority date to the 1970's, and were performed with the motivation to use breakup as a fast neutron source in cancer therapy [110]. Unfortunately many of these measurements are discrepant with one another, and most were only performed at forward angles, motivating an improved set of measurements at multiple energies and angles.

3.2 Parameterization of the Hybrid Breakup Model

The majority of reported experimental neutron spectra from deuteron breakup are neutron yields from thick targets. More specifically, they are the neutron production cross sections integrated over the entire range of the deuteron for a given incident energy, rather than energy differential measurements. This includes neutron production from inelastic reactions other than breakup. While having thick target yields is somewhat convenient from the applications perspective of using deuteron breakup as a neutron source, it means that forward modeling will be required to extract the neutron production cross sections. The total double-differential neutron yields from a thick target can be calculated according to

$$\frac{d^2Y(E_n,T_e,\theta)}{dE_n,d\Omega} = \frac{\rho_N}{e}\int_0^{E_d}\tau(\epsilon_d)\frac{d^2\sigma(\epsilon_d,\theta)}{d\Omega dE_n}\Big(\frac{d\epsilon_d}{dx}\Big)^{-1}d\epsilon_d \tag{3.1}$$

where $\rho_N = \frac{\rho\cdot N_A}{M}$ is the number density of the target, $\tau(\epsilon_d)$ is a parameter representing the attenuation of the deuteron beam from the incident energy E_d down to ϵ_d, $\frac{d\epsilon_d}{dx}$ is the deuteron stopping power in the target, and $\frac{d^2\sigma(\epsilon_d,\theta)}{d\Omega dE_n}$ is the double-differential neutron production cross sections that we are attempting to unfold. At very high energies, we would also need to account for neutron attenuation within a thicker target, as well as tertiary neutrons produced from the breakup proton flux. However, these contributions are likely to be quite small at the energies of interest to this work.

In order to build a successful model for the neutron production cross sections $\frac{d^2\sigma(\epsilon_d,\theta)}{d\Omega dE_n}$, we must perform an iterative procedure in which the cross sections are predicted, the thick target yields are calculated from these, and then the model is adjusted to better reproduce the yield data. To perform this optimization, the model requires adjustable parameters. While one could adjust optical model parameters in a DWBA calculation, we have instead opted to use a parameterzied version of the Serber theory [102]. In addition to the relative simplicity of the Serber theory, there are two motivating factors for using this model. One is that it has already been shown that for low-Z target nuclei (relevant to neutron production targets), the nonelastic breakup component is almost negligible [103], such that there is little improvement in accuracy expected from a DWBA calculation. The exception to this is at low energies (< 15 MeV), however at these energies, the short range of the deuteron limits

the resulting neutron flux, making it generally outside the scope of the isotope production applications which are the focus of this work. The other advantage to the Serber model is that it does not require a re-tuning of optical model parameters for each target nucleus [111], which would likely be required of DWBA calculations as global optical model potentials (OMPs) such as the Koning-Delaroche OMPs [112] are not valid for light nuclei such as ^{6,7}Li and ^{9}Be.

With this in mind, we will first describe the parameterized breakup model, and then discuss the parameter adjustments and fitting to experimental data. As mentioned previously, due to the different time scales of the various neutron producing mechanisms involved, we can divide the cross section into an incoherent sum of the following inclusive cross sections

$$\frac{d^2\sigma}{d\Omega dE_n} = \frac{d^2\sigma_{BU}}{d\Omega dE_n} + \frac{d^2\sigma_{CM}}{d\Omega dE_n} + \frac{d^2\sigma_{PE}}{d\Omega dE_n}$$

where the subscripts BU, CM and PE refer to breakup (via proton stripping), compound-fusion evaporation reactions, and pre-equilibrium reactions. Direct reactions were excluded from this study because they only contribute significantly to the neutron yields at low energy, which is outside the scope of a neutron production target for applications like isotope production.

For the breakup cross section, it was assumed that the energy and angle distributions were independent, and therefore the cross section could be separated into a total breakup cross section σ_{BU}, and probability distributions for the outgoing neutron energy ($P_{BU}(E_n)$) and angle ($P_{BU}(\theta)$) according to

$$\frac{d^2\sigma_{BU}}{d\Omega dE_n} = \sigma_{BU}(\epsilon_d) P_{BU}(E_n) P_{BU}(\theta)$$

According to the Serber model, the stripping cross section should be proportional to the target nuclide radius, or $R = r_0 A^{1/3}$. However, Serber did not include any dependence on the incident deuteron energy. Therefore, the Serber formula was combined with the energy dependence from the semi-empirical breakup model by Kalbach [113] to obtain

$$\sigma_{BU}(\epsilon_d) = 57.2 \cdot \frac{(A^{1/3} + 2^{1/3})}{1 + e^{(22.3 - \epsilon_d)/\eta_{BU}}} \text{ (mb)}, \quad \eta_{BU} = 9.4 \text{ (MeV)}$$

A comparison of the total breakup cross section with the neutron production cross sections from pre-equilibrium and compound reactions can be seen in figure 3.1. These results show that above approximately 20 MeV, breakup is the dominant contributor to neutron production.

The neutron energy and angle distributions for breakup were taken from the opaque nucleus approximation in the Serber theory. However the characteristic widths of these

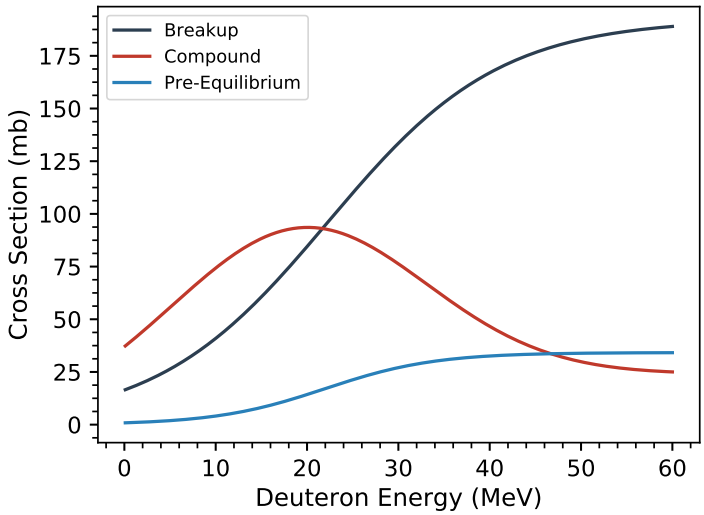

Figure 3.1: The total neutron producing cross sections for deuteron breakup, compound (evaporation) and pre-equilibrium reactions.

distributions were modified to reproduce the experimental measurements. The resulting energy probability distribution is given by

$$P_{BU}(E_n) = \frac{(\epsilon_d - E_c)\cdot w_d}{\pi\left[\left(E_n - \frac{1}{2}(\epsilon_d - E_c)\right)^2 + w_d\cdot(\epsilon_d - E_c)\right]^{3/2}}, \quad w_d = 0.37\cdot E_B$$

where E_c is the Coulomb potential at a separation of $R = r_0(A^{1/3} + 2^{1/3})$. This was not included in the original Serber theory, however it accounts for the slight shift in the centroid energy observed in measurements, particularly of higher Z targets, due to Coulomb repulsion of the incident deuteron.

The angle distribution from the Serber model is given by

$$P_{BU}(\theta) = \frac{\theta_0}{2\pi(\theta_0^2 + \theta^2)^{3/2}}, \quad \theta_0 = 0.72\cdot\sqrt{\frac{E_B}{\epsilon_d - E_c}}\cdot\left(1 - \frac{\epsilon_d}{8m_dc^2}\right)$$

where the relativistic correction term $\frac{\epsilon_d}{8m_dc^2}$ is generally negligible at the deuteron energies applicable to this model. Not included in these equations, but included in the numerical implementation of the model, is a normalization constant such that $\int_{E_n} P(E_n)dE_n = 1$ and similarly $\int_\theta P(\theta)d\theta = 1$.

Figure 3.2 shows these (un-normalized) distributions for the breakup reaction. Characteristic of the breakup process, the energy distribution is centered at half the incident energy (minus the Coulomb potential), with a width that increases with increasing energy. The an-

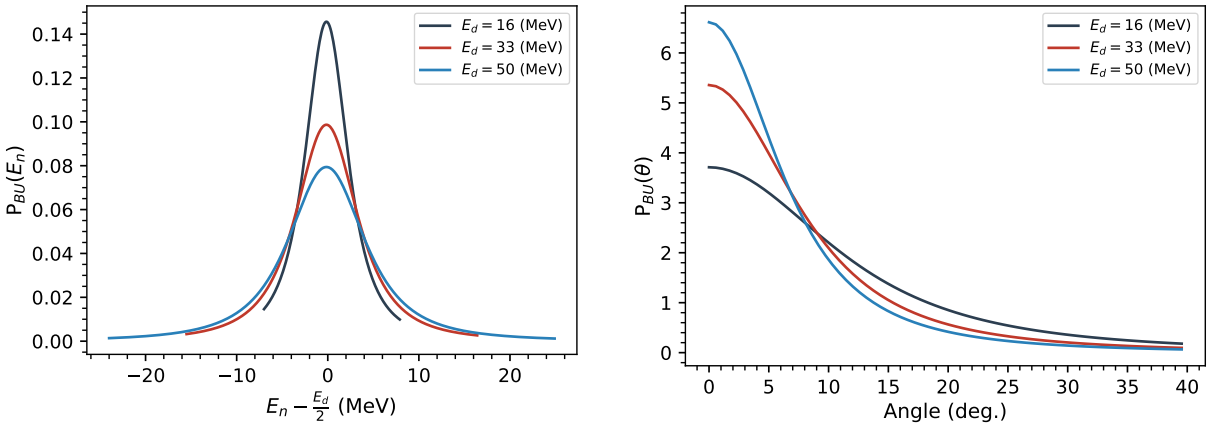

Figure 3.2: Energy (left) and angle (right) distributions of the outgoing neutrons from deuteron breakup, for various incident deuteron energies.

gular distribution is very forward peaked, with the majority of breakup neutrons emerging below about 20°. This angular distribution sharpens as the energy is increased.

However breakup is, of course, not the only reaction responsible for neutron production. While the pre-equilibrium and compound nuclear reactions could be calculated using a standard nuclear model code such as TALYS [54] or EMPIRE [55], for the purposes of a parametric study we have made use of semi-empirical models for these mechanisms, largely inspired by the work of Kalbach [113].

Similar to the breakup cross section, the compound and pre-equilibrium cross sections were assumed to have separable energy and angle distributions, according to

$$\frac{d^2\sigma_{CM,PE}}{d\Omega dE_n} = \sigma_{CM,PE}(\epsilon_d)P_{CM,PE}(E_n)P_{CM,PE}(\theta)$$

The total compound neutron production cross section was given the following parameterization in terms of deuteron energy

$$\sigma_{CM}(\epsilon_d) = 80.6 \cdot \left[\exp\Big(-\frac{1}{2}((18-\epsilon_d)/14)^2\Big) + \frac{0.3}{1+e^{(18-\epsilon_d)/7}}\right] \text{ (mb)}$$

where the shape was determined by fitting to the output of a TALYS calculation for ^{9}Be(d,xn), and the magnitude was determined by a fit to experimental data.

The total pre-equilibrium neutron production cross section was parameterized in a similar manner according to

$$\sigma_{PE}(\epsilon_d) = \frac{34.2}{1+e^{(22-\epsilon_d)/6}} \text{ (mb)}$$

e_a	$\frac{\epsilon_d}{2} + S_b(A+1, Z+1)$
e_b	$\epsilon_d + S_b(A, Z) - E_B$
E_1	$\min(e_a, 130\text{ MeV})$
E_3	$\min(e_b, 41\text{ MeV})$

Table 3.1: Kalbach energy parameters for a.

The systematics of compound and pre-equilibrium neutron angular distributions have been thoroughly characterized in the semi-empirical formulations by Kalbach and Mann [114], and therefore we will adopt their parameterization according to the following relation

$$P_{CM}(\theta) = \frac{a}{2 \cdot \sinh(a)} \cdot \Big(\exp\Big(a \cdot \cos(\theta')\Big) + \exp\Big(- a \cdot \cos(\theta')\Big)\Big)$$

where θ' is the center-of-mass emission angle, which in the non-relativistic case can be determined by

$$\theta'(\epsilon_d) = \arctan\Big(\Big(1 + \frac{\epsilon_d}{(2+A) \cdot 931.5\text{ MeV}}\Big) \cdot \tan(\theta - \frac{\pi}{2})\Big) + \frac{\pi}{2}$$

where θ is the neutron emission angle in the lab frame, and the phase shift $\frac{\pi}{2}$ has been introduced to correctly map the arctan function over the angular range from 0 to π.

The pre-equilibrium angular distribution is given by a similar formula

$$P_{PE}(\theta) = \frac{a}{\sinh(a)} \cdot \exp\Big(a \cdot \cos(\theta')\Big)$$

where the Kalbach "little a" parameter is calculated according to the following empirical formulae

$$a = 0.04 \cdot \frac{E_1 \cdot e_b}{e_a} + 1.8 \times 10^{-6} \cdot \Big(\frac{E_1 \cdot e_b}{e_a}\Big)^3 + 3.35 \times 10^{-7} \cdot \Big(\frac{E_3 \cdot e_b}{e_a}\Big)^4$$

with the energy dependent parameters given by table 3.1.

$S_b(A, Z)$ is defined as

$$S_b = s_1 - s_2 - s_3 + s_4 - s_5 + s_6$$

with the constants s_i being calculated according to table 3.2.

For the neutron emission on beryllium, the compound and pre-equilibrium angular distributions that best fit the experimental data were obtained by modifying the a parameter with $a_{CM} = 1.1 \cdot a$, and $a_{PE} = 1.8 \cdot a$.

i	s_i
1	31.36
2	$28.07 \cdot \left(\frac{(N+1-Z)^2}{A+2} - \frac{(N-Z)^2}{A}\right)$
3	$18.56 \cdot \left((A+2)^{2/3} - A^{2/3}\right)$
4	$33.22 \cdot \left(\frac{(N+1-Z)^2}{(A+2)^{4/3}} - \frac{(N-Z)^2}{A^{4/3}}\right)$
5	$0.717 \cdot \left(\frac{(Z+1)^2}{A^{1/3}} - \frac{Z^2}{A^{1/3}}\right)$
6	$1.211 \cdot \left(\frac{(Z+1)^2}{A+2} - \frac{Z^2}{A}\right)$

Table 3.2: Kalbach constants for a.

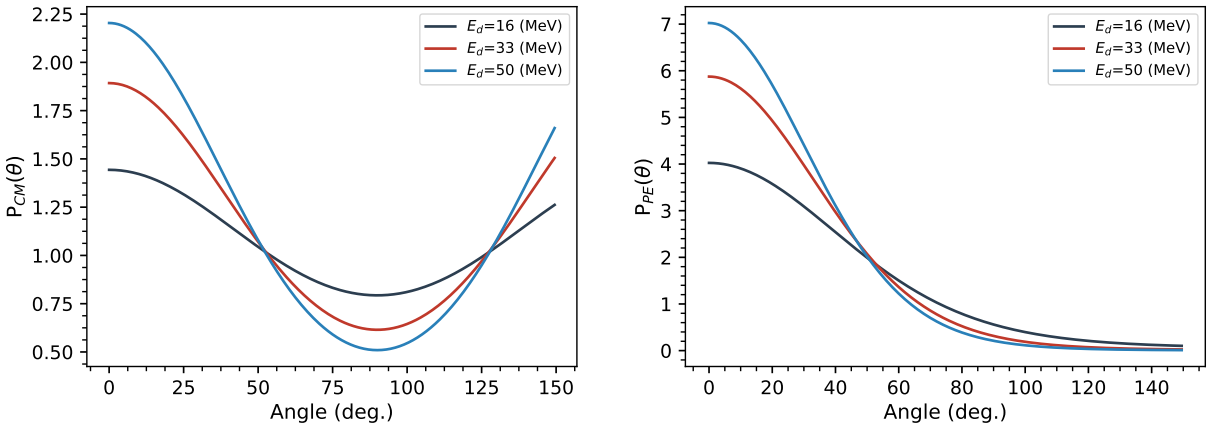

Figure 3.3: Angular distributions of neutrons from compound (left) and pre-equilibrium (right) reactions, as given by the Kalbach systematics.

Figure 3.3 shows these calculated distributions as a function of the neutron emission angle in the lab frame. The systematic behavior of the two, as given by the Kalbach parameterization, are strikingly different. The pre-equilibrium angular distribution is very forward focused, although not nearly so much as for the breakup reaction. This distribution becomes more sharply peaked as the incident deuteron energy increases. The compound distribution, however, is peaked at both forward and backward emission angles, and the degree of anisotropy increases with increasing deuteron energy.

The energy distribution of these neutron emission spectra were calculated using a Watt distribution, according to

$$P_{CM,PE}(E_n) = \sinh\left(\sqrt{2 \cdot E_n}\right) \cdot \exp\left(-\frac{E_n}{kT_{CM,PE}}\right)$$

where kT is the nuclear temperature associated with each process. The Watt distribution

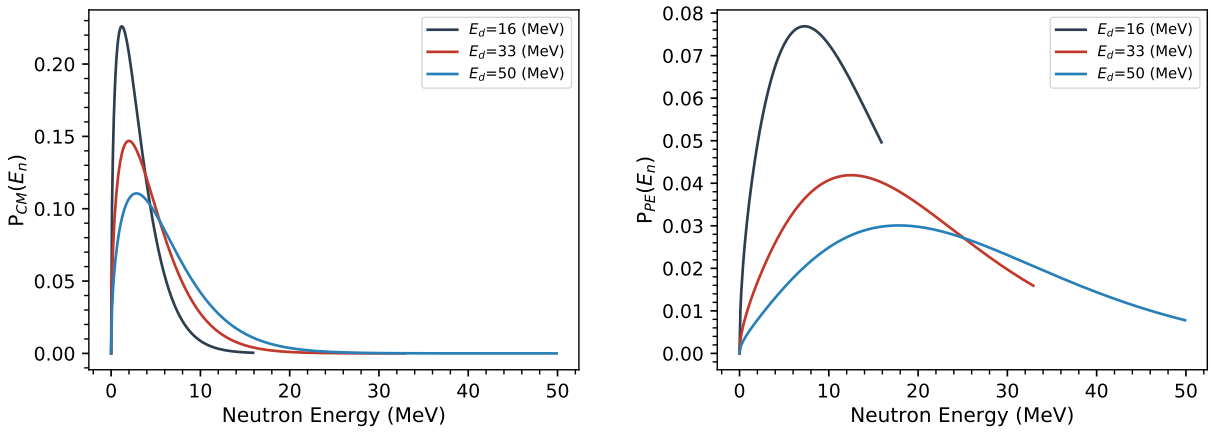

Figure 3.4: Energy distributions of compound (left) and pre-equilibrium (right) reactions, determined using a modified moving-source parameterization.

was found to reproduce the experimental results better than the Maxwell-Boltzmann distribution, which is unsurprising given that it is characteristic of a moving source that emits particles with Maxwell-Boltzmann distribution in the center-of-mass frame. Once again, this distribution was normalized (in the numerical implementation) such that $\int_0^{\epsilon_d} P_{CM,PE}(E_n)dE_n = 1$.

The energetic dependence of the nuclear emission temperature was loosely based on the parameterization of the moving-source model [115], with

$$kT_{CM} = 0.1 + 0.27 \cdot \sqrt{\epsilon_d + Q} \text{ (MeV)}$$

and

$$kT_{PE} = 0.75 + 0.63 \cdot \sqrt{\epsilon_d + Q} \text{ (MeV)}$$

where Q is 4.36 MeV for ^{9}Be(d,n).

Figure 3.4 plots the (normalized) energy distributions for compound and pre-equilibrium emission. These give the expected trends that pre-equilibrium emission will result in a comparably higher average energy, and that the distribution spreads out as the deuteron energy increases. For a more rigorous calculation of these distributions, one could make use of a Hauser-Feshbach calculation [116] for the compound spectrum and an exciton-model calculation [117] for the pre-equilibrium distribution. However this was not performed here for the sake of simplicity, which is justified by the fact that these reactions form a fairly minor contribution to the breakup spectrum, particularly at the energies relevant to applications such as isotope production.

It should be noted that the black-body temperature kT is not an absolute temperature in any moving reference frame, and there will be an apparent temperature shift given by the relativistic correction

$$T'(\theta', \epsilon_d) = \frac{T}{\gamma \cdot \Big(1 - \beta \cdot \cos(\theta')\Big)}$$

where $\beta = \frac{v_{A+d}}{c}$ is the relativistic velocity for the compound system, and θ' is again the neutron emission angle in the center of mass frame.

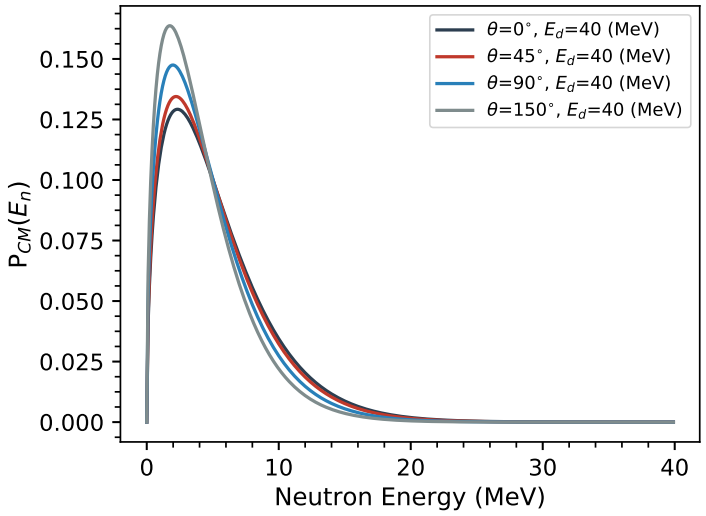

Figure 3.5: Example of relativistic corrections to the energy distribution of neutrons from the compound (evaporation) reaction.

The consequence of this correction is a relatively small shift in the energy distribution, however it does induce a correlation between the outgoing neutron emission energy and angle. Figure 3.5 shows the impact of this correction for 40 MeV deuterons at multiple emission angles (in the laboratory frame). The magnitude of this correction will increase with increasing deuteron energy, however the relative impact on the spectrum will be small as neutrons from the breakup process tend to dominate the spectrum at higher deuteron energies.

This forms the basis of the model for the double-differential neutron production cross sections. Now all that remains in order to calculate thick target yields is an expression for the attenuation parameter τ. Given the expected linear trajectory of deuterons in a material down to energies below the threshold for breakup, the attenuation parameter can be quite simply calculated as the integration of the total reaction probability, according to

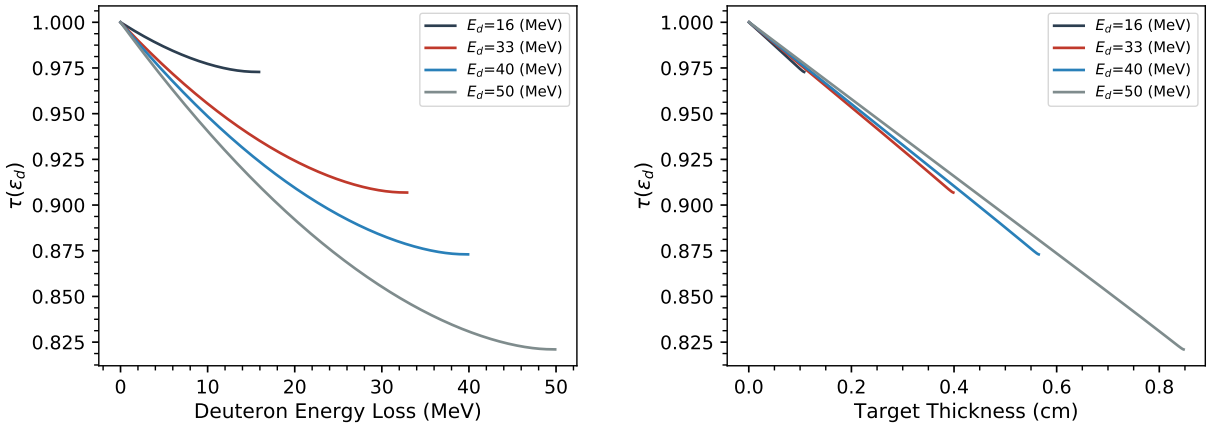

Figure 3.6: Deuteron attenuation factor (τ) as a function of the deuteron energy loss in the target (left) and the target thickness (right) for a range of incident energies.

$$\tau(\epsilon_d) = \exp\Big(-\rho_N \int_{\epsilon_d}^{E_d} \sigma_T(\epsilon') \Big(\frac{d\epsilon'}{dx}\Big)^{-1} d\epsilon' \Big)$$

where ρ_N is the number density of the target, σ_T is the total reaction cross section (not just neutron producing reactions), E_d is the original deuteron energy incident on the target, and $\frac{d\epsilon'}{dx}$ is the stopping power.

This total reaction cross section can be interpolated from an evaluation such as TENDL, however we will make use of the following simple relation

$$\sigma_T(\epsilon') = \sigma_{BU}(\epsilon') + r_0^2(A^{1/3} + 0.8)^2 \cdot \Big[c_1 \cdot e^{-\epsilon'/a_1} \cdot (1 - e^{-\epsilon'/a_2})\Big]$$

where the parameters $c_1 = 5.643$, $a_1 = 131.3$ MeV, and $a_2 = 1.354$ MeV were derived from a fit to experimental data. In this case σ_{BU} is the contribution from breakup only, i.e. not including compound or pre-equilibrium reactions.

The attenuation parameter τ can be seen in the plots of figure 3.6 as a function of both the target thickness, and the deuteron energy loss in the target. A significant feature of these plots is that even at higher incident energies, the deuteron beam is not extremely attenuated. This leads to a general trend in the thick target deuteron breakup measurements: that the breakup spectrum for a given energy is (almost) the cumulative sum of the breakup spectra for all the energies below it. For example, the neutron spectrum from 40 MeV deuterons should be equal to the 30 MeV spectrum, plus the additional flux of the deuterons ranging from 40 down to 30 MeV. This makes inconsistencies in the literature data very clear. If the reported yields at 30 MeV are higher than at 40, one of the two measurements must be incorrect.

Data Selection and Fitting

The emphasis of this work is on reliably calculating double-differential thick target neutron yields on beryllium. Lithium and carbon targets would have also been appropriate, as the stripping reaction mechanism should be the dominant contribution to breakup for low-Z nuclides, however there are fewer experimental data on these targets. Instead, while the data on lithium, carbon (and copper) targets were not included in the fitting procedure, they were used to evaluate the ability of the model to be extrapolated outside the range of where it was fit. It may be of value to perform the same fitting procedure on lithium targets, as these are interesting because they produce about a 30% higher neutron yield per unit of beam current, due to the increased deuteron range in lithium. Furthermore, there are existing high-power liquid lithium targets that are being used for neutron generation for astrophysical applications [118]. However this analysis will be left for a future study.

In total, the measurements of five authors were found with thick target neutron yield data on beryllium targets in the relevant energy range. The most recent, Harrig *et al.*, performed very precise measurements using the double time-of-flight technique at 16 MeV, at forward angle [119]. The use of this method allowed Harrig to measure significantly lower neutron energies than other authors, which all used the (single) time-of-flight method. The works of Saltmarsh [120] and Meulders [110] were quite valuable, because they contained measurements at multiple angles. This is important for assessing the contributions from compound and pre-equilibrium reactions, as these mechanisms will be observed relatively free of breakup neutrons at large angles. However the 33 MeV data of Meulders was not used in the fitting procedure, as it was nearly the same in magnitude as the 40 MeV Saltmarsh measurements, which seemed to be more in line with the rest of the data than the Meulders 33 MeV results. Similarly, the Schweimer data [121] was interesting because it contained a measurement at 54 MeV, but had to be left out of the fitting because the 40 MeV Schweimer measurement was about 40% lower than Saltmarsh. Weaver [122] had multi-angle measurements at 16 MeV, however because the present study does not include direct reactions, these low energy points were highly discrepant. Also, there was about a 25% discrepancy between Weaver and Harrig/Meulders. While not directly used for the fitting, these data are compared to the resultant model in the next section.

Six of the parameters from the proposed model were selected to be adjusted in the fitting procedure. These were the scaling parameters for the magnitudes of the breakup, compound and pre-equilibrium reactions, a parameter each for the widths of the breakup energy (w_d) and angle distributions (θ_0), as well as a slope parameter η for the breakup total cross section.

These parameters were fit using the scaling constants c_i according to

$$\frac{d^2\sigma(c_1,\ldots,c_6)}{d\Omega dE_n} = c_1 \cdot \frac{d^2\sigma_{BU}(c_2\cdot\eta_{BU}, c_3\cdot w_d, c_4\cdot\theta_0)}{d\Omega dE_n} + c_5 \cdot \frac{d^2\sigma_{CM}}{d\Omega dE_n} + c_6 \cdot \frac{d^2\sigma_{PE}}{d\Omega dE_n} \tag{3.2}$$

where the calculation with all $c_i = 1$ returns the cross sections from the previously described model. This 6-parameter function will be useful for the neutron activation analysis measurements performed in this work, as it can be used to deduce the measured spectrum without the issue of solving an underdetermined system typical of spectral unfolding techniques.

Determining the values of c_i which best fit the literature data is done by computing the thick target yields using equation 3.1, and iteratively adjusting c_i to improve their fit to the experimental yields. It is worth noting that this fitting procedure is performed once for all literature data, at all energies and angles together, rather than for a single spectrum at a time. This reduces the likelihood of "overfitting", improving the predictive power of this model.

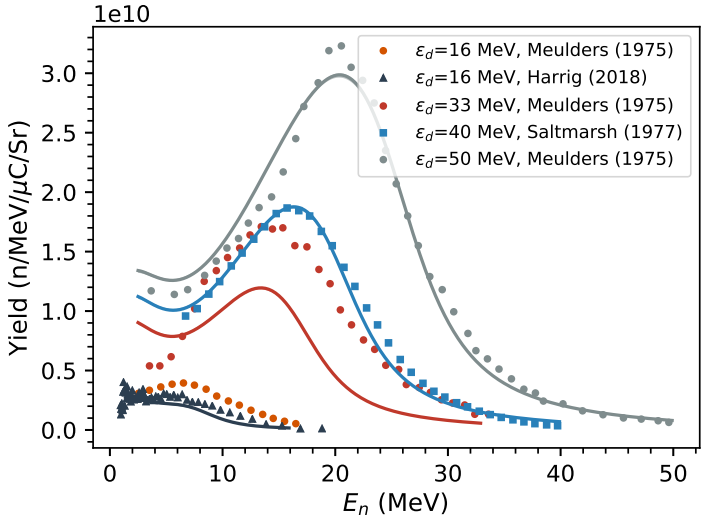

Figure 3.7: Results of the fit to literature data measured at $\theta = 0°$, from $\epsilon_d = 16$–50 MeV. Data from Meulders (1975), Saltmarsh (1977) and Harrig (2018).

The results of this fitting procedure to the selected literature data can be seen in figure 3.7 at forward angles, and in figure 3.8 at $\epsilon_d = 40$ and 50 MeV for multiple outgoing angles.

In general, the agreement is quite good. The results seem to indicate that the Meulders 33 MeV measurement is about 40% too high, rather than the Saltmarsh 40 MeV measurement being too low. The lack of other literature data between 40 and 16 MeV motivates further measurements that we will report in this work. There is a slight disagreement between the

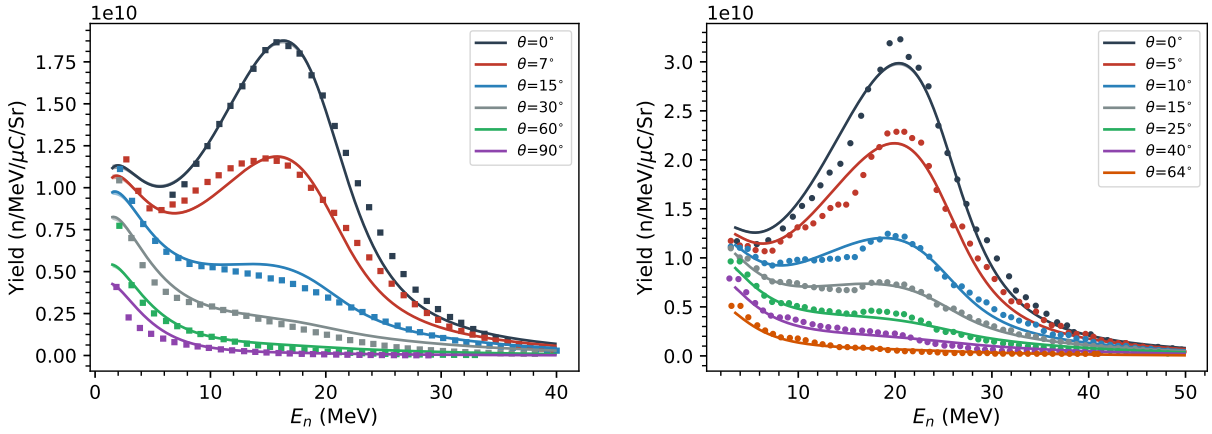

Figure 3.8: (left) Results of the fit to measurements by Saltmarsh (1977) at $\epsilon_d = 40$ MeV from $\theta = 0°$ to $\theta = 90°$. (right) Results of the fit to measurements by Meulders (1975) at $\epsilon_d = 50$ MeV from $\theta = 0°$ to $\theta = 64°$.

suggested width of the breakup peak in the 40 MeV data by Saltmarsh, which seems to show a wider peak, and in the 50 MeV Meulders data, which has a narrower peak. Because this method neglects direct reactions, there is also an underprediction of the 16 MeV Harrig dataset. However this is anticipated as being outside the scope of isotope production applications. There is also a subtle disagreement in the low energy compound spectrum, which is likely due to issues in determining the time-of-flight detection efficiency at low energies.

Model Validation

The collected data that was not used for fitting the breakup model was instead used in a validation procedure, to estimate how well the model extrapolated to other materials and deuteron energies. The results of this validation can be seen in figure 3.9. Because of the previously mentioned discrepancies, the Schweimer data were multiplied by a factor of 1.4, in order to match Saltmarsh at 40 MeV, and the Weaver data were multiplied by 0.8, in order to match the Harrig data at 16 MeV.

The results of this validation are encouraging. The fit on beryllium extrapolated to the corrected 54 MeV Schweimer dataset shows good agreement, which builds confidence in the ability of this model to extrapolate to higher energies, as that may be useful for isotope production purposes. The modeled values on lithium and carbon are systematically high, however this seems mostly attributable to the compound component of the cross sections, rather than the breakup part. This is quite evident in these spectra at low energies, and at large angles. This should not be too surprising, as the compound (and pre-equilibrium)

contributions to the spectrum were specifically chosen to match beryllium data, rather than being based on a more broadly applicable theory.

Interestingly, the breakup model extrapolates well to copper ($Z = 29$), which should have a significant elastic breakup component, despite the fact that the model does not account for this. However the model largely fails to reproduce the double-differential data from Weaver, except at large angle where we can assume most of the neutrons are from compound reactions. This is likely due to the absence of direct reaction modeling.

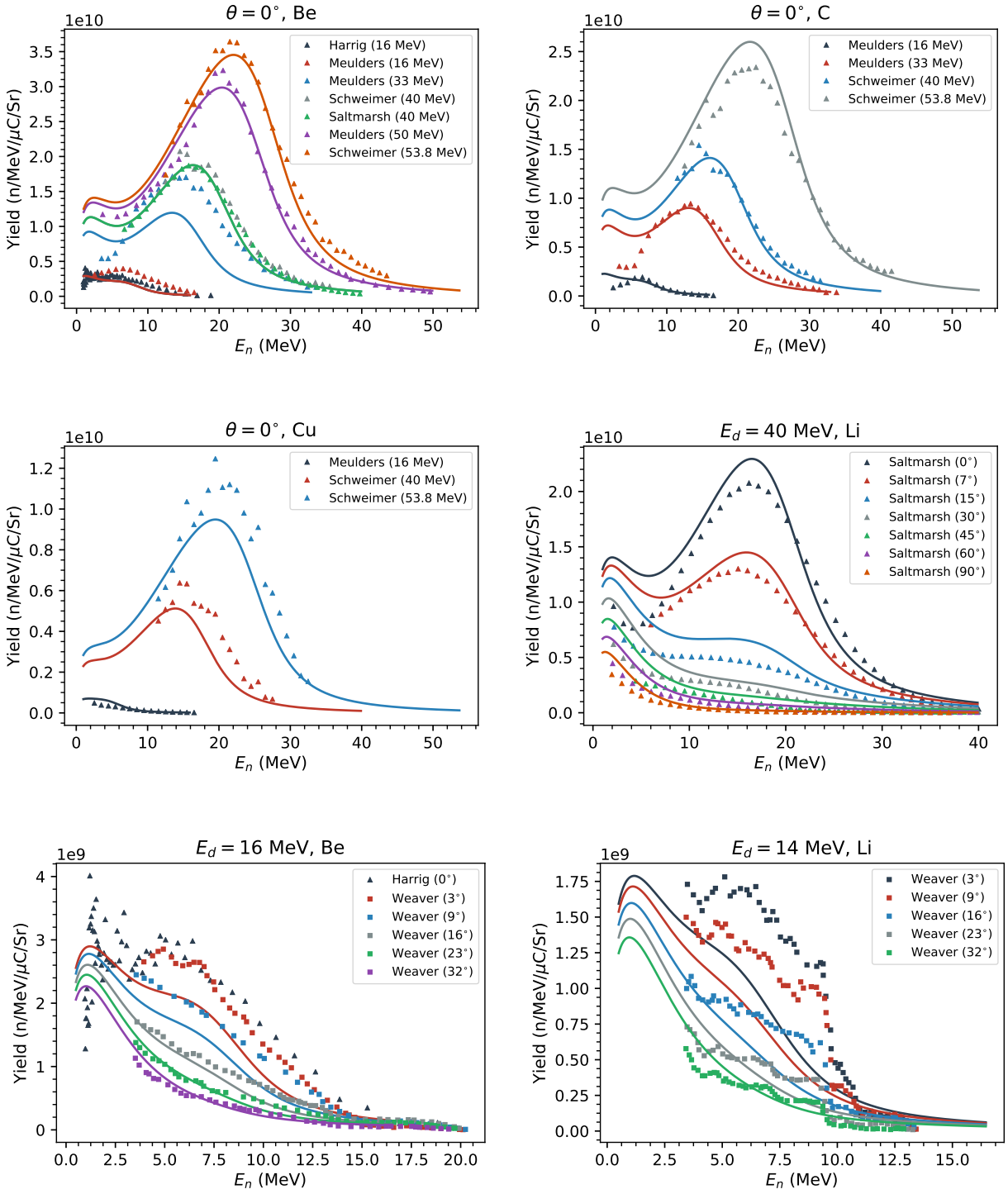

Figure 3.9: Comparison of modeled neutron yields to literature measurements. The first three plots show $\theta = 0°$ measurements on Be, C and Cu. The following three plots show measurements at multiple angles, on Li and Be.

3.3 Measurements of Neutron Yields from Deuteron Breakup on a Thick Beryllium Target

As described in the previous section, there are a number of discrepancies between existing literature measurements that motivate further experimental clarification. In this work, we present the results of two separate irradiations to measure the neutron yields from thick target deuteron breakup on beryllium. Because the discrepancy surrounds the magnitudes of the 33 MeV Meulders dataset and the 40 MeV work of Saltmarsh, these were the two deuteron energies selected for these irradiations.

This is also an energy range that has a relatively high importance for isotope production applications. In chapter 4 we will consider the use of neutrons from deuteron breakup for the production of ^{225}Ac via the ^{226}Ra(n,2n) reaction pathway. At 33 MeV, the neutron spectrum overlaps well with the predicted cross sections. However at 40 MeV, the neutron yields will be higher, and depending on the shape of the ^{226}Ra(n,2n) reaction, may consequently produce higher yields of the valuable medical radionuclide ^{225}Ac.

The first irradiation at 33 MeV consisted only of a foil activation experiment, in which the fitting procedure employed in equation 3.2 was used to extract the observed spectrum from the foil data. At 40 MeV, this was repeated, in addition to a time-of-flight measurement. Each of these experiments consisted of measurements at multiple angles, such that the angular dependence of breakup, as well as the relative contributions from compound reactions and pre-equilibrium, could be understood. In the foil activation experiments, zinc and titanium foils were also co-irradiated to quantify the production of certain medically relevant radionuclides.

Facility Overview

Both irradiations were performed at the Lawrence Berkeley National Laboratory's 88-Inch Cyclotron [61]. The 88-Inch Cyclotron is a variable-beam, variable-energy K=140 isochronous cyclotron, capable of producing deuteron beams with energies up to 55 MeV. The cyclotron facility has a number of shielded experimental "caves", for various applications (see figure 2.2 in chapter 2). Both the 33 and 40 MeV irradiations were performed in Cave 0, considered the "high level" cave due to the extensive radiation shielding enclosing it. Critically for the time-of-flight experiment, this cave is well isolated from neutrons produced by deuteron scraping that might occur in the cyclotron vault, which would interfere with the time-of-flight signals.

One important consideration for the location was in the positioning of detectors for the time-of-flight experiment. Due to the size of the cave, the EJ-309 neutron scintillators [123] were placed between 1.2–2.3 m from the breakup target, ranging from 0–90°. While these path-lengths may be somewhat short, they still proved acceptable based on the energies

being measured, the temporal resolution of the electronics, and the wraparound time of the machine.

Following irradiation, the neutron monitor foils were transferred to a separate counting room within the cyclotron laboratory. These foils were counted on the same ORTEC GMX Series (model GMX-50220-S) High-Purity Germanium (HPGe) detector that was previously used for the La(p,x) experiment described in chapter 2. For these irradiations, the detector energy and efficiency calibrations were determined with the use of the following NIST traceable standard calibration sources: ^{152}Eu, ^{133}Ba, ^{137}Cs, ^{60}Co and ^{57}Co.

Activation Analysis

Neutron activation analysis is a standard technique in which the neutron flux incident upon a foil may be determined from the activity induced upon it and the reaction cross section for the formation of that activation product using the well known thin-target activation equation

$$R = n\langle\sigma\rangle\langle\phi\rangle \tag{3.3}$$

where n is the number of target atoms, R is the production rate, determined by the measured product activity, $\langle\sigma\rangle$ is the flux-averaged cross section given by

$$\langle\sigma\rangle = \frac{\left(\int_{E_n}\sigma(E_n)\phi(E_n)dE_n\right)}{\langle\phi\rangle} \tag{3.4}$$

and $\langle\phi\rangle = \int_{E_n}\phi(E_n)dE_n$ is the scalar neutron flux. Generally in order to solve this for the scalar flux $\langle\phi\rangle$, the relative shape of the flux must be known. However for the purpose of this study, it is the shape of this flux that we are trying to determine. In order to resolve this dilemma, we will measure multiple reaction channels in the neutron monitor foils, which each have different thresholds and are sensitive to different energy regions. In this way, we can essentially find the scalar flux in a small energy window, and then use this to determine the overall shape in an iterative manner.

Figure 3.10 demonstrates this with some of the monitor reactions that were used in this study. It is clear that, for example, ^{115}In(n,n')^{115m}In and ^{89}Y(n,3n)^{87}Y have very little overlap, and are sensitive to neutrons in the 1–10 and 25–35 MeV energy ranges, respectively. Therefore the relative activation rates of the two channels should provide the relative magnitude of the flux in each energy region, and consequently some idea about the flux shape.

If we insert our parameterized breakup model into the above activation equation, the predicted production rate is given by

$$R_{pred,i}(\theta) = \frac{n\cdot I_d}{A}\int_{\hat{\Omega}}\int_{E_n=0}^{E_d}\sigma(E_n)\frac{d^2Y(E_n,\theta)}{d\Omega dE_n}dE_n d\Omega$$

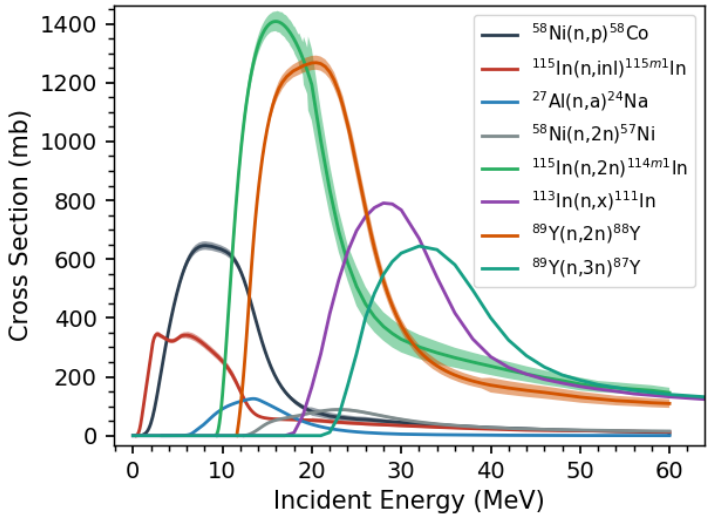

Figure 3.10: Evaluated cross sections for some of the monitor reactions used in the foil activation experiment.

where I_d is the deuteron beam current (in units of µA), A is the area of our monitor foil, and the double differential neutron yield $\frac{d^2Y(E_n,\theta)}{d\Omega dE_n}$ calculated using the hybrid Serber model can be adjusted to match the measured production rates by varying the parameters $(c_1, \ldots, c_6)$ in equation 3.2. In addition to using multiple monitor foils, we can measure these production rates at multiple angles to improve the fit of the terms in eq. 3.2 related to the breakup angular distribution, as well as the compound and the pre-equilibrium contributions to the spectrum, as these will be more sensitive at larger angles.

By comparing the predicted production rates for each of the i reaction channels to those we measure through activation, $R_{meas,i}$, the optimum parameters c_i can be fit by minimizing

$$\chi^2 = \sum_i \frac{(R_{meas,i} - R_{pred,i})^2}{\sigma^2_{meas,i}}$$

This will yield the spectrum, in terms of the hybrid Serber model, which best reproduces the experimental reaction rates.

In order to produce the best results using this method, multiple activation foils were chosen that had well-characterized cross sections; either reactions that were evaluated in the IRDFF-II library [124] or where the TENDL-2015 evaluation gave good agreement with data from EXFOR [125]. For the 33 MeV irradiation, nickel, indium, zirconium and aluminum monitor foils were used. At 40 MeV, an yttrium foils was also included in the foil packets. Additionally, titanium foils were included in the 40 MeV irradiation, and zinc foils were included in both, in order to measure production cross sections for select emerging radionu-

Reaction	Library
^{27}Al(n,x)^{24}Na	IRDFF-II
^{nat}Ni(n,x)^{58}Co	IRDFF-II
^{nat}Ni(n,x)^{57}Ni	IRDFF-II
^{58}Ni(n,x)^{57}Co	TENDL-2015
^{89}Y(n,2n)^{88}Y	IRDFF-II
^{89}Y(n,3n)^{87g}Y	TENDL-2015
^{89}Y(n,3n)^{89m}Y	TENDL-2015
^{nat}Zr(n,x)^{89}Zr	IRDFF-II
^{113}In(n,3n)^{111}In	TENDL-2015
^{115}In(n,2n)^{114m1}In	IRDFF-II
^{115}In(n,n')^{115m}In	IRDFF-II

Table 3.3: Neutron monitor reactions used for the foil activation spectral reconstruction. Note that the reactions based on ^{89}Y targets only applied to the 40 MeV irradiation. Cross section data was retrieved from IRDFF-II and TENDL-2015.

clides. The specific monitor reactions used and libraries from which the cross section data were retrieved are given in table 3.3.

All foils were purchased from Goodfellow Corporation (Coraopolis, Pa 15108, USA) and were of either 99 or 99.99% purity (metals basis) with natural isotopic abundances. All foils were cut to 1 cm diameter disks, and were cold rolled to 0.5 mm thickness, with the exception of the nickel foils which were cut to 6.3 mm diameter, of 1 mm thickness. Each foil was cleaned using isopropyl alcohol, and then its mass was measured using a milligram balance (after drying). One of each foil was then placed into a "foil packet", which was sealed using thin pieces of Kapton polyimide tape. Kapton with an acrylic based adhesive was specifically chosen to avoid contaminating ^{28}Si(n,x)^{24}Na reactions from silicone based adhesives, which may have interfered with the ^{27}Al(n,α) monitor channel [57], although the extent to which this poses a problem for neutron activation is likely minimal.

A custom foil holder was designed and 3D-printed for the purpose of these measurements, with pre-arranged slots for the monitor foil packets at 9 different angles (see figure 3.11).

The beryllium breakup targets were also loaded inside of the holder, with thin aluminum sheets behind the beryllium to prevent activation from any secondary protons produced in (d,p) breakup reactions. This entire assembly was placed in the TEN target box, which is held under vacuum at the end of the Cave 0 beamline. At 40 MeV, a slightly larger foil holder was printed to accommodate the additional 2 mm of beryllium required to stop the deuteron beam, which marginally changed the average angles of each foil packet.

The 33 MeV irradiation was performed with a beam current of 125 nA for 1 hour and

Figure 3.11: Photo of the foil holder used in the activation experiments. The plastic holder was loaded directly inside of the beam-pipe. Foils were wrapped in Kapton polyimide tape for encapsulation during handling. Thin aluminum foils were placed just behind the breakup target to prevent secondary protons from activating the samples.

20 minutes, whereas the 40 MeV irradiation was performed at 75 nA for 1 hour. Following irradiation, the foil packets were quickly removed from the beamline and transferred to the previously described HPGe counting lab.

Due to the large number of foils to be counted on a single detector, and the short half-lives involved with some of the monitor reaction channels, it was decided to count the foils together in packets, rather than individually, although individual counts were performed later in time. An example γ-ray spectrum from the 40 MeV foil packet at 31° can be seen in figure 3.12, as well as fits to the observed peaks.

Counting the foils in packets meant that there was a need to correct for the photon attenuation caused by the additional foils between a particular sample and the detector. If

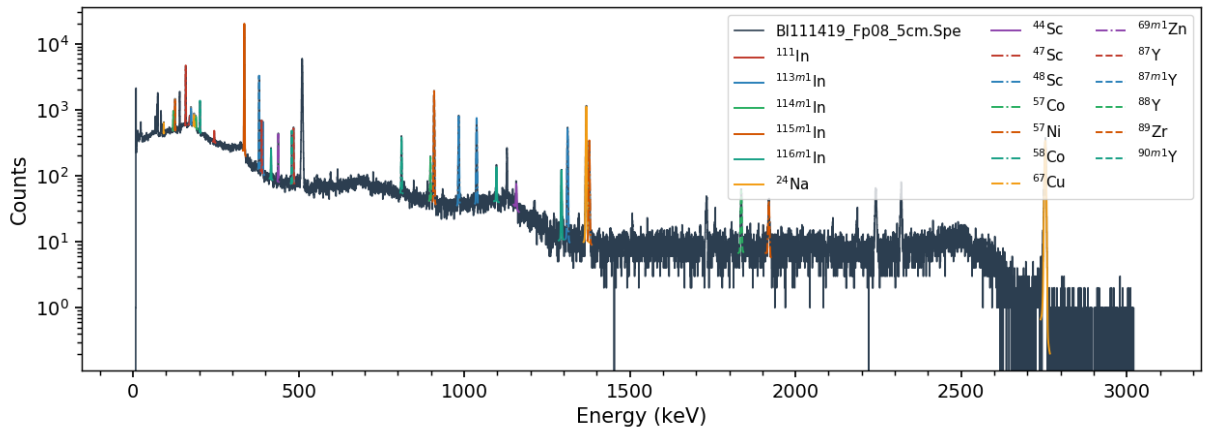

Figure 3.12: Example γ-ray spectrum from the 40 MeV activation experiment.

a given activity A_{meas} was measured at time t, the attenuation corrected activity $A(t)$ is determined by the equation

$$A(t) = A_{meas}(t)\left(\frac{1 - e^{-\mu_0 \cdot x_0}}{\mu_0 \cdot x_0} \cdot \sum_{i=1}^{N} e^{-\mu_i \cdot x_i}\right)^{-1}$$

where the various μ_i's are photon attenuation coefficients [126], the $1 - \exp(-\mu_0 \cdot x_0)$ factor accounts for the attenuation within the radiogenic sample itself, and the other N $\exp(-\mu_i \cdot x_i)$ terms correct for the attenuation in the other samples between it and the detector.

The Bateman equations [65], as implemented in the Curie code [127], were used to determine the measured production rates $R_{meas,i}$ in each monitor reaction channel from these (corrected) activities, which were measured at multiple time points after the end-of-bombardment (EoB). These measured production rates were then used to iteratively solve for the flux distribution from breakup, as previously described.

Time of Flight

For the 40 MeV measurement, neutron time-of-flight (nToF) spectroscopy was performed in addition to the activation experiment. The advantage of this method is that the neutron energy can be directly measured by the detector, in a relatively straightforward manner. The challenges with nToF surround the determination of the detection efficiency. Because activation was also performed, this can be used to normalize the nToF spectra, such that only the relative detection efficiency in each detector needs to be determined.

In this experiment, 5 EJ-309 liquid scintillation detectors were placed at angles ranging from 0–90°, which were located 1.2–2.3 m from the deuteron breakup target, with the 90° detector being placed the closest. A photo of the 0° and 18.2° detectors can be seen in figure 3.13. The digital data acquisition system used to measure the neutron spectra from the detectors was a Mesytec MDPP-16, running the QDC (charge sensitive) firmware and the MVME recording software [128]. The cyclotron RF clock frequency was also routed into one of the MDPP-16 inputs, to act as a start gate for the counting window totaling about 98 ns. With this firmware, the MDPP-16 integrates the entire charge in each detected pulse, as well as the charge in a "short" gate pulse, which together can be used to perform pulse-shape discrimination (PSD) to differentiate neutron and photon signals in the detector.

Figure 3.13: Photo of the EJ-309 neutron scintillation detectors used in the time-of-flight experiment. Pictured here are the detectors positioned at 0° and 18.2°.

The breakup target that was developed for the actinium production experiment described in chapter 4 was used for the nToF measurements. Further details about the beamstop dimensions and construction can be found in appendix A. The beamstop holding the beryllium breakup target in place was made from thick aluminum, which meant that an attenuation correction needed to be applied in the interpretation of the results.

Due to the relatively high neutron output from 40 MeV deuteron breakup, the nToF irradiation was performed at a beam current of 0.7 nA for approximately 30 minutes, which was enough to achieve good statistics. Figure 3.14 shows the nToF spectrum from the 0°

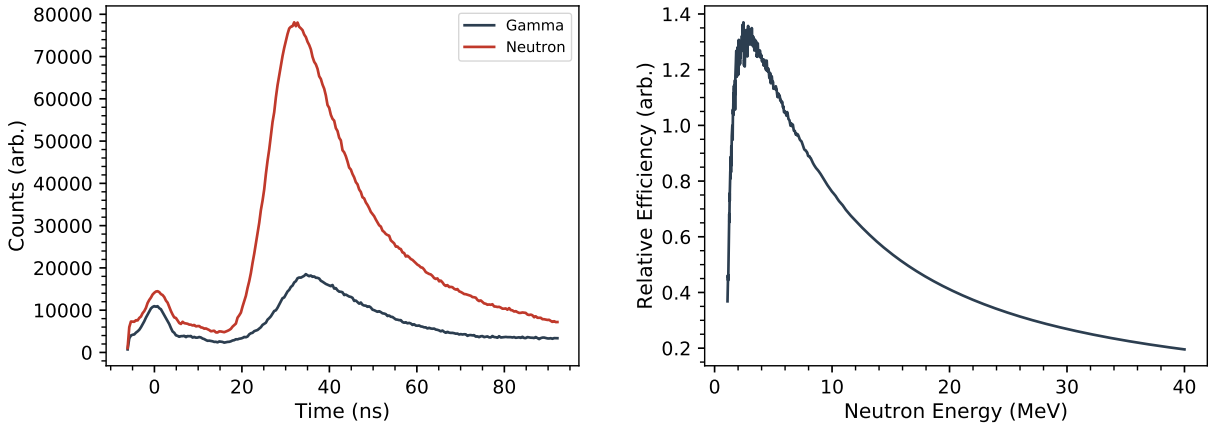

Figure 3.14: (left) Time-of-flight spectrum from the detector at 0°, with characteristic γ peak at t_0, followed by the neutron signal. Some overlap can be seen in both signals, due to imperfect pulse-shape discrimination. (right) Detector efficiency for $E_{cut} = 1$ MeV. The proton cutoff energy E_{cut} was determined for each detector separately, but was typically 1–2 MeV.

detector, with more than 10,000 counts in every time bin of the neutron channel.

The time-of-flight spectrum of the neutrons was determined using cuts on the integrated tail/total PSD parameter. This was done to select only events corresponding to H(n,elastic) interactions in the scintillator, as the C(n,α) contribution to the spectrum was clearly visible, although easily separable. There as also a low-energy cut, to eliminate the portion of the energy spectrum with poor PSD. The time-of-flight spectrum was then converted into an energy spectrum using the relativistic time-of-flight equations

$$E_n(t) = (m_n c^2)(\gamma - 1) = (m_n c^2)\left(\frac{1}{\sqrt{1 - \left(\frac{1}{c} d/(t + \Delta t_\gamma)\right)^2}} - 1\right)$$

where $m_n c^2$ is the neutron rest mass energy, t is the time of flight, and $\Delta t_\gamma = d/c$ is the time required for a photon to traverse the same distance as a neutron. This adjustment is required because the time of flight is determined relative to the characteristic "gamma flash" that occurs when the cyclotron beam pulse first strikes the target.

In order to properly determine the neutron yields at each angle position, the detection efficiency as a function of neutron energy must be determined. Because we are normalizing the nToF results with the activation measurements, we are only concerned with the relative detection efficiency. EJ-309 detectors are composed of a scintillating fluid that is chemically similar to xylene: $(CH_3)_2C_6H_4$ [129]. At the energies measured in this experiment, neutrons primarily generate light in the detector through elastic scattering of hydrogen, or through

C(n,α) reactions. Because the (n,α) contribution can be separated from our spectrum with PSD, we can attribute all of the neutron signal to (n,elastic) reactions. There is a lower limit, E_{cut}, below which the recoil proton will not be detected. In this case, the value of E_{cut} was set by the energy below which the PSD became poor. If we make the assumption of a small detector volume relative to the neutron path length (i.e. no multiple scattering), the detection efficiency will be proportional to

$$\epsilon(E_n) \propto \sigma_{el}(E_n) \cdot \frac{E_n - E_{cut}}{E_n}$$

where σ_{el} is the H(n,elastic) cross section and the factor $(E_n - E_{cut})/E_n$ arises from the fact that the neutron elastic scattering kernel for protons is uniform in energy, or more simply that the incident neutron has an equal probability of scattering to any proton energy. A plot of the detection efficiency for an example of $E_{cut} = 1$ MeV is shown in figure 3.14.

One issue that tends to arise with this determination of the detection efficiency is that in the low-energy portion of the spectrum, the efficiency is asymptotically dependent on the value of E_{cut}. Thus the uncertainty in E_{cut} gets propagated into a very large systematic uncertainty in the efficiency. To account for this, the reported spectra will not include data within 0.2 MeV of E_{cut}.

3.4 Experimental Results

The measured deuteron breakup spectra showed relatively good agreement with the predictions of the hybrid Serber model, which were based on a fit to literature data on beryllium. The discrepancy between the Meulders 33 MeV measurement and the Saltmarsh 40 MeV measurement was confirmed, with the values observed in this experiment being very close to the measurements by Saltmarsh. These also represent the first set of measurements of 33 MeV deuteron breakup taken at multiple angles, which will be a valuable tool for the optimization of isotope production pathways which make use of thick target deuteron breakup as a neutron source.

Activation Spectral Reconstruction

The results of the foil activation experiments can be seen in figure 3.15. The data show a clear agreement with the Saltmarsh measurements, and the predictions of the hybrid Serber model, and also show that the Meulders 33 MeV measurement was systematically high. However, the measured values are approximately 12% higher than the predictions of the hybrid model. At forward angles for 33 MeV deuterons, this is likely attributable to an underprediction of the total deuteron breakup cross section, albeit only slightly.

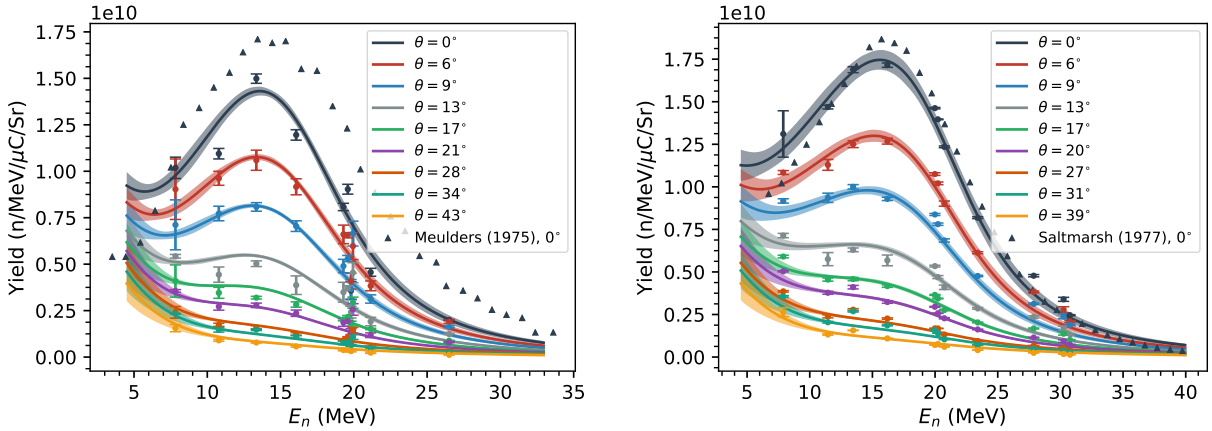

Figure 3.15: Results of the activation measurements at $\epsilon_d = 33$ MeV (left) and $\epsilon_d = 40$ MeV (right). The centroids of the experimental data points were are derived from the energy average of the cross section, i.e. $\frac{\langle E \cdot \sigma(E) \rangle}{\langle \sigma(E) \rangle}$. The solid line (and the 1-σ error band) indicates the Serber model fit to the data.

i	c_i(33 MeV)	c_i(40 MeV)
1	1.46	1.56
2	0.43	1.93
3	1.8	1.73
4	1.1	1.16
5	1.19	0.89
6	0.59	0.51

Table 3.4: Fitted parameters for the double-differential neutron production cross section, as described in Eq. 3.2, for the 33 and 40 MeV activation experiments.

These measurements were determined by fitting the predicted production rates, based on the model parameters $c_1, \ldots, 6$ in equation 3.2, to the measured production rates in each monitor reaction channel. The optimized values of c_i for each measurement are summarized in table 3.4.

There are a few clear similarities between the results of the two measurements. The angle and particularly the energy distributions for each were wider than the optimized hybrid model. There was also a clear decrease in the pre-equilibrium contribution to the spectrum. This could be a real, significant decrease, however because pre-equilibrium is already a relatively small contributor to the spectrum, it could also be a statistical anomaly due to the fitting method. And while the magnitude component of the total breakup cross section increased in both cases, the slope factor also changed by a factor of two in both cases

(although in opposite directions), so it is difficult to say whether or not this is significant. Most of these fitted parameters are probably not valid outside the scope of the data they were fitted to. However, the fact that the width of the energy distribution is significantly wider than the hybrid model prediction indicates that either the Meulders 50 MeV measured distributions are narrower than in reality, or that the model does predict these widths as a function of deuteron energy correctly.

Time of Flight Results

The measured nToF results are plotted in figure 3.16, along with a comparison to the 40 MeV activation results, the Saltmarsh data, and the optimized hybrid Serber model. While it is not surprising that the magnitudes of the nToF and activation results are similar, as one was used to normalize the other, the relatively good agreement in the shape of these results does build confidence in the activation results taken at 33 MeV. Interestingly, the increased width of the breakup neutron energy distribution, which was seen in the activation data, is also present in the nToF data. The breakup peak is fully apparent only in the 0° spectrum, however even in the small peak at 15° it is clear that the measured spectrum is wider than either the Saltmarsh values or the hybrid Serber model (which was itself fit to the Saltmarsh data).

One clear area of systematic disagreement between the nToF data and the foil activation data is in the low energy portion of the spectrum, where the activation measurements are generally higher. This could just be an artifact of normalization: if the high energy side is overpredicted then the low energy side will necessarily be underpredicted. It could also be an error in the nToF efficiency determination, as the low energy portion of the spectrum, close to E_{cut}, will be most sensitive to that. Or, it could be due to a lack of monitor reaction sensitivity in the low energy portion of the spectrum. Only ^{115}In(n,n')^{115m}In extends down to the lowest part of the spectrum, but has significant cross section up to 10 MeV. This could be improved with more (n,n') or (n,p) reactions in this energy region, with multiple different thresholds helping to improve the sensitivity.

Cross Section Measurements on ^{nat}Zn, ^{nat}Ti Targets

In addition to the monitor foils, natural foils of titanium and zinc were included in the foil packs irradiated during the activation experiments. The purpose of this was to measure the production of a number of medically significant radionuclides.

Theranostics (therapeutic-diagnostics) are a relatively new class of radiopharmaceutical, in which both therapeutic and diagnostic isotopes (usually) of the same element are given as part of a treatment [130]. Because the two isotopes are indistinguishable from a chemical per-

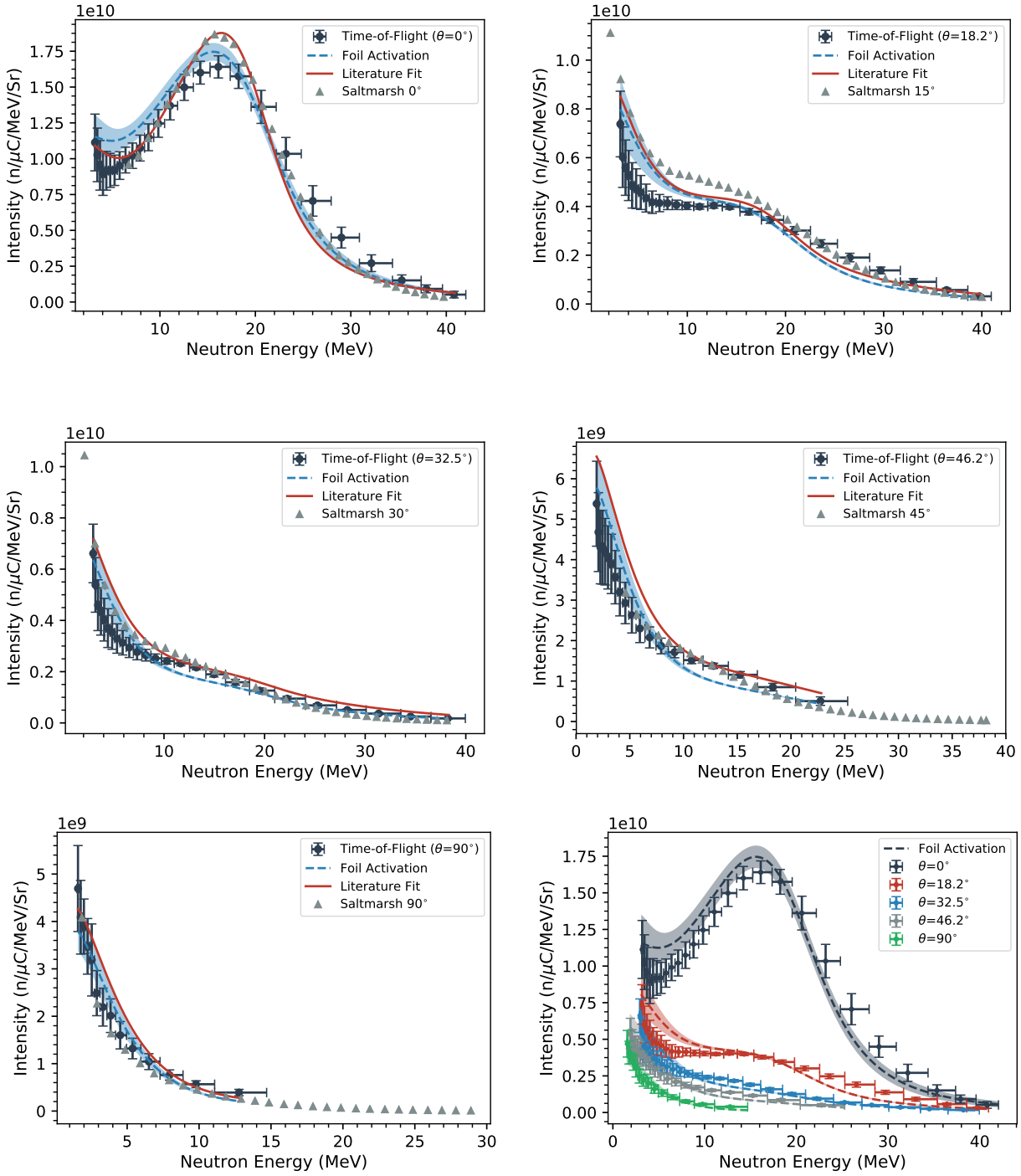

Figure 3.16: Measured time-of-flight spectra at $\epsilon_d = 40$ MeV. Measured angles were 0°, 18.2°, 32.5°, 46.2° and 90°. Each plot compares the measured results to the extracted yields from the 40 MeV foil activation experiment (to which these data are normalized), the Serber model, and the Saltmarsh data (occasionally differing by $< 3.2°$). A comparison between the spectra and activation data measured at all angles can be seen in the lower right.

Reaction	Multiplier
^{nat}Zn(n,x)^{67}Cu	0.81 ± 0.08
^{nat}Zn(n,x)^{64}Cu	0.96 ± 0.09
^{nat}Ti(n,x)^{47}Sc	0.65 ± 0.06
^{nat}Ti(n,x)^{44}Sc	0.083 ± 0.025
^{nat}Ti(n,x)^{46}Sc	0.84 ± 0.08
^{nat}Ti(n,x)^{48}Sc	0.7 ± 0.05
^{nat}Zn(n,x)^{65}Zn	0.43 ± 0.04
^{nat}Zn(n,x)^{63}Zn	0.33 ± 0.06

Table 3.5: Results of fit to measured cross sections.

spective, they will exhibit identical biochemistry. If one of the isotopes is a positron-emitter, enabling the use of the high resolution positron-emission tomography (PET) scanning technique, then an exact dose profile of the therapeutic isotope can be mapped through modeling of its decay processes with a similarly high resolution [29].

The theranostic pairs of interest for production from zinc and titanium targets are ^{64}Cu/^{67}Cu and ^{44}Sc/^{47}Sc, respectively. While both of the PET emitting isotopes ^{64}Cu and ^{44}Sc can be produced in relatively large abundances through ^{63}Cu(n,γ) and ^{44}Ca(p,n) (on an enriched target), the therapeutic β^- emitters ^{47}Sc and ^{67}Cu have much more challenging pathways. In chapter 5 we will compare (γ,p) and (n,np) pathways for the production of these isotopes.

In the activation experiments, the production of all four of these theranostic isotopes was observed, as well as a number of neighboring reaction channels. Unfortunately, the induced activities were measured with relatively poor statistics, mostly due to an overwhelming γ-ray background from some of the other, much stronger monitor reaction channels. However, the measured production rates were converted into cross sections using equation 4.1, with the model parameters for $\phi(E_n)$ from the activation experiment fits reported in table 3.4. These cross section values are plotted in figure 3.17, along with an x "errorbar" representing the $\pm 1\sigma$ energy distribution, rather than the uncertainty in the mean energy.

Because these cross sections are averaged over a wide spectrum, have rather large uncertainties, and are somewhat difficult to interpret, we will present the results of a very basic "fit" to these measurements. The fit is simply a constant multiplicative factor by which to scale the TENDL-2015 cross sections for each channel, such that they best reproduce the measured flux-averaged cross sections. This provides a good visualization of what the "actual" cross sections were in these measurements, and it will also have a lower error than the individual cross sections because it is an average over all of them. The optimized scaling parameters from this fit are given in table 3.5.

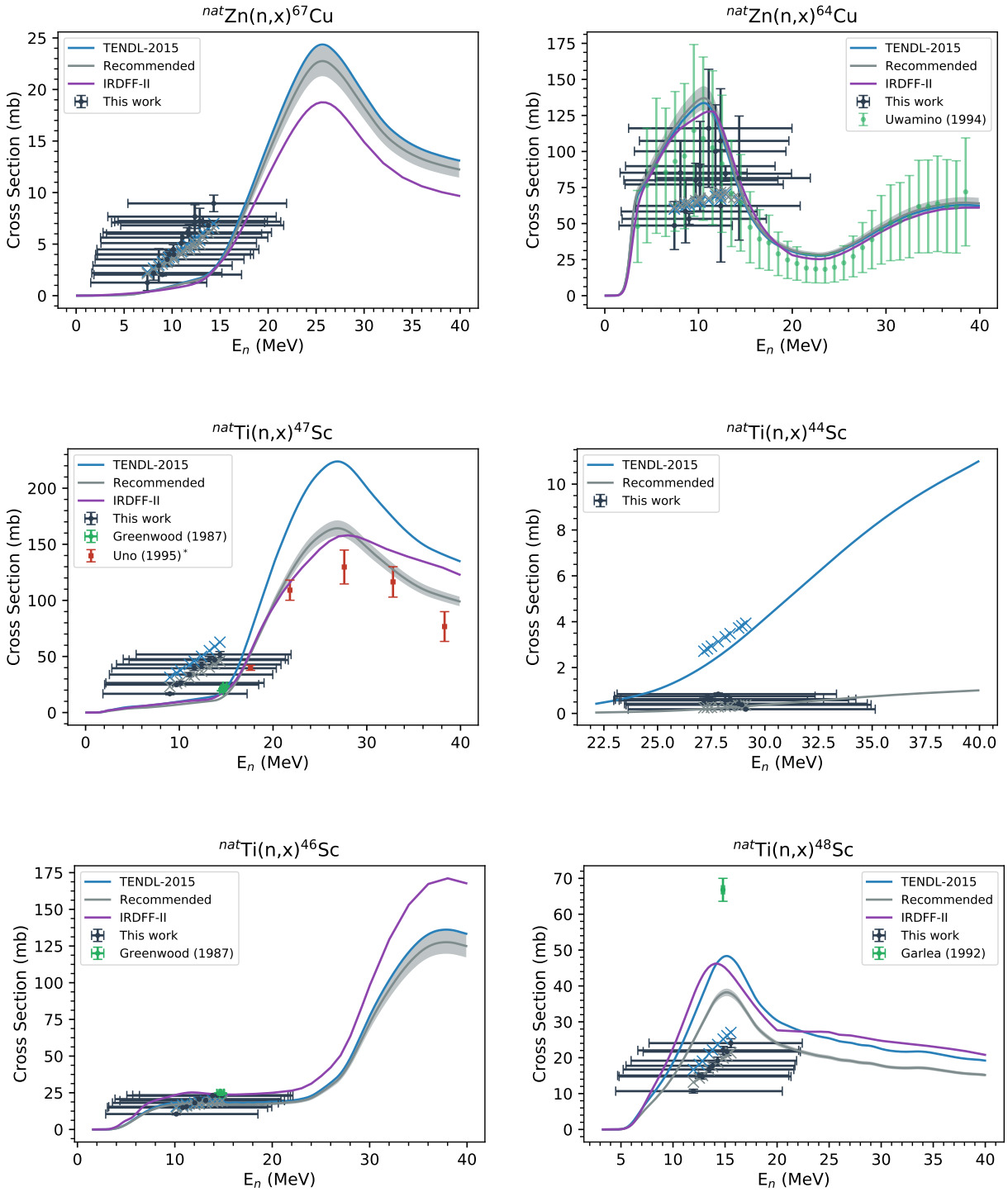

Figure 3.17: Cross sections measured via activation. The x-error bars indicate the $\pm 1\sigma$ widths of the neutron distributions. The grey line indicates a "recommended" cross section, based off a scaling of the TENDL data that best fits the measured values. Points marked with "$\times$" show flux-averaged values from each respective library, at each measured energy centroid.

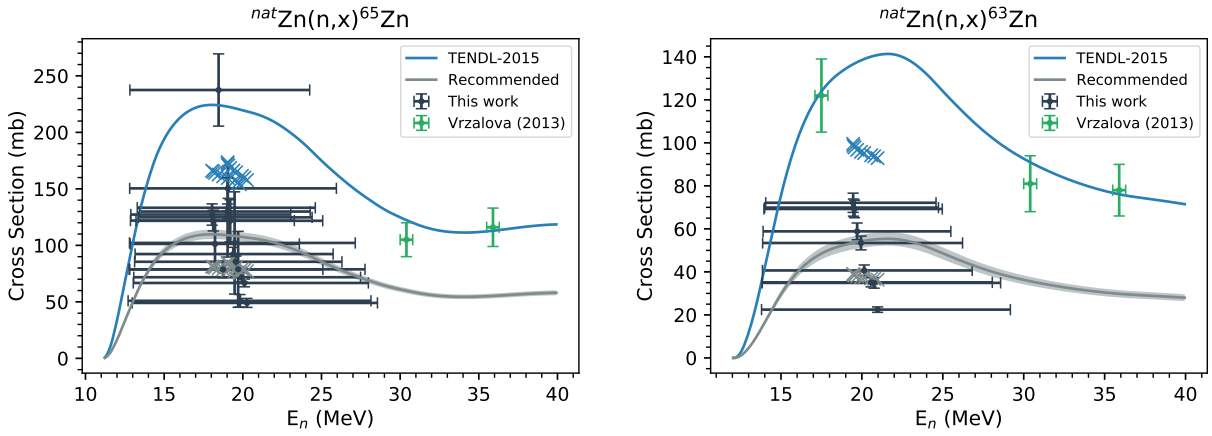

Figure 3.18: Measured cross sections. The x-error bars indicate the $\pm 1\sigma$ widths of the neutron distributions. The grey line indicates a "recommended" cross section, based off a scaling of the TENDL data that best fits the measured values. Points marked with "$\times$" show flux-averaged values from each respective library, at each measured energy centroid.

3.5 Summary and Conclusions

In this work we have proposed a new hybrid model for predicting neutron yields from intermediate-energy deuteron breakup on light targets. The model was benchmarked against literature values at a variety of incident deuteron energies and outgoing neutron energies and angles. This model has the benefits of a relatively simple calculation method, without sacrificing accuracy over the application range considered. It has also been adapted to apply a relatively simple 6-parameter fitting procedure, which was demonstrated to be applicable to both global fits across the literature values mentioned above, as well as a more focused fit to neutron monitor activation data for spectrum unfolding.

We have also presented new measurements of the breakup spectrum on beryllium for deuteron energies of 33 and 40 MeV. These were performed with neutron activation unfolding, using the hybrid breakup model to forward-fit to the spectrum, as well as a more conventional time-of-flight experiment, which was normalized to the activation data. The results of this showed that the hybrid model was generally accurate. Additionally, cross section measurements for a number of medically relevant isotope production pathways were presented, along with a recommended cross section based on these measurements.

It is the hope that this work, in providing a relatively simple yet accurate model of deutron breakup on light targets, will aid in the design of future high intensity neutron sources based on this mechanism, and will enable new research into applications such as isotope production.

Relevant Nuclear Data

Isotope	γ Energy (keV)	I_γ (%)	$T_{1/2}$
^{24}Na	1368.626	99.9936 (15)	3.16 (4) d
	2754.007	99.855 (5)	
^{44}Sc	1157.02	99.9 (4)	3.97 (4) h
^{46}Sc	889.277	99.984 (1)	83.79 (4) d
	1120.545	99.987 (1)	
^{47}Sc	159.381	68.3 (4)	3.3492 (6) d
^{48}Sc	175.361	7.48 (1)	43.67 (9) h
	983.526	100.1 (6)	
	1037.522	97.6 (7)	
	1212.88	2.38 (4)	
	1312.12	100.1 (7)	
^{57}Co	122.06065	85.6 (17)	271.74 (6) d
	136.47356	10.68 (8)	
^{57}Ni	127.164	16.7 (5)	36.60 (6) h
	1377.63	81.7 (4)	
	1919.52	12.3 (4)	
^{58}Co	810.7593	99.45 (1)	70.86 (6) d
^{63}Zn	669.62	8.2 (3)	38.47 (5) m
	962.06	6.5 (4)	
^{64}Cu	1345.77	0.475 (11)	12.701 (2) h
^{65}Zn	1115.539	50.04 (1)	243.93 (9) d
^{67}Cu	93.311	16.1 (2)	61.83 (12) h
	184.577	48.7 (3)	
^{87m}Y	380.79	78.05 (8)	13.37 (3) h
^{87}Y	388.5276	82.2 (11)	79.8 (3) h
	484.805	89.8(9)	
^{88}Y	898.042	93.7 (3)	106.626 (21) d
	1836.063	99.2 (3)	
^{89}Zr	909.15	99.04 (5)	78.41 (12) h
^{111}In	171.28	90.7 (9)	2.8047 (4) d
	245.35	94.1 (1)	
^{113m}In	391.698	64.94 (17)	99.476 (23) m
^{114m}In	190.27	15.56 (15)	49.51 (1) d
	558.43	4.4 (6)	
	725.24	4.4 (6)	
^{115m}In	336.241	45.9 (1)	4.486 (4) h

Table 3.6: Principle γ-ray data from ENSDF [87, 88, 90, 131–145].

Chapter 4

^{225}Ac Production via the ^{226}Ra(n,2n) Pathway using a Deuteron-Breakup Source

4.1 Introduction

TARGETED alpha therapy is a particularly favorable new method of cancer treatment, in which an α-emitting radionuclide is attached to a targeting molecule, such as a monoclonal antibody, that has a high affinity for binding to cancer cells. Due to the high linear energy transfer (LET) and short range of decaying α-particles, this new class of radiopharmaceutical has the capability to destroy cancer cells while sparing nearby healthy tissue.

The α-emitting isotope ^{225}Ac ($t_{1/2}$ = 9.920 (3) d) is a promising candidate for alpha therapy, but is not currently available in quantities sufficient for widespread clinical use [32]. In this chapter, we will present the results of measurements of the spectrum-averaged ^{226}Ra(n,2n)^{225}Ra reaction cross section, using neutrons from thick target deuteron breakup. The measurements were performed at two incident deuteron energies, 33 and 40 MeV, which approximately corresponded to average neutron energies of 15 and 17 MeV, respectively. This represents a new pathway for the production of ^{225}Ac, and we will compare the potential ^{225}Ac production rates using this pathway to the estimated demand. In addition, a chemical separation of the ^{226}Ra target and produced ^{225}Ac was performed, to explore the radiochemistry of this production route. Preliminary results for this separation are presented.

Medical Potential of ^{225}Ac

There are a number of characteristics of the isotope ^{225}Ac that make it appealing for use in targeted alpha therapy (TAT). Most importantly, it has a half-life of 9.920 (3) days, which is in the optimal range for medical radionuclides. This is long enough such that it can be produced and isolated in a central facility, distributed, and used in treatments without decaying too significantly. However it is not too long, such that it might remain in the body for many years and do long-term damage. Furthermore, there are also no long-lived decay products of ^{225}Ac, that could present a similar issue [22, 24, 49, 50]. Actinium is also advantageous from a bio-chemical perspective, in that there is established chemistry to conjugate it to cancer targeting vectors, such as a monoclonal antibody, with widely available chelators such as DOTA [146]. However research on this subject is still ongoing, to improve the *in vivo* stability of such chelators [147].

Because ^{225}Ac can be bound to a targeting vector with a high affinity for cancer cells, such as PSMA-617 [148], it has shown promising results from a series of preliminary clinical trials in patients with metastatic castration resistant prostate cancer (mCRPC) [4]. Another attractive feature of ^{225}Ac is that it is a generator isotope for the ^{213}Bi alpha emitter, which has also shown clinical potential to improve patient outcomes [9].

However the ^{225}Ac used in these trials was derived from a ^{229}Th "cow", which slowly produced ^{225}Ac from natural decay at a rate of less than 13 µCi per mg of ^{229}Th, per day. While this source provides a steady supply of high purity ^{225}Ac, it does not supply enough to provide ^{225}Ac for widespread clinical use. It is estimated that approximately 800 µCi of ^{225}Ac is required to treat a patient with mCRPC, and the number of such cancer patients is in the hundreds of thousands per year, worldwide [35]. This means the requirements for the global, yearly production rate of ^{225}Ac is in the hundreds of curies. The current estimated supply of ^{225}Ac from ^{229}Th generators is about 2 Ci per year, which is not adequate to meet this demand [32].

Alternative Production Pathways

The leading production pathway for large scale ^{225}Ac production is with high energy protons on ^{232}Th targets. The ^{232}Th(p,x)^{225}Ac cross section is not very large, approximately 15 mb at 200 MeV [36]. However, the long range characteristic of high energy protons means that yields from this production route are quite high, and that this is a viable pathway to make Curie levels of ^{225}Ac. The drawback to this approach is that it is not possible to make pure ^{225}Ac, free of the contaminant ^{227}Ac with its 22 year half life. This contaminant has the potential to cause long term side-effects, and as a long-lived activation product is a nuclear waste concern.

Irradiating radium targets directly with protons, to produce ^{225}Ac from the ^{226}Ra(p,2n) reaction is also a potential pathway, and has the advantages of high yields and also high radio-purity [39]. However the challenges associated with directly irradiating a radium target, which is highly radioactive and chemically hazardous, likely preclude this production route from being pursued at a large scale.

The pathway proposed in this work is the ^{226}Ra(n,2n) reaction, which creates ^{225}Ra, the 15 day precursor to ^{225}Ac. This pathway has a high reaction cross section, estimated by TENDL at over two barns, and can be made completely free of ^{227}Ac. It also avoids some of the challenges of the ^{226}Ra(p,2n) route, as the high energy neutrons needed for the (n,2n) reaction will not deposit a significant amount of heat in the radium target.

The main challenge associated with this pathway is selecting a source of high energy neutrons comparable in intensity to large proton accelerators, that are commonly used for isotope production work. Two conventional sources of high energy neutrons, that may be considered, are deuterium-tritium (DT) neutron generators and fast reactors. Unfortunately, while the DT neutron generator spectrum is ideal for ^{226}Ra(n,2n), they do not have the intensities required for this route to be competitive with other pathways. Conversely, fast reactors have very high neutron intensities, but at too low an energy to be useful for this reaction.

Instead, thick target deuteron breakup is a source of high energy neutrons, and can be scaled up to the intensities required for isotope production. Deuteron breakup is a process whereby a high energy deuteron beam reacts with a target nucleus to overcome its modest 2.2 MeV binding energy, and break into its constituent proton and neutron. In a thick target, the outgoing protons will be stopped by Coulomb forces, however the uncharged neutron will continue on with approximately half the incident deuteron energy. The probability of a breakup reaction is quite high: a 40 MeV deuteron incident upon a thick beryllium target will produce a neutron almost 10% of the time. Because deuteron breakup is so intense, and the outgoing energy distribution is tunable (as it is approximately half the incident energy), it is a great candidate neutron source for producing ^{225}Ac via the ^{226}Ra(n,2n) pathway.

What is needed to optimize this pathway is a fundamental understanding of the outgoing neutron spectra, as a function of energy and angle, as well as an accurate assessment of the ^{226}Ra(n,2n) cross section. Chapter 3 provides an adjusted model, and a series of new measurements, for the neutron spectra from thick target deuteron breakup. In this chapter, we will perform measurements of the ^{226}Ra(n,2n) cross section, with a deuteron breakup neutron source.

Existing Data

There is a single literature measurement of this cross section, performed by O'Connor *et al.* in 1960, using a DT neutron generator [149]. The measured value was 1600 ± 300 mb, at a neutron energy of 14.5 MeV. Because the total neutron yield for thick target deuteron breakup increases with increasing deuteron energy, a measurement of the cross section at a higher energy would be useful in order to better predict ^{225}Ac yields for this pathway. It would also be good to have another measurement at an energy close to 15 MeV, to validate the existing O'Connor data point. To accomplish this, we used deuteron energies of 33 and 40 MeV to measure these cross sections, corresponding to average neutron energies of approximately 15 and 17 MeV, respectively.

As further motivation for new data, there is a rather significant discrepancy between the ENDF evaluation, TENDL and the O'Connor data point [125, 150]. At 14.5 MeV, TENDL-2015 recommends a cross section of 1440 mb, whereas in ENDF/B-VII.1 the value is only 546 mb. This comparison is plotted below in figure 4.5. While the O'Connor data point is much more consistent with the TENDL evaluation, further measurements would be valuable in resolving this discrepancy.

4.2 Methods

For this measurement, we used the neutron activation technique, in which the reaction cross section can be determined by quantifying the induced activity of the ^{225}Ra reaction product. To calculate a cross section with this method, we must accurately know the mass of the sample, as well as the neutron flux incident upon it. The neutron source used in this measurement was thick target deuteron breakup.

The main challenge that must be overcome in order to measure the induced ^{225}Ra activity is that the ^{226}Ra target is highly radioactive, creating a large background over which we must be able to observe the ^{225}Ra activity. The high radioactivity also prohibits the use of a large target mass. For ^{226}Ra specifically, every gram of material has an activity of exactly one Ci. In fact, this is the measure used to define the unit of a Curie.

In order to measure the ^{225}Ra production rate with sufficient accuracy, the ^{226}Ra target was bombarded with as high a neutron fluence as possible. This fluence was quantified using neutron monitor foils, which were assayed by γ spectroscopy. However, the ^{225}Ra could not be assayed by γ spectroscopy because of the intense γ-ray background from ^{226}Ra, and its decay products. Instead α spectroscopy was performed to assay the ^{221}Fr, ^{217}At and ^{213}Po decay products of ^{225}Ra, which emit higher energy alpha particles than ^{226}Ra or its decay products, enabling them to be distinguished despite their lower decay rate.

Experiment Setup

This experiment took place at the 88-Inch cyclotron, located at Lawrence Berkeley National Laboratory (LBNL) in Berkeley, California [61]. Two separate irradiations were performed, the first using a deuteron beam with an incident energy of 33 MeV, with the second taking place at 40 MeV. The 88-Inch cylotron is a variable-beam, variable-energy K=140 isochronous cyclotron, which is capable of producing deuteron beams of up to 20 µA in beam current. The cyclotron facility has several isolated beamlines, which are directed into a multitude of experimental "caves", which are surrounded by thick concrete radiation shielding (see figure 2.2). Both irradiations took place in Cave 0, which is considered the "high-level" cave, because it is a generally well shielded location. Nevertheless, the beam current utilized in this experiment had to be limited to below 5 µA, due to the intense radiation fields generated by the breakup source.

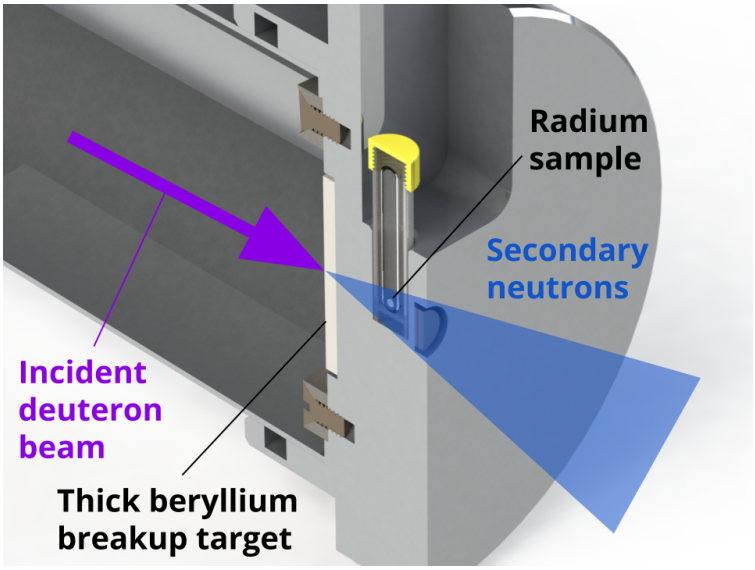

Figure 4.1: Rendering of the neutron production target used in the experiments, showing placement of the 1 mg radium sample and monitor foils.

Each irradiation was performed with a $Ra(NO_3)_2$ salt target, containing 1 mg of ^{226}Ra each. These samples also contained approximately 25 µCi of a ^{228}Ra impurity, or 91 ng, which is less than 0.01% of the total mass. These radium samples were acquired from Oak Ridge National Laboratory, where they were dried down into small grains of $Ra(NO_3)_2$ salt, and flame-sealed into 5 mm diameter quartz ampules to prevent ^{222}Rn contamination. This ampule was then placed inside of a secondary plastic capsule, for safe handling.

The neutron fluence was monitored using a 1 mm, 99.999% purity nickel foil and a 0.5 mm, 99% purity yttrium foil, both purchased from Goodfellow Corporation (Coraopolis, PA

15108, USA). Both foils were cut to 1 cm diameter disks, and their masses were measured with a milligram balance. Prior to irradiation they were cleaned with isopropyl alcohol and sealed in 3M 5413-Series Kapton polyimide film tape.

A new beamstop was designed and fabricated to accommodate the unique requirements of this measurement. A cut-away rendering of the new beamstop can be seen in figure 4.1, with key components highlighted. This beamstop was designed to keep the radium target as close as possible to the breakup source, but also outside of the vacuum beamline. For this design, the radium was about 1.9 cm from the beryllium breakup target. To ensure adequate cooling for this high-current irradiation, the target is securely clamped inside of the beamstop, and a water cooling plate (not pictured) was also clamped to the back. Immediately behind the slot for the radium capsule is a machined recess for placement of the neutron monitor foils. The geometry for the two irradiations was identical, with the exception that only 4 mm of beryllium was used for the breakup target in the 33 MeV irradiation, whereas 6 mm was used at 40 MeV.

The entire beamstop was made with 6061-aluminum, for ease of fabrication and to minimize the production of any long-lived activities that would impede safe handling after the irradiation. More details on the design and fabrication of the beamstop can be found in appendix A.

Irradiation

As previously stated, the goal for the irradiation was to maximize the total neutron fluence on the radium targets. This was accomplished by irradiating the samples with as much beam current as possible, for as much time as possible, and by minimizing the beamspot size. The beam current was limited to under 5 µA to maintain radiation safety in the work areas surrounding Cave 0. For the 33 MeV irradiation, the beam current was initially set to 10 µA, but after a radiation "hotspot" was found outside of the cave this was reduced to 1 µA. Upon correction the beam was brought back up to about 5 µA. The 40 MeV irradiation had a more stable beam current, but was limited closer to 4 µA. For both cases, the beam current on the breakup target was recorded at approximately 5 minute intervals, and the Bateman equations were used to correct for any variation.

The irradiation length was based on the time allotted by the cyclotron operations. The 33 MeV irradiation lasted 7.51 days, and the 40 MeV irradiation lasted 3.69 days. For both cases, this was significantly less than the 14.9 (2) day half-life of ^{225}Ra, so there were no additional uncertainties associated with saturation of the ^{225}Ra activity.

Minimizing the beamspot size, and aligning the sample with the beam, were important to increase the flux on the radium sample at a given beam current. A larger beamspot will increase the average angle of emission relative to the small sample, an effect which is

amplified by having the sample placed so close to the breakup target. Because the deuteron breakup emission spectrum is highly forward focused, the difference in the relative angle of emission will impact the flux significantly. Also, the geometric ($1/r^2$) effects on the solid angle cause a smaller beamspot to have a higher flux.

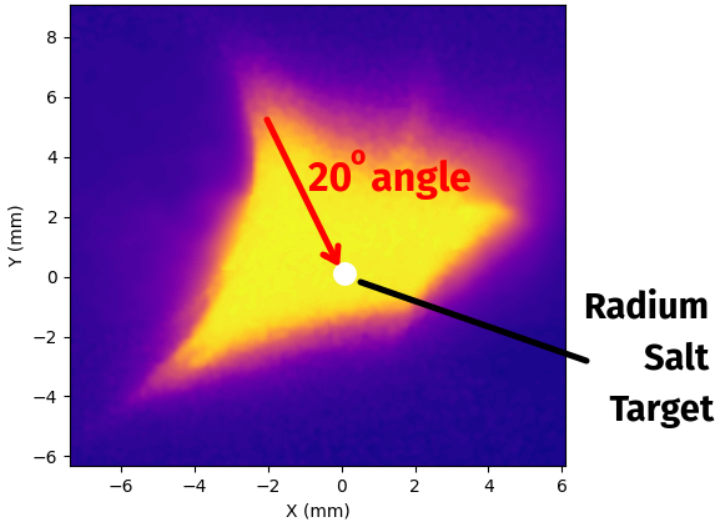

Figure 4.2: 2D contour plot of the beam intensity incident on the target, showing the significant angular spread relative to the radium sample.

Figure 4.2 shows a scan of the beam profile incident upon the breakup target at 33 MeV, that was acquired using radiochromic film (Gafchromic EBT3). The coordinates of the scan are relative to the location of the radium sample. With the radium located only 19 mm from the breakup target, the emission angle, and consequently the neutron spectrum, is highly dependent on this beam profile. Also, the beam was not perfectly centered on the target, which had to be corrected for.

In order to account for this, these beamspot scans were used to simulate the flux spectrum witnessed by the radium sample and the monitor foils, using the hybrid deuteron breakup model presented in chapter 3. This was also important to determine the neutron fluence over the radium sample, as the value computed for the neutron monitor foils required correction for the significantly different geometry.

Activation Analysis

Because ^{225}Ra β^- decays without any α or strong γ emissions, there was an approximately 2–3 week waiting period after the irradiation for the in-growth of ^{225}Ac and its short-lived decay products. This was also operationally required, as the ambient radiation levels in

Cave 0 were too high for safe entry. Unfortunately, this meant that the ^{224}Ra ($t_{1/2}$ = 3.6319 (23) d) produced by the (n,3n) reaction decayed significantly before the sample was analyzed. Furthermore, because ^{224}Ra was already present in the sample from the ^{228}Ra decay chain, the additional ^{224}Ra production through the (n,3n) reaction channel could not be quantitatively measured within reasonable uncertainties.

Following the 33 MeV irradiation, the sample was initially assayed using γ spectroscopy, in an attempt to observe the 218 keV γ-ray from ^{221}Fr decay (I_γ = 11.44 (12)%) and the 440.45 keV γ-ray from ^{213}Bi decay (I_γ = 25.94 (15)%). While the 440 keV γ-ray was visible, the presence of a significant Compton background from the ^{226}Ra decay products (primarily ^{214}Pb) meant that the systematic uncertainties associated with peak fitting were unacceptably high for quantitative analysis. Fortunately, the results from α spectroscopy were much more successful.

After about 20 days of decay time following the end-of-bombardment (EoB), the radium samples were transferred to the Heavy Elements Research Lab (HERL) for α spectroscopy and an actinium/radium chemical separation. The samples were taken out of the quartz vial, and the $Ra(NO_3)_2$ was dissolved in weak nitric acid over a period of several hours. A small aliquot was sampled from this solution, and baked onto a metal backing foil in a very thin layer, using an inductive heater. This released any radon gas in the sample, and consequently the ^{226}Ra decay products were not in secular equilibrium. This sample was then counted at HERL using an ORTEC alpha spectrometer and digital MCA, over a period of approximately 24 hours.

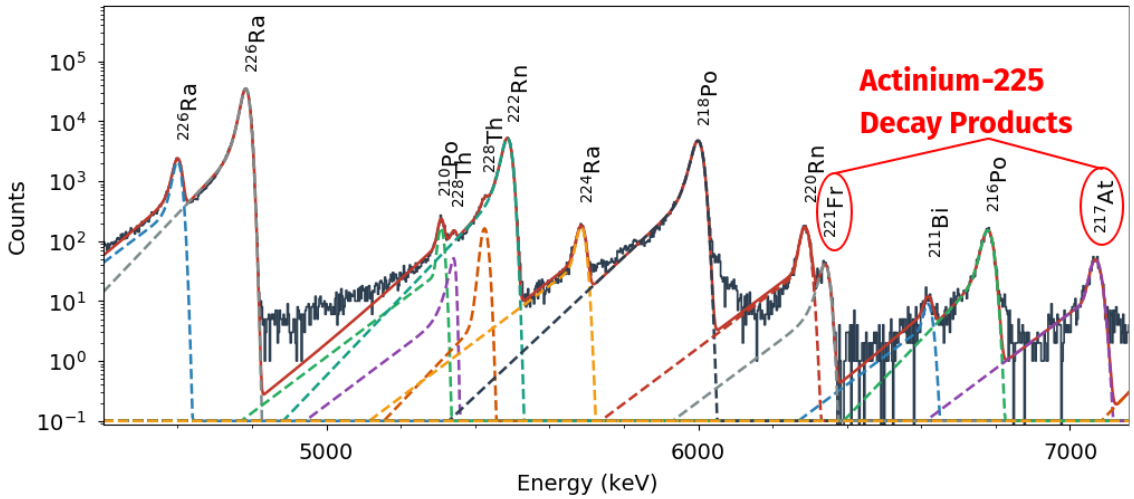

Figure 4.3: α spectrum of the radium sample after irradiation, with ^{225}Ac decay products highlighted in red.

The α spectrum from the sample irradiated at 33 MeV can be seen in figure 4.3. ^{225}Ac has multiple alpha branches near 5.8 MeV, which were mostly obscured by the tail of the 6.002 MeV ^{218}Po peak. However ^{221}Fr, ^{217}At and ^{213}Po all have high energy alphas that were clearly separable from the other ^{226}Ra decay products. Each peak was fit using a Gaussian function with a two-component exponential tail, to account for the low-energy straggling. These were used to quantify the ^{225}Ra production rate, which is needed to calculate the flux-averaged (n,2n) cross section according to the well-known activation equation

$$\langle \sigma_{n,2n} \rangle = \frac{R_{Ra-225}}{n_{Ra-226} \cdot \langle \phi(E_n) \rangle} \tag{4.1}$$

Because the alpha spectrum was collected with only a small aliquot of the dissolved radium target solution, the ^{225}Ra activity was determined by calculating the ratio of ^{225}Ra decays observed in the spectrum to the number of ^{226}Ra decays, and multiplying that ratio by the known initial radium target activity. Because the number of radium atoms n_{Ra-226} in equation 4.1 is also proportional to the radium activity, the average cross section $\langle \sigma_{n,2n} \rangle$ can be determined without the radium activity at all. This slightly reduces the systematic uncertainty in the reported cross sections, although the radium mass would not have been a very large source of uncertainty as it can be quite accurately determined by γ spectroscopy.

The average neutron flux $\langle \phi(E_n) \rangle$ was determined using the following monitor reactions on the nickel and yttrium foils: $^{\text{nat}}$Ni(n,x)^{58}Co, $^{\text{nat}}$Ni(n,x)^{57}Ni, ^{89}Y(n,2n)^{88}Y, and ^{89}Y(n,3n)$^{87\text{m+g}}$Y. These foils were counted on the same ORTEC GMX Series (model GMX-50220-S) High-Purity Germanium (HPGe) detector that was described in chapter 2. The detector energy and efficiency calibrations were performed using the following standard calibration sources of known activity, traceable to NIST: ^{152}Eu, ^{133}Ba, ^{137}Cs and ^{60}Co. The monitor foils were counted between 60–80 cm from the front face of the detector, to keep the detector dead time below about 10%.

The neutron energy spectrum incident on the monitor foils was calculated via numerical integration using the beamspot scans and the deuteron breakup model described in chapter 3. This spectrum was then used to determine an average cross section for each of the monitor reactions, and a flux value was determined for each channel. The average of these was taken and multiplied by a correction factor, to account for the difference in flux expected between the radium sample and the monitor foils due to the monitor foils being much larger than the radium, and further away from the source. This corrected average flux $\langle \phi \rangle$ could then be used to determine the average (n,2n) cross section, for each of the 33 and 40 MeV measurements.

Chemical Separation

Only a small aliquot from the solution of dissolved $Ra(NO_3)_2$ was used for preparing the α spectroscopy target. The rest of the solution was then run through a resin based cation-exchange column at HERL, to separate out the actinium from the bulk of the radium target. The sample used in the 33 MeV irradiation was separated using a DGA column. The sample from the 40 MeV irradiation was, however, split into two equal parts. One was again separated using DGA [151], and the other was separated with an AG50 column [152], in order to compare the two separation techniques.

The separated actinium solution was then transferred back to the counting facility at the 88-Inch cylotron, where the samples were counted over a period of several months using the same detector described for the monitor foil assay. Because the samples were in liquid form, a combination of a liquid ^{152}Eu/^{154}Eu source and Monte Carlo modeling were used to correct for the effects of attenuation in the liquid sample. This correction factor was typically between 20–30%, depending on the γ-ray energy.

The purpose of the separation and counting was to search for any potential impurities co-produced in the irradiation. While ^{227}Ac production from ^{226}Ra(n,γ) was the primary concern, it is possible that ^{226}Ra could fission at the neutron energies present in this experiment, creating radioactive fission products that could impact medical applications.

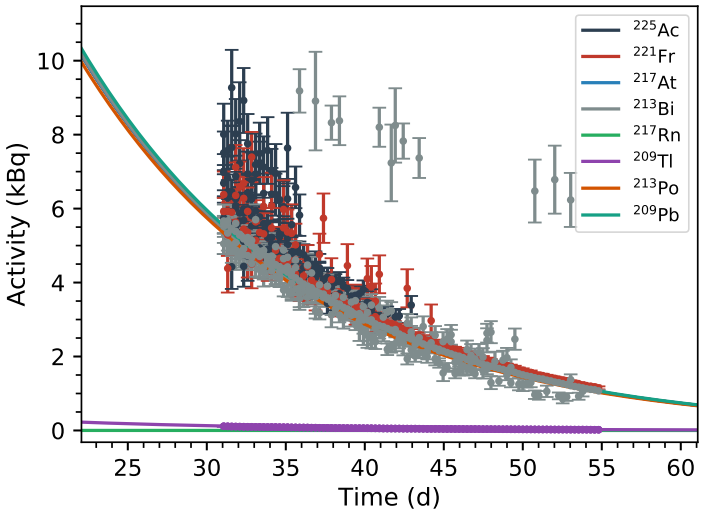

Figure 4.4: Measured decay curve of the ^{225}Ac sample after chemical separation through the DGA column. Note that some spurious counts were seen from poor fits to the 0.167%, 324 keV peak in ^{213}Bi, however these had a negligible impact on the resulting fit.

The separated ^{225}Ac was also compared to the ^{225}Ac activity quantified by α spectroscopy,

in order to determine the chemical recovery of actinium for the both columns. Figure 4.4 shows the decay curve fitted to the measured ^{225}Ac activities in the separated sample, from the 33 MeV experiment. In this case $t = 0$ is the time that the chemical separation began. The recovery of ^{226}Ra in the purified actinium solution was also measured, in order to calculate the separation factor

$$SF = \frac{A_f/A_i(^{225}\mathrm{Ac})}{A_f/A_i(^{226}\mathrm{Ra})}$$

where A_i and A_f are the activities of each isotope in the initial, and final (separated) solutions, respectively.

4.3 Results

In spite of the large background activity from the ^{226}Ra target, the production rates of ^{225}Ra were able to be successfully quantified with α spectroscopy, at an accuracy of about 10%. These production rates, for the 33 and 40 MeV irradiations, are presented in table 4.1 and table 4.2 respectively, along with some of the irradiation parameters for each measurement. Using equation 4.1, along with the radium mass and the average neutron fluxes determined from the monitor foils, the average (n,2n) cross section was calculated for each irradiation.

The resulting cross sections are plotted in figure 4.5, in comparison with the TENDL-2015 and ENDF/B-VII.1 evaluations, and the O'Connor measurement at 14.5 MeV.

Note that the mean energy in this plot was chosen to *only* account for the mean energy of neutrons with $E_n > E_{thresh}$, which is 6.425 MeV for the ^{226}Ra(n,2n) reaction. This is because neutrons lower than the threshold energy do not contribute to the ^{225}Ra activation, and would therefore be improperly weighted. This was also done for the mean energies reported in tables 4.1 and 4.2. Also, the energy errorbar in the above plot represents the $\pm 1\sigma$ widths of the energy distribution, rather than the uncertainty in the mean energy.

Because flux-averaged cross sections can be somewhat difficult to interpret on their own, a "recommended" cross section was derived from these results. To obtain this, a fitting procedure was performed in which the TENDL cross section was multiplied by a two-term logarithmic polynomial, the parameters of which were adjusted to best fit the measured average cross sections. This is a somewhat arbitrary method for adjusting the cross section, however it is useful for visualizing the changes to the shape and magnitude of the cross section that best reproduce the experimental measurements. Also, to help visualize how the measured average cross sections compare to the evaluations, the flux-averaged cross sections for each library are plotted with an "$\times$" of the same color. These averages are also reported in tables 4.1 and 4.2.

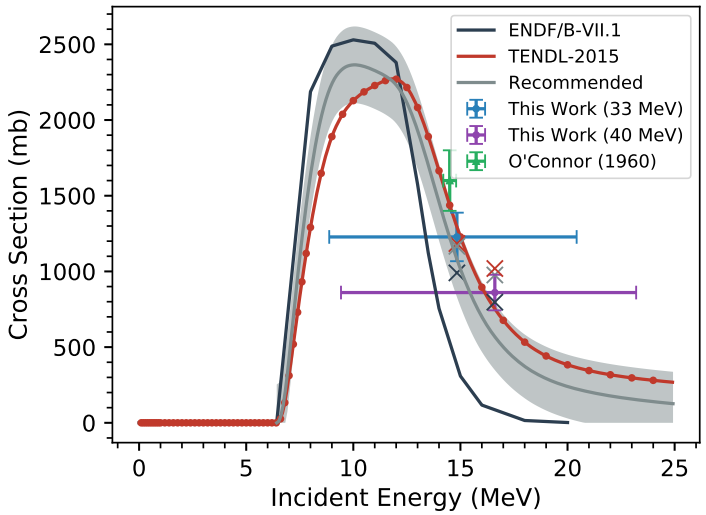

Figure 4.5: Measured ^{226}Ra(n,2n)^{225}Ra cross sections, along with ENDF and TENDL evaluations. The grey line indicates a "recommended" cross section based on the measured values. Points marked with "×" show flux-averaged cross sections for each library. The x-error bar in the the measured values represents the $\pm 1\sigma$ widths of the neutron energy distribution over the (n,2n) threshold.

The measured average cross sections were above either TENDL or ENDF for the 33 MeV measurement, and in between the two for the 40 MeV measurement. Based on this and the "recommended" cross sections that were fit to the measured values, the TENDL evaluation seems to predict this channel cross section better than ENDF. One theory for why this might be the case is that the (n,2n) and (n,3n) measurements by O'Connor were somehow reversed in the ENDF evaluation, as the ENDF value of 546 mb is quite close to the (n,3n) measurement by O'Connor of 630 ± 70 mb. Regardless of the reason, the fact that the measurements support the TENDL cross section has a rather significant implication for the ^{225}Ac yields from this pathway. If the ENDF cross sections were correct, raising the incident beam energy much beyond about 40 MeV would have no increase in the ^{225}Ra yield, as the cross section for those higher energy neutrons would be almost zero. However because this is not the case, it may be advantageous to operate this pathway at even higher incident deuteron energies. This will be explored further in chapter 5.

It should be noted that the measured ^{225}Ra production rates, per unit deuteron beam current, per unit mass are approximately the same at both 33 MeV and 40 MeV incident beam energies, at least within the margin of error. This would seem to be in contradiction to the previous statement about operating at higher deuteron beam energies. However, this discrepancy is likely due to a difference in beam-sample geometries, arising from the thicker

Deuteron Energy	33 (MeV)
Average Current	3.89 (µA)
Integral Current	701.9 (µAh)
Irradiation Time	7.51 d
Decay Time	18.9 d
$R_{\text{Ra-225}}$	$(3.48 \pm 0.37) \times 10^5$ (s^{-1})
Produced ^{225}Ac	1.40 ± 0.15 (µCi)
Recovered ^{225}Ac (DGA)	0.84 ± 0.01 (µCi)
^{226}Ra Target Activity	0.813 ± 0.033 (mCi)
Recovered ^{226}Ra (DGA)	35.1 ± 0.4 (nCi)
Actinium Recovery	60%
Radium Recovery	4.3×10^{-3} %
Ac/Ra Separation Factor	13900
Total Neutron Fluence	$(4.26 \pm 0.32) \times 10^{16}$ (cm^{-2})
Average Neutron Energy	14.8 (MeV)
Measured ^{226}Ra(n,2n) XS	1227 ± 160 (mb)
ENDF Average XS	990 (mb)
TENDL Average XS	1184 (mb)

Table 4.1: Irradiation parameters and results from the experiment at $\epsilon_d = 33$ MeV.

beryllium target and differences in the beamspot between the two tunes. The end result is that the effective solid angle of the radium target in the 40 MeV experiment was about 15% lower than at 33 MeV. This effect is accounted for in the reaction cross sections.

The results of the γ-spectroscopy assays of the separated ^{225}Ac are reported in table 4.1 and 4.2. This includes the ^{226}Ra and ^{225}Ac activities, both before and after irradiation, which have been decay-corrected to the activities at the separation time, which is in turn given relative to the EoB as "decay time" in the above tables.

The results of this showed a good separation factor for the DGA method, but a rather poor separation factor for the AG50. In this case, the separation factor was the ratio of the actinium to radium recovery. For DGA, the separation factor was about 14,000, averaged between the two measurements. This is important if the (n,2n) pathway is to be considered for medical purposes, as ^{226}Ra is long-lived, highly cyctotoxic, and cannot be tolerated in the processed ^{225}Ac solution. The separation factor for AG50, however, was only 12.7, which is quite poor. In fact, more ^{226}Ra activity was in the AG50 solution than ^{225}Ac.

For all three separations, the actinium recovery was quite poor, at only about 40-60%. Ideally, the recovery and the separation factor would be slightly better, however this requires optimizing certain variables like the pH of the solution, or testing different rinse solutions

Deuteron Energy	40 (MeV)
Average Current	3.68 (µA)
Integral Current	326.8 (µAh)
Irradiation Time	3.69 d
Decay Time	20.8 d
$R_{\text{Ra-225}}$	$(3.86 \pm 0.52) \times 10^5$ (s^{-1})
Produced ^{225}Ac	0.77 ± 0.10 (µCi)
Recovered ^{225}Ac (DGA)	0.143 ± 0.002 (µCi)
Recovered ^{225}Ac (AG50)	0.168 ± 0.003 (µCi)
^{226}Ra Target Activity	0.999 ± 0.034 (mCi)
Recovered ^{226}Ra (DGA)	12.8 ± 0.6 (nCi)
Recovered ^{226}Ra (AG50)	17.7 ± 0.2 (µCi)
Actinium Recovery (DGA)	37%
Radium Recovery (DGA)	2.6×10^{-3} %
Ac/Ra Separation Factor (DGA)	14500
Actinium Recovery (AG50)	44%
Radium Recovery (AG50)	3.5 %
Ac/Ra Separation Factor (AG50)	12.7
Total Neutron Fluence	$(2.93 \pm 0.12) \times 10^{16}$ (cm^{-2})
Average Neutron Energy	16.6 (MeV)
Measured ^{226}Ra(n,2n) XS	860 ± 117 (mb)
ENDF Average XS	797 (mb)
TENDL Average XS	1019 (mb)

Table 4.2: Irradiation parameters and results from the experiment at $\epsilon_d = 40$ MeV.

and sequences, for example [153, 154]. The results of this optimization might also depend on the relative concentrations of the actinium analyte and radium interferent. Unfortunately, the low total mass of actinium in this study prohibited such an optimization, but should be performed in the future if this pathway is to be pursued. However, the preliminary results obtained here suggest that the DGA resin has a significantly better selectivity for actinium than AG50.

Possible Contaminants

The main contaminant of concern for this production pathway is ^{227}Ac, which could be produced via ^{226}Ra(n,γ) with neutrons that have thermalized in the cave shielding, and returned to the sample. While the expected rates of this are low, and the ^{227}Ac can be

cleanly separated due to the short half life of the ^{227}Ra parent (42.2 (5) m), it is still valuable to attempt to quantify any that is produced.

While no ^{227}Ac was seen directly, 0.51 ± 0.04 µCi of ^{211}Bi was observed via alpha spectroscopy of the 33 MeV samples. If this were from ^{227}Ac it would have been easily visible in the γ-ray spectrum, however neither ^{227}Ac nor any of its decay products were observed in the spectra from the separated actinium solution. Also, 0.64 ± 0.04 µCi was observed from the 40 MeV sample, a 25% increase despite the integral beam current being half what it was at 33 MeV. This suggests that the ^{211}Bi originated from ^{223}Ra decay, which is be produced via the ^{226}Ra(n,4n) reaction, rather than through ^{227}Ac decay. According to TENDL this reaction cross section is expected to threshold at 20 MeV and peak at about 28 MeV, which is consistent with the increased ^{211}Bi activity for the 40 MeV measurement. While ^{227}Ac could still be present at very low activity levels, none was observed in either measurement after several months of counting time.

Contaminants from fission were also a possible concern, as ^{226}Ra fission has been reported at excitation energies as low as 23 MeV [155]. However no fission products were observed in the separated actinium solutions. Certain oxidation states of lanthanides have been shown to exhibit similar chemistry to actinium, and could potentially be highly recovered by the cation-exchange separation [156]. These usually have fission yields of several percent in thorium, such as ^{140}La, however none were observed in the measured γ-ray spectra.

Scaling Production

Based on the measured production rates, the ^{225}Ac yields for this pathway scale at approximately 2.4 mCi/(mAh·g$_{Ra}$) at 33 MeV. This is assuming the irradiation time is short relative to the ^{225}Ra half-life, and that the beam is not significantly attenuated by the radium sample. The effects of this will be explored further in chapter 5. While the beam current in this experiment was limited to about 4 µA due to radiation shielding limitations, a purpose built cyclotron, custom tuned to run high intensity deuterons, could conceivably operate at currents up to 600 µA [157]. Also, because all the samples in this experiment were manipulated by hand, only one milligram of radium was irradiated due to radiation safety concerns with large quantities of radium. However, most large scale production facilities tend to have remote manipulators and hot-cells surrounding their production targets, and could safely handle much larger quantities of radium.

Many hospitals maintain an inventory of radium needles that historically were used for brachytherapy [40], which typically contain 10–100 mg of radium. These are generally considered waste, and could be collected and repurposed as production targets relatively easily. If, however, radium were in short supply, it is part of the ^{238}U decay chain and could be chemically removed from uranium ores. However this is obviously a much more costly approach

than repurposing radium waste products. Either way, it is not unreasonable to assume that a target of 10 grams of radium or more could be collected into a production target. Because the radium in this production pathway will not be significantly heated by neutrons, the chemical form of this target could be quite flexible.

Based on a scaling of our measured production rates, a 10 gram radium target irradiated at 33 MeV with a 600 µA deuteron beam over 5 days would produce 1.73 Ci of ^{225}Ac. In our experiments, the radium sample was placed approximately 20 mm away from the breakup target. In an engineered production target, the radium could likely be located much closer, which would increase the neutron flux due to the larger solid angle. Realistically, with internal water cooling of the target, the radium could perhaps be located 10 mm from the source, which would raise the yields to 7 Ci. However if the beamspot is large, which may be required to operate at such high beam currents, the effect of moving the radium closer may not be as significant. The impact of the beamspot size on the yields will be investigated further in chapter 5. Also, this 7 Ci estimate is based on a single ^{225}Ac extraction from the target. Because ^{225}Ra will continuously feed into ^{225}Ac, multiple extractions could be performed, potentially doubling the total amount of ^{225}Ac that can be recovered. At this order of magnitude, the ^{226}Ra(n,2n) pathway is very compelling for producing ^{225}Ac for widespread clinical use.

4.4 Conclusions and Future Work

We have demonstrated the viability of this pathway to produce ^{225}Ac, with a high radiopurity, and have performed an initial exploration of the chemical processing steps required to extract ^{225}Ac from a radium target. While the scaling of this pathway will be considered further in chapter 5, the initial results suggest that this pathway could be used to produce ^{225}Ac in quantities relevant to widespread availability for research and treatment. The results suggest that a beam current on the order of 100-500 µA and a radium target on the order of 10 grams could accomplish this. The technical challenges related to this pathway are relatively straightforward, mainly concerning radiation shielding and remote target handling of a larger radium target, and optimizing the breakup target design such that the radium sample can be located as close as possible. In future target designs, it may be advantageous to use a recirculating liquid lithium target, as it could sustain high currents and produces about 30% higher neutron yields per incident deuteron than beryllium. An example target of this sort is the LiLit neutron production target at the SARAF facility [118].

Future work for this pathway should be focused on understanding how to scale up the production. There are two main areas where improvements could be made. One is on understanding how the mass and geometry of the target affects the production scaling. This

will be investigated in chapter 5, however the effects of elastic and inelastic scattering within a large target are sources of uncertainty. Also, the yields could potentially be improved by using a neutron reflector. However depending on the design, this could also create a significant thermal neutron flux, which would lead to the production of more ^{227}Ac through the (n,γ) reaction.

Experimentally, understanding the behavior of the target geometry and mass scaling could be studied using a surrogate target of a similar atomic mass, such as thorium, that is simpler to work in a lab setting in larger quantities. Additionally, more detailed studies of the radium/actinium separation chemistry should be performed, to improve the actinium recovery, and the separation factor. This could be optimized using ^{227}Ac, as it is relatively more available, and longer lived than ^{225}Ac. This may include optimizing the load pH, evaluating different rinse solvents and sequences, and testing various cation exchange resins. While this type of optimization has been performed for radium/actinium samples that were produced from thick target thorium irradiations [154], the relative concentration levels of the two elements was very different than what is relevant to ^{225}Ac production routes using radium targets.

Relevant Nuclear Data

Isotope	α Energy (keV)	I_α (%)	$T_{1/2}$
^{226}Ra	4601	6.16 (3)	1600 (7) y
	4784.3	93.84 (11)	
^{210}Po	5304.3	100	138.376 (2) d
^{228}Th	5340.36	26 (1)	1.9125 (9) y
	5423.15	73.4 (5)	
^{222}Rn	5489.48	99.92 (1)	3.8235 (3) d
^{224}Ra	5685.37	94.92 (5)	3.6319 (23) d
^{218}Po	6002.35	99.9789 (23)	30.098 (12) m
^{220}Rn	6288.08	99.886 (17)	55.6 (1) s
^{211}Bi	6622.9	83.54 (14)	2.14 (2) m
^{221}Fr	6341	83.4 (8)	286.1 (10) s
^{216}Po	6778.3	99.9981 (3)	0.154 (2) s
^{217}At	7066.9	99.89 (1)	32.3 (4) ms
^{215}Po	7386.1	99.99977 (1)	1.781 (4) ms
^{214}Po	7686.82	99.9895 (6)	163.6 (3) µs
^{213}Po	8376	100	3.72 (2) µs
^{212}Po	8784.86	100	0.299 (2) µs

Table 4.3: Principle α-emission data from ENSDF [20–22, 49, 50, 158–166].

Chapter 5

Comparing ^{225}Ac Production Pathways

The intention of this chapter is to attempt a fair comparison between the myriad of possible production pathways for ^{225}Ac. There are many things to consider when judging the performance of an isotope production route. First there is the total yield of the isotope of interest. Then there is the radiopurity, which is important in nuclear medicine for minimizing unnecessary dose to patients. Another consideration is whether the isotope can be made carrier-free, with a means of separating out unnecessary stable isotopes either through chemistry or otherwise. This is not likely to be a significant concern for ^{225}Ac, most isotopes in the same mass region are relatively short-lived, but is important for other isotopes. Fission is likely to be a concern for isotopic purity in this mass region, and may significantly complicate the chemical recovery of ^{225}Ac. The co-production of long-lived nuclear waste may also be a factor in evaluating a pathway, depending on the scale of production. These considerations are mostly based on the physics of the nuclear interactions of the beam with the target, and can be evaluated without very specific knowledge of the isotope production facility itself. It is upon these merits that we will be primarily evaluating each pathway in this chapter.

There are, however, many other considerations specific to an individual production facility that may outweigh these factors when determining the "best" pathway for a given facility. The foremost, and most difficult to evaluate on a scientific basis, will probably be the cost. There are also many engineering considerations when performing isotope production at a large scale. The target cooling could be a significant limitation for certain pathways, as these requirements depend on the target material and the intended scale of production. Some facilities may choose not to handle certain targets, either because of the target's chemical properties or its radioactivity before or after irradiation. Lastly, as these pathways may

not utilize the whole range of the beam, it is challenging to compare the potential for co-production of other desirable radionuclides. Because these considerations vary depending on the facility, it is impossible to make claims about a "best" production pathway for ^{225}Ac, absent other considerations. Instead, the goal of this chapter is to examine the general trends in each production pathway under a similar set of operating conditions.

To achieve this, it was decided to compare the yields of each pathway at a constant beam power of 25 kW. This constraint was chosen because the ultimate engineering limitation when scaling up isotope production is the amount of heat that can be dissipated from the target, which primarily depends on the total beam power. This leads to a general trend among accelerators for isotope production, that high energy facilities tend to run lower beam currents than low energy facilities (and vice versa) [32]. 25 kW was chosen as the reference beam power, because this is the rated beam power of the Los Alamos Neutron Science Center's Isotope Production Facility (IPF) [92]. Seeing as the rated beam powers of several large scale isotope production centers provided by ref. [32] cover the 10–60 kW range, 25 kW can be justified as a realistic median value for this comparison. It should be noted that another fundamental constraint is the linear heat generation rate, which depends on the stopping power of the beam in question within a given material. This will limit the maximum permissible beam power for certain pathways. However, when determining the "optimum" production energy for a specified beam and target combination, this effect can be largely neglected.

In addition, because multiple target materials were compared, and the relative energy deposition within each target varies significantly for each approach, a basic thermal comparison was performed. Again, the exact thermal constraints for a given pathway will be unique to each facility, but this comparison is useful for understanding the relative difficulty of target cooling for each approach.

5.1 Introduction

Actinium-225 is a rare, challenging isotope to produce because it is not a decay product of any significant naturally abundant actinides, and there are no stable targets of a similar atomic mass from which to produce it. ^{226}Ra is the closest target material that could likely be obtained in gram to tens of gram quantities, however it is highly radioactive and chemically hazardous as well. Natural thorium is probably the nearest target that could be obtained in bulk (kilogram) quantities, and is not a dangerously radioactive target to prepare. Although there are a few other possible target materials (e.g. ^{228}Ra, ^{230}Th, ^{228}Th), they are not likely to be available at the same level as radium and thorium, so we will limit this comparison to pathways using ^{226}Ra and ^{232}Th targets [32].

We will split the different pathways into two categories, direct and secondary particle pathways, mostly based on the calculation methods associated with each comparison. For direct production pathways, an accelerated charged particle beam impinges directly on the radium or thorium target, whereas for the secondary particle pathways the incident beam impinges on a conversion target, and a beam of secondary particles is produced that goes on to react with the isotope production target. For direct production, thick target yields are relatively simple to compute, as they only depend on the production cross section, the areal density, and the stopping power in the target. For the secondary particle routes, the angle and energy distributions of the secondary particles must be well characterized, and the yields are dependent on the beam geometry, target mass and target geometry.

5.2 Direct Production Pathways

A common way to report thick target yields for a given pathway is in units of activity per unit charge, e.g. Ci/µAh. Since we would like to make a comparison at a fixed beam power, we will instead report the thick target production rates R as a function of energy, and any other variables of interest. The production rate R, which is equivalent to the saturation activity, can be determined for a direct production pathway with the equation

$$R = \rho_N \cdot I_p \int_0^{E_{inc}} \sigma(\epsilon_p) \Big(\frac{d\epsilon_p}{dx}\Big)^{-1} d\epsilon_p \tag{5.1}$$

where $\rho_N = \rho \cdot N_A/M$ is the number density of the target, $d\epsilon_p/dx$ is the stopping power in MeV/cm, σ is the production cross section, and I_p is the proton beam current in units of particles/sec. Because this comparison is being performed at a fixed beam power, the beam current is inversely related to the incident energy by $I_p = P/(e \cdot E_{inc})$.

This relationship provides a better indication for the optimum incident energy of a given production route than a typical thick target yield calculation. Because of the cumulative nature of thick target yields, the production rate always increases with increasing energy (for a fixed beam current). This would seem to indicate that the optimum energy is always the highest energy. However because beam power is often a fundamentally limiting engineering constraint, a lower beam energy of a proportionally higher intensity may have a higher yield.

Based on Eq. 5.1, this point of optimum energy depends on two factors: the energy dependence of the cross section, and the stopping power. At high energy, proton stopping powers are proportional to $1/\beta^2 \propto 1/E$. This means that at a fixed current, the saturation activity tends to increase proportional to E_{inc}^2, or proportional to E_{inc} for a fixed beam power. For the cross section, many reactions will have a characteristic compound peak, above which the cross section drops rather significantly. This will impact the optimum production energy.

However, not all reactions will demonstrate this behavior, particularly if they have high energy thresholds.

The three direct production pathways evaluated here are ^{232}Th(p,x)^{225}Ac, ^{226}Ra(p,2n)^{225}Ac, and ^{232}Th(p,4n)^{229}Pa for the production of the ^{225}Ac generator isotope ^{229}Th. There were a few other pathways considered, but left out of the comparison for the sake of brevity. The ^{nat}U(p,x)^{225}Ac pathway shares many of the same characteristics as the ^{232}Th(p,x) approach, but has about a factor of 10 lower cross section, and no obvious advantages. The ^{230}Th(p,2n) [167], ^{230}Th(d,3n) and ^{232}Th(d,5n) reactions have many of the same characteristics as the ^{232}Th(p,4n), however ^{230}Th is much less abundant than ^{232}Th. According to TENDL ^{226}Ra(d,3n)^{225}Ac may have a larger cross section than the (p,2n) approach, however there is no literature data to support this.

^{232}Th(p,x)^{225}Ac Pathway

The advantage of the ^{232}Th(p,x)^{225}Ac pathway is that reasonably high yields of ^{225}Ac can be produced, without the engineering or safety concerns associated with a radium target. This is particularly true for higher energy proton accelerators. Thorium is also a widely available material, and may not need to be reprocessed after each irradiation. From an engineering perspective, high currents can reasonably be run on a thorium target, as thorium metal (the preferred form for this application) has a thermal conductivity of $k = 54$ W/m·K, and ThO_2 has $k = 20$ W/m·K [168]. As many isotope production centers are based around high energy proton accelerators, this approach is particularly well suited to the existing infrastructure.

Multiple experimental measurements of this reaction channel have been performed, as shown in figure 5.1. The TENDL (2015) prediction for this channel was systematically a factor of ≈2.5 times higher than what was observed experimentally, and was scaled down by a factor of 0.4. There was also a peak in the TENDL prediction at about 50 MeV, corresponding to the ^{232}Th(p,α4n) partial cross section, that does not seem to be reproduced by experiment. While this reaction cross section of about 5–15 mb is relatively low, the range of high-energy protons is significant enough to make this reaction channel compelling for large scale production.

Unfortunately, the cross section for the production of ^{227}Ac is almost as large. Figure 5.2 again shows a comparison of the literature measurements to TENDL-2015. There is a similar scaling factor of 0.4 that had to be applied to the TENDL cross section to better agree with the experimental values. ^{227}Ac is the primary contaminant of concern with ^{225}Ac alpha therapy, as it is the only long-lived actinium isotope ($t_{1/2} = 22.772$ (3) y). Depending on the long term bio-kinetics of chelated actinium, the presence of ^{227}Ac may (or may not) represent a risk for clinical use. There will also be significant fission product contaminants

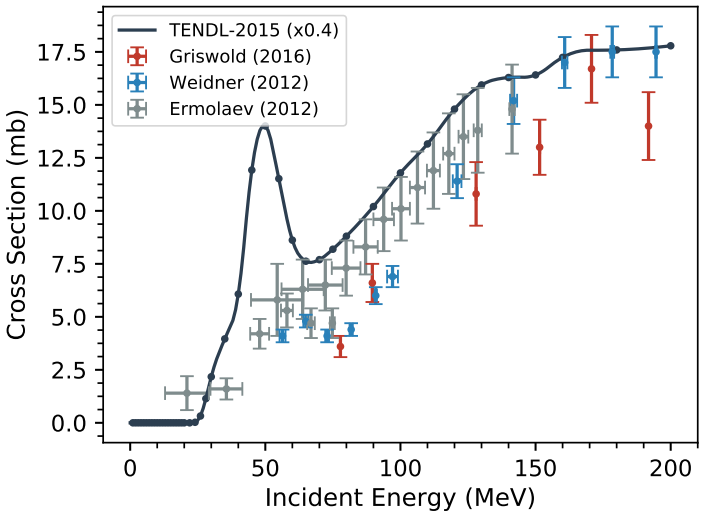

Figure 5.1: Measured and evaluated cross sections for the ^{232}Th(p,x)^{225}Ac reaction. TENDL has been multiplied by 0.4 to better reproduce the experimental data.

produced by the high energy proton reactions on ^{232}Th, however most, if not all of these can generally be chemically separated out from the final actinium solution, unlike ^{227}Ac.

Based on these cross section values, ^{227}Ac atoms will be produced in an approximately 2:3 ratio to ^{225}Ac, comprising 0.047% of the total activity. This ratio will change as the atoms decay; 10 days after irradiation ^{227}Ac will represent a 0.067% radio-impurity, for example. At these impurity levels the dose rate from ^{227}Ac will not be very high, however if it is not cleared from the body the integrated dose over a patient's lifetime could be very significant. Long term studies on the bio-distribution of ^{227}Ac used in TAT molecules have yet to be performed to determine if this is a significant concern.

The 25 kW yields for this pathway as a function of proton energy can be seen in figure 5.3. Very little ^{225}Ac is produced below 50 MeV, however the saturation activity grows roughly linearly with energy due to the dependence on the proton range. At 100 MeV the saturation activity is approximately 14 Ci, and it reaches about 40 Ci at 200 MeV. It's worth noting that the feature between 50–60 MeV is due to the (p,α4n) peak in the TENDL evaluation, and is not reflected in literature data.

At these production levels, this pathway is quite compelling for the production of ^{225}Ac. Pre-clinical trials suggest that ^{225}Ac alpha therapy for treatment of metastatic castration-resistant prostate cancer (mCRPC) requires about 100-200 µCi per treatment cycle, and a patient may undergo 2–4 cycles [10]. For mCRPC in the United States alone, several tens of thousands of patients could benefit from this treatment every year [35]. This puts a minimum estimate for production requirements at several 10's of Ci per year, which could

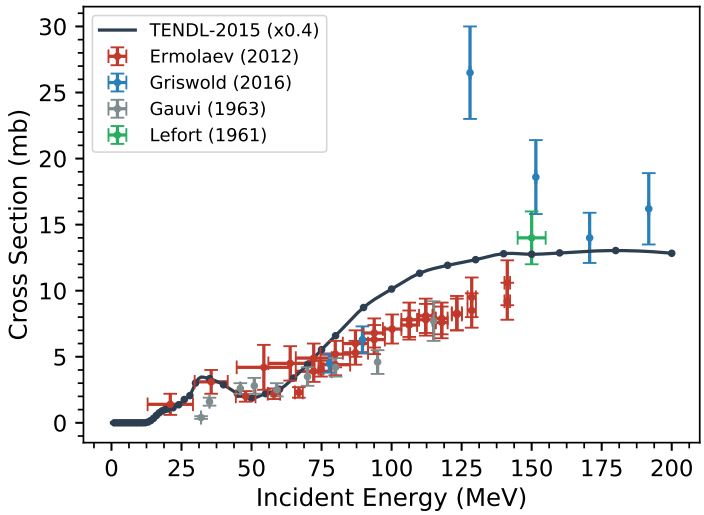

Figure 5.2: Measured and evaluated cross sections for the ^{232}Th(p,x)^{227}Ac reaction. TENDL has been multiplied by 0.4 to better reproduce the experimental data.

very reasonably be produced using the ^{232}Th(p,x)^{225}Ac production pathway.

^{226}Ra(p,2n)^{225}Ac Pathway

The ^{226}Ra(p,2n)^{225}Ac production pathway has the advantage of relatively high yields per unit of proton beam current, due to the cross section, and is produced free of significant impurities such as ^{227}Ac. It also has the advantage of being compatible with lower-energy proton accelerators, which could enable local ^{225}Ac production. The disadvantage is that radium is a challenging target material, particularly for a direct proton irradiation which will dissipate a significant amount of heat. This will likely limit the total production capability, and may require significant target engineering that would discourage local production.

Because of the relatively high yield of this pathway, one might consider local production with a low intensity beam, so as to avoid the target heating concerns. However radium is a rare, expensive and dangerous material. The range of 40 MeV protons in radium metal is about 7.1 mm. Therefore a production target with a 1 cm radius would require 11 grams of radium. Unshielded, 11 grams of ^{226}Ra would have a γ dose rate of 109 R/hr, 30 cm from the target, which is a significant hazard. Additionally, acquiring 11 grams of radium for a large number of local production sites is not likely feasible with the current supply. For these reasons, this pathway is probably best considered for regional isotope suppliers.

Figure 5.4 shows fairly good agreement between the cross section predicted by the 2015 TENDL evaluation and the single measurement of this channel performed by Apostolidis

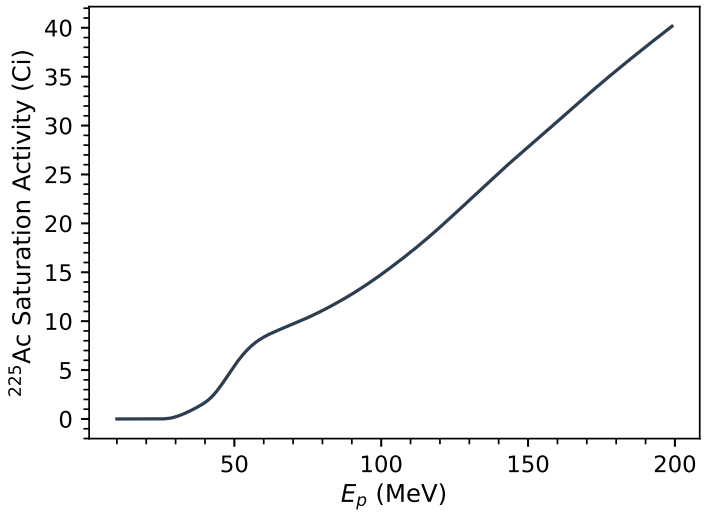

Figure 5.3: Calculated ^{225}Ac yield for the ^{232}Th(p,x) production pathway, at a fixed beam power of 25 kW.

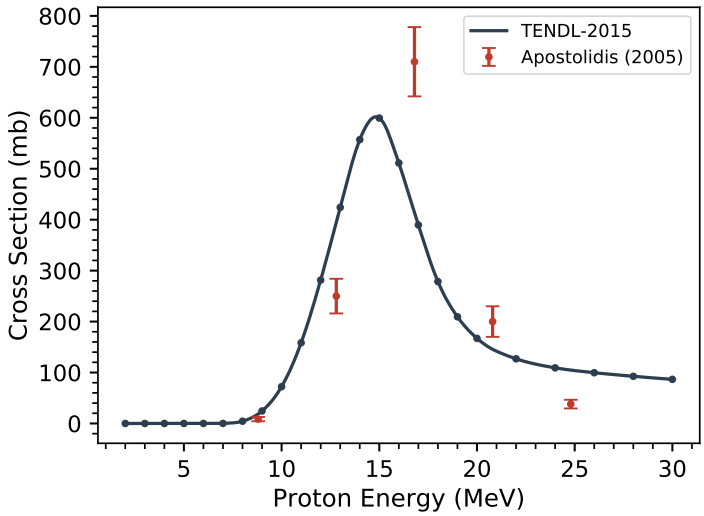

Figure 5.4: Measured and evaluated cross sections for the ^{226}Ra(p,2n)^{225}Ac reaction.

et al. in 2005 [39]. The compound peak, centered around 15 MeV, has a maximum cross section somewhere between 600–700 mb, which is significantly larger than the 5–15 mb of the ^{232}Th(p,x) channel. Despite the shorter range of these low-to-medium energy protons, this means the total ^{225}Ac yields at 25 kW beam power are quite high.

Figure 5.5 shows these yield calculations at 25 kW beam power, over the 10–40 MeV

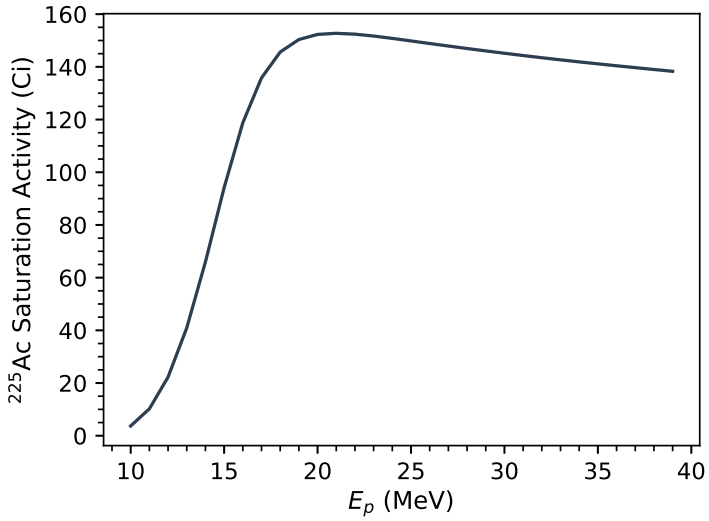

Figure 5.5: Calculated ^{225}Ac yield for the ^{226}Ra(p,x) production pathway, at a fixed beam power of 25 kW.

proton energy range. These calculations show that at a fixed beam power, the optimum proton energy for this pathway is just under 20 MeV. The ^{225}Ac saturation activity at this energy is just over 150 Ci. This was assuming pure elemental radium. Because elemental radium is extremely reactive, a more realistic target will be made of some radium compound, which will decrease these yields somewhat. While these production rates are greater than those of the ^{232}Th(p,x)^{225}Ac pathway, the challenges associated with directly irradiating a radium target at 25 kW will likely limit this approach significantly. Additionally, the risks of a loss of target containment to a large accelerator facility, which may have many other users, is an operational concern that some may decide outweigh the benefits of this approach.

Thermal Considerations

The total beam power that can be safely dissipated by the target is determined by a maximum permissible temperature rise, such that the target material does not melt, sublimate, or undergo any other type of phase change that might alter its thermal or chemical properties significantly. Without focusing on a specific target design or cooling configuration, we can still gain some insight about the limitations surrounding target cooling using the steady-state heat equation in one dimension:

$$-k\frac{d^2u}{dx^2} = q(x)$$

where k is the thermal conductivity of the target, $q(x)$ is the distribution of the volumetric heat flux, and $u(x)$ is the 1D temperature distribution in the target. For a slab centered at $x = 0$ with a homogeneous volumetric heat source $q(x) = q$ and constant temperature boundary conditions, the temperature distribution in the target will be given by the following solution:

$$u(x) = u_0 - \frac{q}{2k}x^2$$

where the temperature $u(x = 0) = u_0$ is a constant.

Intuitively, this shows that the maximum temperature is in the center of the slab. If our target is a cylinder with radius r and thickness t, absorbing a total beam power P_{abs}, the volumetric heat flux is given by $q = P_{abs}/(\pi t \cdot r^2)$. Plugging this into the equation for the temperature distribution gives a maximum temperature change of

$$\Delta u = \frac{qt^2}{8k} = \frac{P_{abs} \cdot t}{8\pi k \cdot r^2}$$

where $\Delta u = u_0 - u(x = t/2)$ is the difference between the "hot-spot" and the temperature at the slab boundaries. Re-arranging this equation will give the maximum beam power that can be permissibly absorbed by the target while keeping the maximum temperature rise below a certain value:

$$P_{max} = \Delta u \cdot \frac{8\pi k \cdot r^2}{t}$$

There are several basic insights that can be gained from this relation. The first is that the power can be increased if it is distributed over a larger area (r^2) and if the target is thin ($1/t$). For the ^{226}Ra(p,2n) production route, almost no ^{225}Ac is produced below 10 MeV, so the target does not need to be as thick as the full range of the incident proton beam. Next is that the choice of chemical form for the radium will have a very large impact on the maximum power, as it determines the maximum permissible temperature rise (based on the melting point, for example) and the thermal conductivity.

Unfortunately, little data exists for the thermal conductivity of radium, other than radium metal which is 18.6 W/m·K. However pure radium metal is not suitable due to its high chemical reactivity in air, so the most likely target material will be a powder of radium salt, such as $RaCl_2$ or $Ra(NO_3)_2$. The thermal conductivities of salts are generally very poor, even in aqueous form. For example, pure calcium has a thermal conductivity of 200 W/m·K, however $CaCl_2$ salt has a thermal conductivity of about 0.5 W/m·K, and aqueous $CaCl_2$ has a thermal conductivity only about 50% higher, depending on the concentration [169]. Some authors have suggested that radium could be smelted into a hexaboride ceramic, RaB_6, which is likely to have very good thermal properties [42], based on similar behavior from

chemically similar hexaborides. For example, lanthanum metal has a thermal conductivity of 13.4 W/m·K, however LaB_6 has a thermal conductivity of 47 W/m·K, and also a melting point of 2528 K [170]. If this is possible with radium, it could make this particular pathway much more compelling.

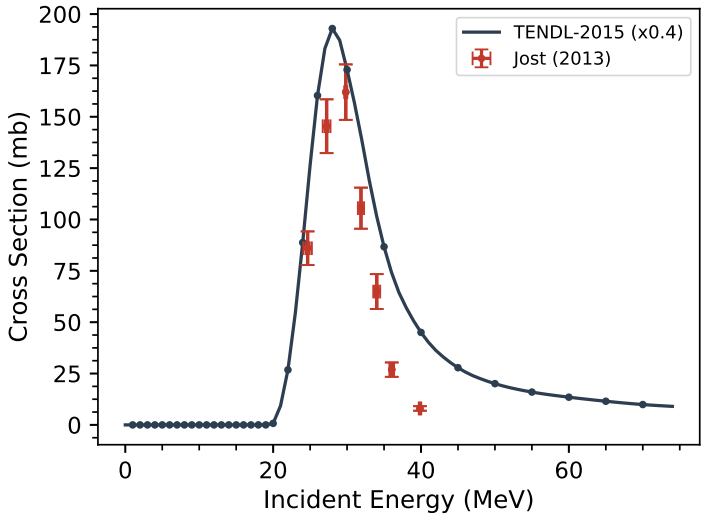

Figure 5.6: Measured and evaluated cross sections for the ^{232}Th(p,4n)^{229}Pa reaction. TENDL has been multiplied by 0.4 to better reproduce the experimental data.

For an example calculation, consider a tightly packed radium chloride target, with a thermal conductivity of 1 W/m·K. With an incident proton energy of 20 MeV, a 1.3 mm thick target would cover the 10–20 MeV range, which contains most of the reaction cross section. Using a target containing 10 grams of ^{226}Ra, the target diameter would be about 5.1 cm. If the maximum permissible temperature rise were 50 K, this would limit the absorbed beam power to no more than 0.635 kW, with a total incident beam power of 1.27 kW. The ^{225}Ac saturation activity in this example is 6.6 Ci, which is still quite compelling, but is considerably less than the 150 Ci activity predicted without regard to thermal constraints.

^{232}Th(p,4n)^{229}Pa Pathway

The motivation behind pursuing this pathway is to produce ^{229}Th, the 7932 year generator isotope of ^{225}Ac. ^{229}Pa has a half-life of 1.50 (5) d, and decays to ^{229}Th with a 99.52% branching ratio. There are several steps required to isolate the ^{229}Th with a high radiopurity. Due to the 1.5 day half-life of ^{229}Pa, the irradiation time time can be relatively short; ^{229}Pa would reach 75% of its saturation activity within 3 days, for example. A Pa/Th chemical separation should then be performed as quickly as possible, to isolate the ^{229}Pa. The isotopes

^{228}Pa ($t_{1/2}$ = 22 (1) h), ^{230}Pa ($t_{1/2}$ = 17.4 (5) d), ^{231}Pa ($t_{1/2} = 3.276 \times 10^4$ (11) y) and ^{232}Pa ($t_{1/2}$ = 1.32 (2) d) will also be significantly produced, depending on the incident energy, and will be present in the separated Pa solution.

Following several half-lives of ^{229}Pa decay, another Pa/Th separation should be performed, this time keeping the thorium. The reason these steps are needed are both to separate ^{229}Th from the bulk thorium target, and to eliminate any ^{231}Pa from the final ^{229}Th solution, as it is a long-lived generator of the contaminant isotope ^{227}Ac. The other short-lived protactinium isotopes will beta-decay into thorium isotopes that do not present a significant problem for the actinium radiopurity.

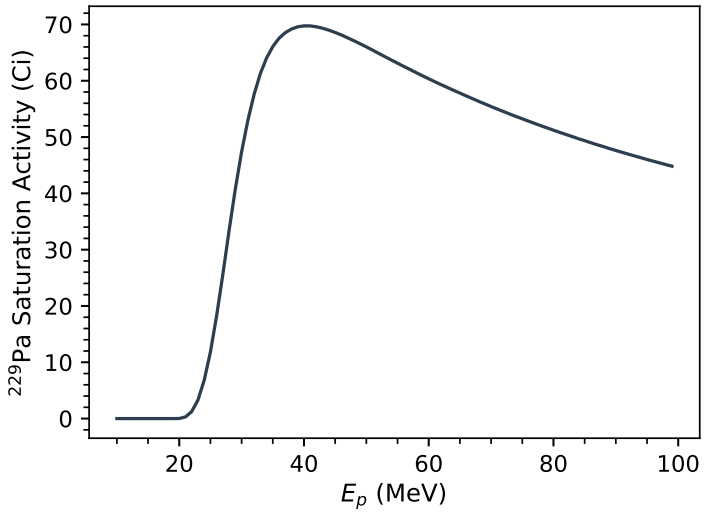

Figure 5.7: Calculated ^{229}Pa yield for the ^{232}Th(p,4n) production pathway, at a fixed beam power of 25 kW. Note that the ^{225}Ac activity will be much lower due to the long half-life of ^{229}Th.

In figure 5.6 the measurements of this channel by Jost *et al.* are compared to the 2015 TENDL evaluation [171]. The TENDL data once again needed to be multiplied by a factor of 0.4 to better reproduce the experimental data. Using the TENDL cross section, figure 5.7 shows the calculated thick target yields of ^{229}Pa. Based on this, the optimum energy for this production pathway is approximately 40 MeV. This presents an interesting opportunity for synergy between this pathway and the ^{232}Th(p,x)^{225}Ac route. Below 40 MeV, very little ^{225}Ac is directly produced in thorium. This means that the target could be split into two sections, one for the direct production of ^{225}Ac at high energy, and one for the production of ^{229}Th at lower energy.

Unfortunately, the activities of ^{225}Ac that could be extracted from the ^{229}Th generator produced by this pathway are very low. From a cost perspective, it may be preferred to use

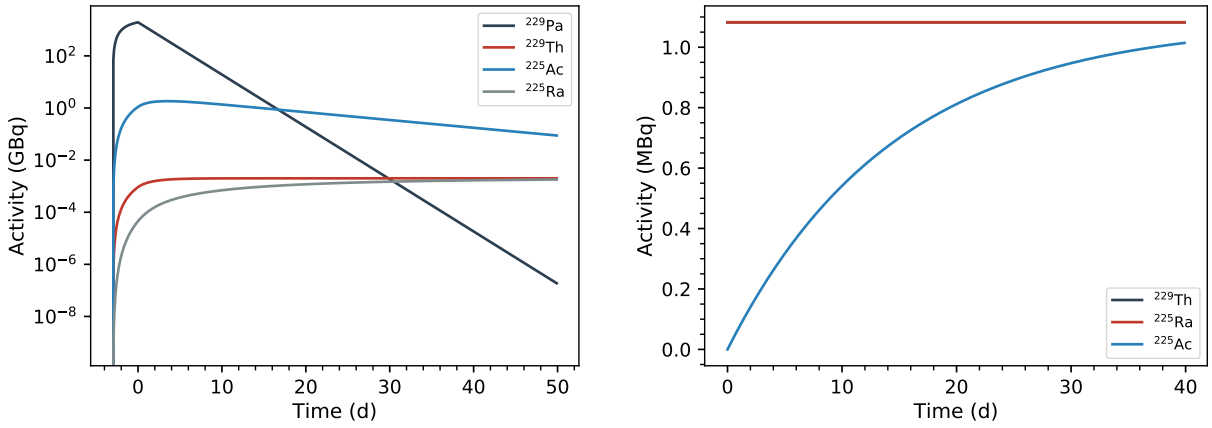

Figure 5.8: (left) Decay curve for the ^{229}Pa decay chain, following a 3 day irradiation. Only direct production of the parent isotope ^{229}Pa is included in this calculation. (right) Characteristic in-growth of ^{225}Ac from a ^{229}Th source, starting with zero ^{225}Ac activity.

the $<$ 40 MeV protons for producing other isotopes. However there is a strong argument in favor of creating a stockpile of the ^{229}Th generator, which can provide ^{225}Ac to patients even in the event of a major supply disruption, such as an accelerator shutdown.

Figure 5.8 plots the decay curves for the ^{229}Pa decay chain following a 3 day irradiation at 40 MeV and 25 kW (625 µA). On the left, it can be seen that the initial ^{229}Pa activity is very high: 52.6 Ci at end-of-bombardment (EoB). Also, note that the ^{225}Ac activity is initially higher than ^{229}Th and ^{225}Ra because it is a product of the 0.48 (5)% α-decay branch from ^{229}Pa. After a 15 day decay time (10 half-lives), essentially all of the ^{229}Pa has decayed into ^{229}Th, which will have an activity of 1.08 MBq or about 29 µCi.

As can be seen from the plot on the right of figure 5.8, this ^{229}Th stock will produce about 0.7 MBq (18.9 µCi) of ^{225}Ac after 15 days of in-growth, or about 0.95 MBq (25.6 µCi) after 30 days. This is much too low to meet the total demand for ^{225}Ac. Even though ^{225}Ac is continuously replenished after each separation, and every irradiation increases the rate at which ^{225}Ac grows in, the rate of production is much too low. It is estimated that there is currently about 150 mCi of ^{229}Th supply in the United States, and about 350 mCi globally [32]. To match even the current US supply, which itself is considered insufficient for widespread treatment, would require over 5,000 of these 3-day, 625 µA irradiations (at 40 MeV), or 41 years of continuous irradiation. Over that same time period, the approximately 428 kg of ^{233}U stored in Oak Ridge National Lab's Building 3019 will have produced about 16 Ci of ^{229}Th through natural decay [172].

5.3 Secondary Particle Production Pathways

In an isotope production pathway based on secondary particles, the purpose of the primary charged-particle beam (from the accelerator) is not to directly transmute the target into the isotope of interest. Rather, the goal is to convert it into another, secondary particle, such as a photon or neutron, that then reacts with a separate target to produce the isotope. While the secondary particle beam will have a reduced intensity compared to the primary beam, there are two main advantages to this approach. In the MeV energy range relevant to isotope production, both neutrons and photons will have a mean path length through the target that is much longer than a charged particle of an equivalent energy. This means larger sample masses can be utilized, corresponding to higher net production rates. Additionally, there may be situations in which the production cross sections of the secondary particle pathways are higher than for the direct pathways, particularly for neutron reactions which can peak at over 2000 mb for reactions like (n,2n). Additionally, both photons and neutrons will have a much lower heat deposition rate in the production target than charged particles, which is important for materials that are either sensitive to heat or which are poor conductors, such as radium salt targets.

The main drawback to the secondary particle approach is the reduced intensity, and average energy of the secondary particle field compared to the incident beam. There may also be challenges with shielding high-energy photons or neutrons, both of which typically lead to an intense field of thermal neutrons that could activate components in the accelerator facility, or more importantly, induce adverse reactions in the target.

Designing the geometry of the production target is also more complex with secondary particle pathways. Direct production pathways generally have a well collimated beam, for which it is relatively straightforward to calculate the energy and angle distributions in the target. Secondary particle pathways, on the other hand, have flux distributions with a strong angular dependence. A simple cylindrical target may not be the most optimal geometry. Also, if the secondary pathway makes use of a large target, which is advantageous from a total yield perspective, scattering and attenuation within the target must be accounted for. Because of this, understanding the secondary particle source distribution is very important to optimizing and accurately predicting the yields for these pathways.

The two secondary particle pathways for ^{225}Ac production that were considered in this comparison were ^{226}Ra(n,2n)^{225}Ra and ^{226}Ra(γ,n)^{225}Ra. The neutron source chosen for the (n,2n) pathway was thick target deuteron breakup, because it was found to have a much higher intensity than other sources in the appropriate energy region (6–20 MeV). The photon source chosen for the (γ,n) pathway was thick target Bremsstrahlung. While there are more intense photon sources, making use of exotic techniques such as inverse Compton-scattering of free-electron laser pulses [173], Bremsstrahlung photon sources are much more

commonplace and still suitable to the application.

The model for the neutron yields from thick target deuteron breakup has been described extensively in chapter 3. Because the measurements and modeling were mostly focused on a beryllium target, that is the target material used in the simulations performed for this comparison. However to attain the highest neutron, and consequently ^{225}Ac yields, a liquid lithium target would be a better choice for a large scale production facility. The calculation method for the thick target Bremsstrahlung spectra was mostly derived from the work of Mordasov *et al.* [174], but with with some modifications taken from other authors to better reproduce experimentally determined photon spectra.

Calculating Thick Target Bremsstrahlung Yields

Bremsstrahlung, derived from the German "bremsen" (to brake) and "stráhlung" (radiation), is an electromagnetic process which causes electrons to emit photons as they are decelerated in a material. While the elementary spectrum of photons emitted by an electron decelerating parallel to its direction of motion is relatively straightforward to derive from classical electromagnetism, there are a number of factors complicating the calculation of this spectrum for a thick target.

The first to consider is the angular distribution of electrons in the target. While most electrons will only undergo small angle deflections, because they can scatter off of other electrons very wide angle deflections are possible. The angular distribution will also broaden as the electrons traverse the target, so the resulting photon spectrum cannot simply be assumed to be cumulative with increasing electron energy, as was the case with deuteron breakup. The other main complication is that the electrons are traversing screened Coulomb potentials. Because the "exact" solution to the Dirac equation for electrons traversing a screened Coulomb potential requires the wavefunction be represented by an infinite series, the bremsstrahlung cross section cannot be analytically calculated [175]. Instead, there are a number of approximations and semi-empirical formulas for this cross section. Unfortunately, there is no "universal" formulation, and each approximation generally has a limited range of energies and targets for which it is valid. Many of these semi-empirical cross section formulations have been compiled in the work of Koch and Motz [175], and were used for the bremsstrahlung calculations in this comparison.

Temporarily neglecting the effects of angular straggling, the general formula for calculating thick target photon yields from a given bremsstrahlung cross section $\frac{d^2\sigma(\kappa_e,\theta)}{d\Omega dE_\gamma}$ is determined by the following integral:

$$\frac{d^2Y(E_\gamma,T_e,\theta)}{dE_\gamma,d\Omega} = \frac{\rho_N}{e}\int_0^{T_e}\tau(\kappa_e)\eta(E_\gamma)\frac{d^2\sigma(\kappa_e,\theta)}{d\Omega dE_\gamma}\Big(\frac{d\kappa_e}{dx}\Big)^{-1}d\kappa_e$$

where the variables T_e, E_γ and θ are the incident electron energy, and the outgoing γ-ray energy and angle, respectively. $\tau(\kappa_e)$ is the probability for the incident electron to be transmitted to an energy κ_e. $\eta(E_\gamma)$ is the probability for a photon of energy E_γ to be transmitted through the remainder of the target thickness. $\rho_N = \frac{\rho \cdot N_A}{M}$ is the number density of the target, e is the electron charge, and $\frac{d\kappa_e}{dx}$ is the electron stopping power in the target. Also, these photon yields are usually given in units of photons/(μC·MeV·Sr).

To numerically implement this solution, we make the following substitutions. The thick target of total thickness D is split into N sections of equal thickness Δd. Mordasov *et al.* [174] suggested the following relation for the elementary layer thickness Δd, applicable to a wide range of targets and incident electron energies

$$\Delta d = X_0 \cdot \frac{(Z+10)(T_e+10)}{84 \times 10^4 \text{ (MeV)}}$$

where X_0 is the characteristic radiation length of photons, given by the empirical relation

$$X_0 = \frac{1433}{\rho} \cdot \frac{A}{Z(Z+1) \cdot \Big(11.319 - \ln(z)\Big)} \text{ (cm)}$$

with the units of ρ in g/cm^3.

Additionally, as the bremsstrahlung cross sections we will be using from Koch and Motz [175] (derived from the earlier work of Schiff, Bethe and Heitler [176–178]) are only energy differential cross sections, we will split the double-differential cross sections into separate energy and angle components:

$$\frac{d^2\sigma(\kappa_e, \theta)}{d\Omega dE_\gamma} = \frac{d\sigma(\kappa_e)}{dE_\gamma} \cdot \frac{1}{4\pi} P(\theta, \kappa_e)$$

This gives us the following numerical expression for the thick target yields

$$\frac{d^2Y(E_\gamma, T_e, \theta)}{dE_\gamma, d\Omega} = \frac{\rho_N}{4\pi} \frac{1}{e} \sum_{i=0}^{N} \tau(\kappa_i)\eta(E_\gamma)\frac{d\sigma(\kappa_i)}{dE_\gamma} P(\theta, \kappa_i)\Delta d_{i,eff}$$

Note that Δd has been substituted for $\Delta d_{i,eff}$ in order to account for the effective thickness covered by the electron beam going through an average straggling angle θ_e, due to multiple scattering in the target material. Mordasov gives this the following empirical formula [174]

$$\Delta d_{i,eff} = \frac{\Delta d}{\cos\Big(\sqrt{1.5 \cdot \theta_{e,i}^2}\Big)}$$

The average electron angle θ_e was taken from Molière's theory of multiple scattering [179] to be

$$\theta_e^2 = -\frac{1.02\sqrt{d}}{\kappa_i + 2\mu_e} \cdot \mathbb{R}\Big(\mathcal{W}(e^{-b})\Big),$$
$$e^b = (6680 \cdot d/\beta^2) \cdot \frac{(Z+1) \cdot Z^{1/3}}{A \cdot (1 + 3.34 \cdot (1/137)^2)}$$

where μ_e is the electron rest mass energy $m_e c^2$ in units of MeV, $\mathcal{W}$ is Lambert's $\mathcal{W}$ function, $d = \rho \cdot \sum_0^i \Delta d$ is the thickness of the target traversed by the electron at energy κ_i, in units of g/cm^2, and the parameter β^2 is given by

$$\beta^2 = 1 - \Big((2 + \frac{\kappa_i}{\mu_e})^2\Big)^{-1}$$

The electron energy in the i'th layer, κ_i is determined by

$$\kappa_i = \kappa_{i-1} - \Delta d_{i-1,eff}\Big(\frac{d\kappa}{dx}(\kappa_{i-1})\Big), \quad i \geq 1$$

with $\kappa_0 = T_e$, where $\frac{d\kappa}{dx}$ is the total electron stopping power. For this work, the collisional and radiative stopping powers were taken from the formulas given by Turner [15].

The electron attenuation parameter τ represents the probability that an electron of incident energy T_e will be transmitted to a particular energy κ_i. It can also be represented in terms of the traversed thickness d_i. Figure 5.9 shows the dependence of this parameter on the energy loss, and equivalently the target thickness, for various incident electron energies on a tungsten target. The general behavior is that the electron beam is significantly attenuated: at the point the electron beam is at half its incident energy the beam has been attenuated by approximately 60%. This is very different from the systematic behavior of deuteron breakup, where most of the beam current is transmitted down to zero energy. The result of this is that bremsstrahlung yields are not cumulative, as the neutron yields from deuteron breakup were.

The parameterization for this attenuation parameter was taken from the work of Tabata and Ito [180], and is expressed by the following relation

$$\tau(T_e, d_i) = \frac{1 + \exp(-S_0)}{1 + \exp\Big((S_0 + 2) \cdot \frac{d_i}{R_{ex}} - S_0\Big)}$$

where d_i is in units of g/cm^2. The parameter S_0 is given by

$$S_0 = \frac{10.63}{Z^{0.232}} \cdot \exp\Big(0.22 \cdot Z^{0.462} \cdot \Big(1 + 0.042 \cdot E_0^{1.86}\Big)^{-1}\Big)$$

with E_0 defined as

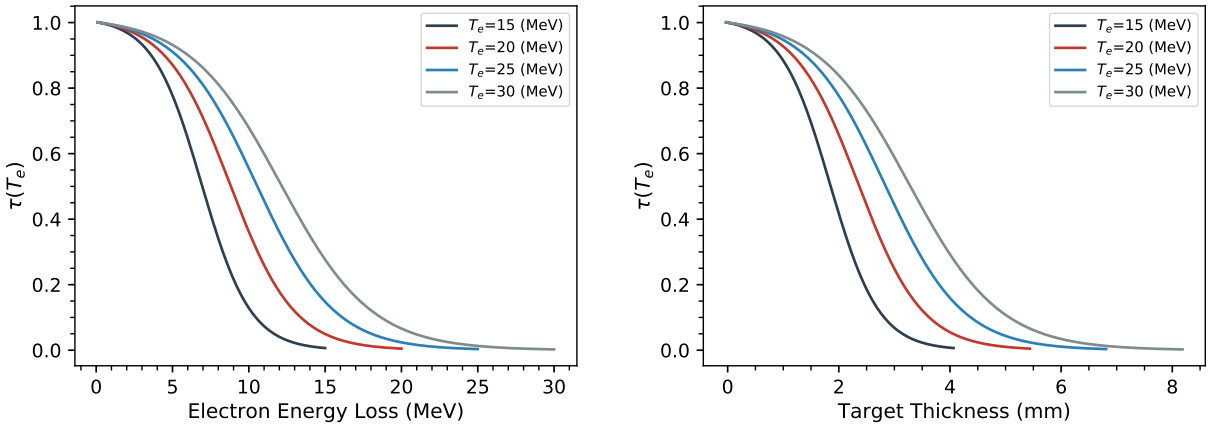

Figure 5.9: Electron attenuation parameter τ as a function of electron energy loss and tungsten target thickness, on a tungsten target.

$$E_0 = 1 + \frac{T_e}{\mu_e}$$

and where once again $\mu_e = m_e c^2$ is the electron rest mass energy, in MeV. The extrapolated electron range R_{ex} was parameterized by Tabata and Ito [180] according to the formula

$$R_{ex} = c_1 \cdot \left(\frac{\ln(1 + c_2 \cdot E_0)}{c_2} - \frac{c_3 \cdot E_0}{1 + c_4 \cdot E_0^{c_5}} \right) \ (\mathrm{g/cm^2})$$

where the constants c_n are given by

$$\begin{aligned} c_1 &= 0.2325 \cdot \frac{A}{Z^{1.209}} \\ c_2 &= 1.78 \times 10^{-4} \cdot Z \\ c_3 &= 0.9891 - 3.01 \times 10^{-4} \cdot Z \\ c_4 &= 1.468 - 0.0118 \cdot Z \\ c_5 &= \frac{1.232}{Z^{0.109}} \end{aligned}$$

For high Z materials such as tantalum or tungsten, which are common bremsstrahlung targets, the photons generated at the front of the production target may be significantly attenuated before exiting the back. The attenuation of a photon with energy E_γ, produced by an electron having traversed a thickness $d_i = \sum_0^i \Delta d$, exiting at an angle θ, will be given by

$$\eta(E_\gamma) = \exp\Big(-\mu(E_\gamma \cdot \frac{(D - d_i)}{\cos(\theta)}\Big)$$

where D is the total thickness of the target, and μ is the photon attenuation coefficient. For this study, these attenuation coefficients were interpolated from the NIST database of x-ray mass attenuation coefficients [60]. The effect of this attenuation is largest in the low energy portion of the photon spectrum.

The energy differential cross sections for bremsstrahlung were taken from the compilation of empirical formulas given by Koch and Motz [175]. The exact form is dependent on the screening parameter γ, which is dependent on the electron and outgoing photon energies, as well as the atomic number of the target, according to the relation

$$\gamma = \frac{100\mu_e \cdot E_\gamma}{E \cdot E_0 \cdot Z^{1/3}}$$

where $E = \kappa_i + \mu_e - E_\gamma$, and $E_0 = \kappa_i + \mu_e$.

The cross section formulas given by [175] are as follows

$$\frac{d\sigma(\kappa_i)}{dE_\gamma} = \frac{2Z^2 \cdot r_e^2}{137E_\gamma} \cdot \begin{cases} \Big((1 + \epsilon^2 - \frac{2}{3}\epsilon) \cdot \ln(\frac{183}{Z^{1/3}}) + \frac{\epsilon}{9}\Big), & \text{if } \gamma = 0 \\ \Big((1 + \epsilon^2) \cdot (\frac{1}{4}\phi_1 - \frac{\ln(Z)}{3} - \frac{2}{3}\epsilon \cdot (\frac{1}{4}\phi_2 - \frac{1}{3}\ln(Z))\Big), & \text{if } \gamma < 2 \\ (1 + \epsilon^2 - \frac{2}{3}\epsilon) \cdot \Big(\ln(2E \cdot \frac{E_0}{E_\gamma}) - \frac{1}{2} - C(\gamma)\Big), & \text{if } \gamma \geq 2 \end{cases}$$

where $\epsilon = \frac{E}{E_0}$, r_e is the classical electron radius, and the screening functions ϕ_1 and ϕ_2 are calculated as

$$\phi_1(\gamma) = 19.24 - 4.0 \cdot \ln(\gamma + \frac{2}{\gamma + 3}) - 0.12 \cdot \gamma \cdot \exp(-\frac{\gamma}{3})$$

and

$$\phi_2(\gamma) = \begin{cases} \phi_1 - 0.027 - (0.8 - \gamma)^2, & \text{if } \gamma < 0.8 \\ \phi_1(\gamma), & \text{otherwise} \end{cases}$$

The function $C(\gamma)$ is not directly specified in the literature, however it is plotted in the Koch and Motz reference. A least squares fit to the data found in figure 2 in [175] gives the following $C(\gamma)$ parameterization

$$C(\gamma) = 0.117 \cdot \exp(-\frac{\gamma}{5.84}) + \frac{1}{2} \cdot \exp(-\frac{\gamma}{1.42})$$

One notable feature of this formulation is that the cross section is proportional to the atomic number Z *squared*. Because the collisional stopping power for electrons is only proportional to Z, this means that the bremsstrahlung yields for a given incident electron energy

grow with increasing Z. This is quite different from deuteron breakup, where the yields were dominated by the deuteron range, making low Z targets preferred. Because of this dependence, the preferred "radiators" for bremsstrahlung are high Z materials. Tungsten and tantalum are commonly used target materials, as they offer a combination of high photon yield and good thermal properties.

The angular distribution of photons from thick target bremsstrahlung is generally quite forward focused, however there is a small component that extends to large angle. Figure 5.10 plots this angular distribution for a few incident electron energies on a tungsten target. The width of this distribution narrows significantly with increasing energy. For example, at 40 MeV incident electron energy, the angle at which the intensity reaches one half of the forward intensity is about 4°.

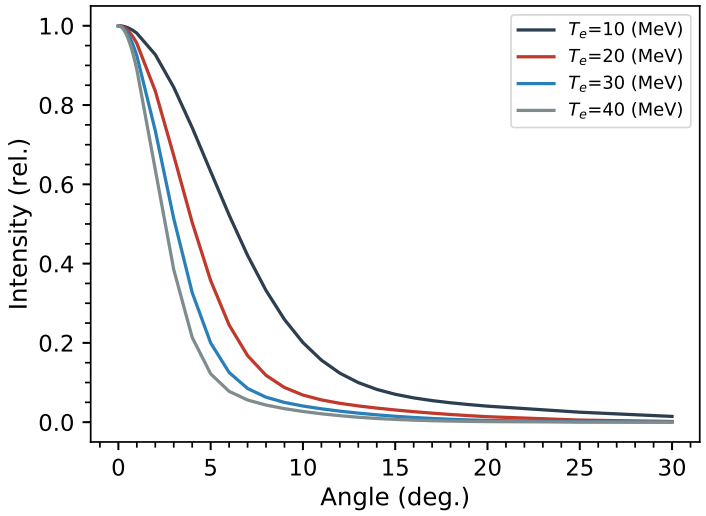

Figure 5.10: Relative angular distribution of Bremsstrahlung photons, for multiple incident electron energies on a tungsten target.

The empirical formula for this distribution was taken from the derivation by Ferdinande [181], and is given as a function of electron energy κ_i by

$$P(\theta, \kappa_i) = \left(\frac{1}{1.1} e^{-\theta^2/\theta_b^2} + \frac{0.1}{1.1} e^{-0.1\cdot\theta^2/\theta_b^2}\right) \cdot \left(\frac{11\theta_b^2 + 2\theta_e^2}{10(\theta_b^2)^2 + 11(\theta_b^2 \cdot \theta_e^2) + (\theta_e^2)^2}\right)$$

where the characteristic angle of photon emission from bremsstrahlung is given by

$$\theta_b = \begin{cases} \frac{\mu_e}{\kappa_i + \mu_e}, & \text{if } \kappa_i < 5 \\ \left(\frac{\epsilon}{4} + g_Z\right) \cdot \left(\frac{\ln(\kappa_i/\mu_e + 1)}{\kappa_i/\mu_e + 1}\right), & \text{otherwise} \end{cases}$$

with the factor g_Z parameterized as

$$g_Z = 0.5046 + 7.49 \times 10^{-4} \cdot Z - 1.78 \times 10^{-6} \cdot Z^2$$

Finally, this model was compared to available literature data for thick target bremsstrahlung photon yields. The data from the work of O'Dell [182] was selected for this evaluation for two reasons. One is that it encompasses a wide selection of incident electron energies, which is useful to highlight any systematic deficiencies of the model as a function of the beam energy. The other is that the O'Dell data is given in the correct units for total photon yield, which will be essential for accurately comparing isotope production yields to neutrons from deuteron breakup. While it would have been preferred to have a data set which extends to higher incident electron energies, none were found with the correct units of photon yield. This is perhaps not surprising, as most commercial bremsstrahlung machines (usually for radiation cancer therapy) operate under 20 MeV electron energy.

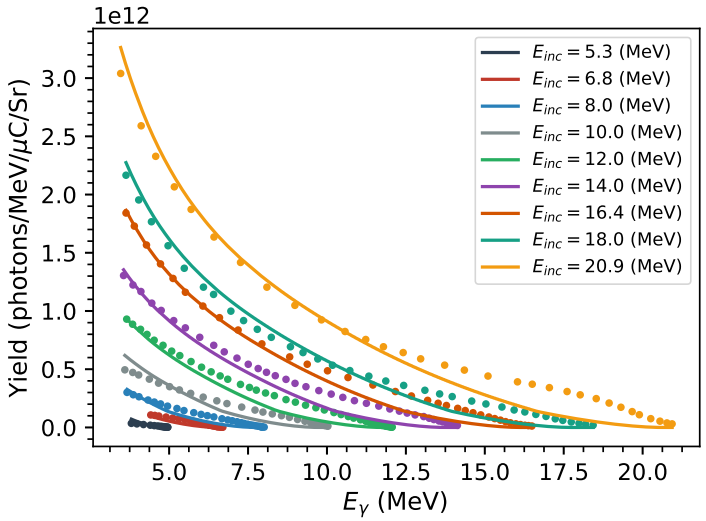

Figure 5.11: Comparison of predicted Bremsstrahlung photon spectra (lines) to experimental data from O'Dell (points) measured on a gold+tungsten target.

Figure 5.11 shows the results of the comparison to the work of O'Dell. There were not any systematic disagreements associated with the incident electron energy, which builds confidence in the capability of this model to extrapolate to higher beam energies. Also, the model generally predicted the total integrated photon fluence and the average photon energy within 25% of the experimental values. However there does seem to be a systematic disagreement between the model and the O'Dell data at photon energies close to the incident electron energy. This discrepancy has been acknowledged by other authors as common to

many thick target bremsstrahlung models [183]. Fortunately, because the majority of the (γ,n) cross section is typically in the 10–15 MeV range, and because the cross section is very wide, this high-energy discrepancy does not have too great an impact on the predicted yields. For example, at 20.9 MeV, the net modeled photon yields are under-predicted (relative to O'Dell) by 6.2%, whereas the ^{226}Ra(γ,n) reaction rate using the modeled spectrum is under-predicted by 8.2%, which means that only a 2% difference is attributable to the discrepant flux shape.

Numerical Implementation

We have now demonstrated successful models for the yields of both thick target bremsstrahlung and deuteron breakup, and evaluated them against experimental data. Because both models are expressed as double-differential yields that are parameterized in terms of the outgoing energy and angle of the respective secondary particle, we can apply the same calculation method to each yield equation.

The production rate of a given isotope is generally determined by integrating over the product of the flux distribution $\frac{d\phi}{dE}$ and the reaction cross section $\sigma(E)$, according to the equation $R = n \int_E \sigma(E) \frac{d\phi}{dE} dE$, where n is the total number of target atoms. This is making the assumption of a uniform flux distribution across a thin target.

However both deuteron breakup and bremsstrahlung have highly non-uniform emission spectra, and we would like to extend this calculation to thick targets. Additionally, we would like to consider the case of an incident (deuteron or electron) beam that has a non-uniform spatial distribution. To do this, the equation for the reaction rate must also be integrated over the coordinate spaces for the incident beam, $\vec{r}_b$, and the target, $\hat{\Omega}$. The flux attenuation in the target must also be accounted for by multiplying the flux by $\exp(-\Delta x \cdot \Sigma_t)$, where Δx is the total thickness traversed by the secondary particle, and Σ_t is the (total) attenuation cross section, which is usually designated μ for photons.

The resulting equation for the production rate is given by

$$R = n \int_{\vec{r}_b} \frac{dI(\vec{r}_b)}{d\vec{r}_b} \int_{\hat{\Omega}} \Big(\frac{1}{r_s(\hat{\Omega}, \vec{r}_b)} \Big)^2 \int_{E_o} \sigma(E_o) \frac{d^2Y(E_{inc}, E_o, \theta)}{dE_o d\Omega} \cdot \exp(-\Delta x \cdot \Sigma_t) \; dE_o d\hat{\Omega} d\vec{r}_b$$

where $\frac{dI(\vec{r}_b)}{d\vec{r}_b}$ is the spatial distribution of the incident beam intensity, r_s is the distance from the beam position vector $\vec{r}_b$ to the sample position vector $\hat{\Omega}$, E_{inc} is the incident energy of the electron or deuteron beam, and E_o is the energy of the secondary particle (photon or neutron).

This integration was calculated numerically by dividing the source and sample into finite volumes in cylindrical coordinates. For both the source and sample, the azimuthal variable

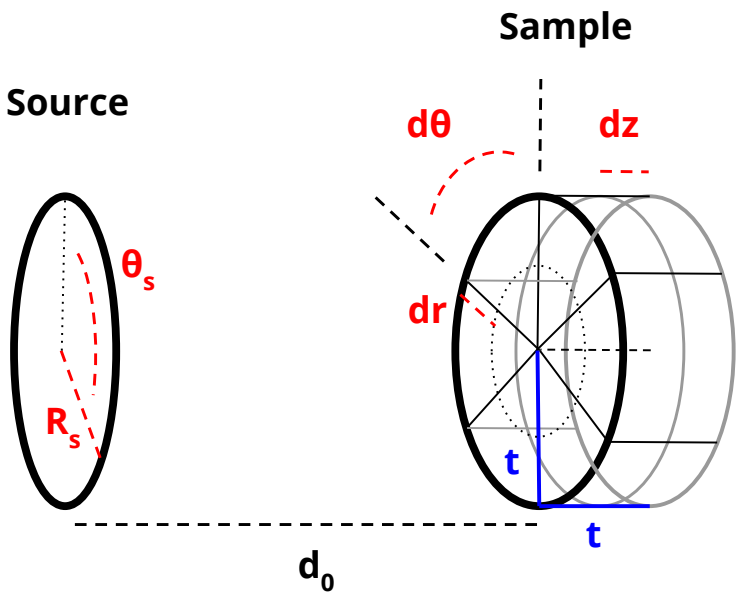

Figure 5.12: Schematic representation of variables used in the calculation of ^{225}Ra yields from both Bremsstrahlung and deuteron breakup sources.

was divided into 25 sections. The source radial distribution was divided into 20 sections, and the sample radial and axial variables were divided into 1 mm thick sections, or 5 sections, whichever was smaller.

A diagram showing this method for the production scenario used in this comparison is given in figure 5.12. One simplifying assumption that can be seen in this figure is that the source neutrons or photons were produced at the sources surface, rather than in the volume, for computational simplicity. This affects the relative solid angle for each differential source element, which could slightly bias the comparison in favor of deutron breakup as the bremsstrahlung targets will be generally thinner than breakup targets at the same beam energy. However, as long as the (conversion) target thickness is sufficiently less than the distance between the source and sample, plus the sample thickness, this effect will be small.

Based on inspiration from the work of Diamond and Ross [42], the beam profile was chosen to have a (azimuthally uniform) Gaussian radial distribution, with a nominal width of 2.5 mm full-width at half-maximum (FWHM). However the systematic dependence of the isotopic production rates on the width of this source distribution was evaluated in this study. Generally, smaller beams will produce a higher flux of particles. Deuteron breakup is expected to be less sensitive to the effects of the beam diameter than Bremsstrahlung, due

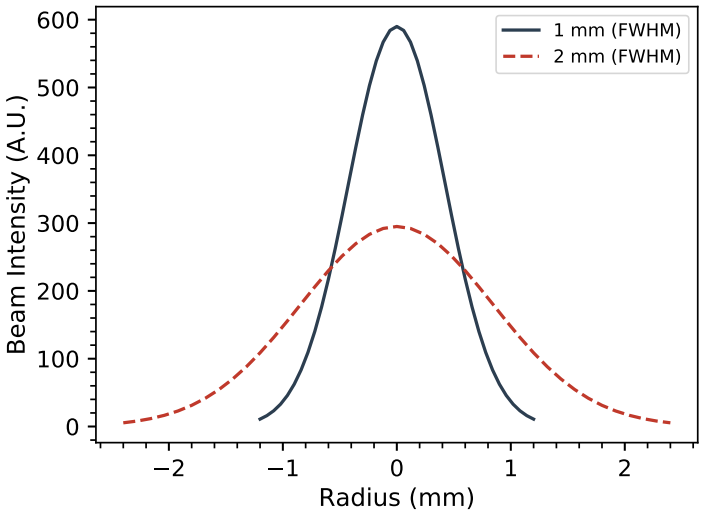

Figure 5.13: Plot of (Gaussian) radial beam intensity distribution used in the comparison.

to its relatively wider angular distribution.

There is, however, a practical limitation to how small the beam diameter can be, based on the maximum heat flux that can be safely dissipated by the target. In this comparison we will consider a tungsten bremsstrahlung target and a beryllium breakup target, both of which have high thermal conductivities (over 150 W/m·K), meaning they could both potentially withstand such a small beamspot, however this should be investigated further. Additionally, the cooling requirements for the (bremsstrahlung or breakup) target will dictate the minimum distance that the source can be from the sample. Based on the production target designs in the work of Diamond and Ross, this distance d_0 was estimated to be about 1 cm [42]. No attenuating material, such as coolant water, was simulated between the source and the sample, as this was considered too design specific. However this would certainly be a requirement for a realistic production target, which would lower the yields somewhat.

The sample was chosen to be a cylinder, for computational simplicity. Based on the double-differential spectra from both sources, this may not necessarily be the most optimal target geometry, and warrants further study. The cylinder was specified to have equal thickness and radius t, which scaled with the target mass m according to

$$t = \frac{m}{\sqrt[3]{\pi\rho}}$$

This was chosen to balance two competing effects that the sample geometry has on the production rates. Increasing the radius of the sample will increase the average source-to-sample angle, which decreases the secondary particle flux for deuteron breakup and par-

ticularly for bremsstrahlung. Increasing the thickness, however, increases the Δx through which the secondary particle beam is attenuated, which also decreases the production rate. Proportionally increasing t with the sample mass was therefore a good compromise between these two negative effects.

Results

There are several parameters which may impact the isotope production yields for the secondary particle pathways. Similar to the direct pathways, the energy of the incident beam will have a significant impact. This directly affects the energy and intensity of the secondary particle distribution. The energy distribution of the secondary particle distribution impacts the reaction cross section, and the rate of attenuation in the target. However unlike the direct pathways, which have a maximum cumulative yield which is based on the total range of the incident charged particle, uncharged secondary particles do not have a "range" in the same respect, and the target mass can be scaled to increase the yield. We don't expect this relationship to be linear, as the beam will be increasingly attenuated as the target mass increases, but we would like to examine this relationship in this study.

The other parameters affecting the isotope production yields concern the geometry of the sample. The thicker the target, the more attenuation occurs. Also the relative solid angle of the target to the beam impacts the yield; for example decreasing the beam diameter will have a similar effect as increasing the sample radius. And finally the distance between the source and the sample impact the geometric $(1/r^2)$ losses in the flux. In this study, we will examine the impact of the incident beam radius, as well as the impact of the target thickness on these two production pathways.

In order to accurately predict isotope production yields, it is essential to have a good understanding of the underlying reaction cross sections. For the (n,2n) pathway, we have performed two measurements of this cross section, averaged over a deuteron breakup spectrum at 33 and 40 MeV incident energies (about 15 and 17 MeV neutron energies). These results were presented in chapter 4, and it was shown that the TENDL evaluation reproduced these average cross sections slightly better than the ENDF evaluation, and it also better reproduced the singular literature measurement by O'Connor at 14 MeV [149]. We will therefore use the TENDL-2015 cross section for the ^{226}Ra(n,2n) reaction in this comparison.

Unfortunately for the bremsstrahlung route, there are no published measurements of the ^{226}Ra(γ,n) cross section. There was a measurement by Melville [40] of total ^{225}Ra yields, from a 10 mg radium needle irradiated in an 18 MeV bremsstrahlung spectrum. However the reported yields for the ^{225}Ra activity were based on fitting a single channel in a γ-ray spectrum at 40 keV, which was atop a very large Compton background from the 10 mg radium target. The result of this was an unacceptably large systematic uncertainty for this

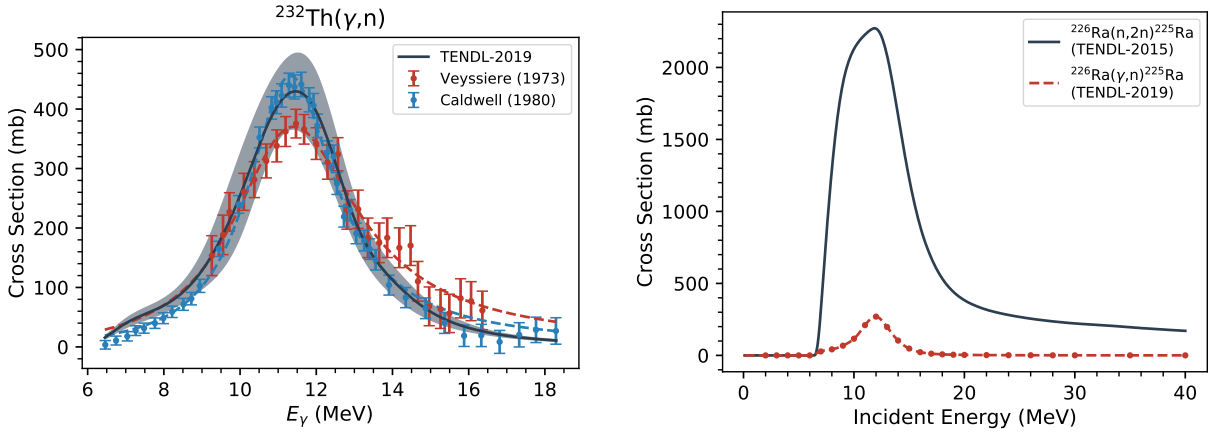

Figure 5.14: (left) Comparison of TENDL (γ,n) evaluated cross sections on a ^{232}Th target to literature measurements. (right) Comparison of ^{225}Ra production cross sections via the (n,2n) and (γ,n) pathways on ^{226}Ra.

measurement: the reported yields would correspond to a (γ,n) cross section of about 4 barns, or over 10 times the predicted value.

This is impossible to believe, as (γ,n) reactions proceed through the giant-dipole resonance (GDR). The compilation of experimental data from Berman and Dietrich [184] list a peak of 360 mb for the combined (γ,n)+(γ,pn) cross section on both ^{232}Th and ^{238}U, and 480 mb for ^{209}Bi. Even using the recent parameterization by Firestone [185], the GDR should have a total cross section of only $\sigma_T = 0.483 \cdot 226^{4/3} = 665$ (mb), and the partial cross section proceeding through (γ,n) should be less than this; usually about half, depending on the deformation of the nucleus.

The closest isotope to ^{226}Ra with measured cross sections for (γ,n) is ^{232}Th, with one measurement by Veyssiere in 1973 and another by Caldwell in 1980 [186, 187]. These cross sections are compared to TENDL-2019 in figure 5.14 [125]. The TENDL-2019 evaluation shows good agreement with the Caldwell data, and is generally within one standard deviation of Veyssiere. This provides confidence that the TENDL predictions for (γ,n) in this mass region are reasonably accurate.

The TENDL prediction for the ^{226}Ra cross section is less than for ^{232}Th, at about 270 mb peak cross section, rather than 430 mb, as can be seen in figure 5.14. This is *significantly* less than the (n,2n), which peaks at over 2200 mb. The implications of this can be seen in figure 5.15. The plot on the left shows the calculated ^{225}Ra saturation activity as a function of the (25 kW) incident beam energy, for a one gram ^{226}Ra target. Despite the bremsstrahlung source having approximately 260 times greater flux in the forward direction, the saturation activities are very similar for a 1 gram target. This is because while bremsstrahlung is very

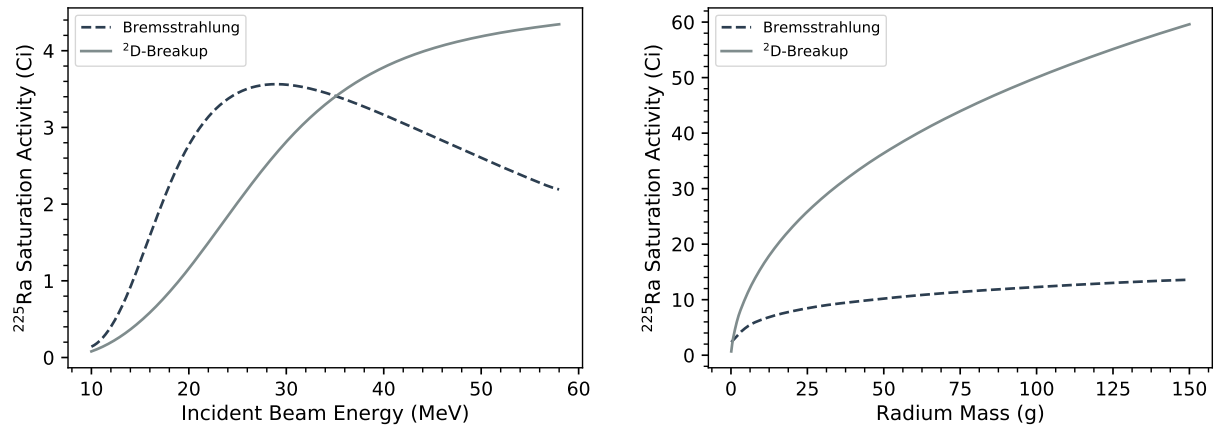

Figure 5.15: (left) Comparison of ^{225}Ra saturation activity yields from each pathway, as a function of incident energy. The simulated beam power was fixed at 25 kW, and the radium target mass was 1 g. (right) Comparison of ^{225}Ra saturation activity yields from each pathway, as a function of radium target mass. The simulated beam power was fixed at 25 kW, and the incident energy (for each) was 40 MeV.

intense, it has a spectrum with an approximately $1/E_\gamma$ shape, which means most of these photons do not contribute to the (γ,n) reaction.

The other interesting result from the comparison of the incident beam energies is that the bremsstrahlung pathway is more "efficient" at lower energy as compared to deuteron breakup, despite the cross sections for both reactions peaking at about 12 MeV. This is likely attributable to the fact that the electron beam is strongly attenuated in the target, regardless of the incident energy. This can be seen from the plots of $\tau(T_e)$ in figure 5.9, where the intensity of the incident beam reaches approximately half by the time the electron has lost half of its energy. This means that electron beams higher than about 25 MeV are essentially "wasting" their electrons, as they will be significantly attenuated by the time they are reduced to energies more appropriate for the (γ,n) reaction.

The major differentiating factor between the bremsstrahlung approach and deuteron breakup is, however, when the mass of the radium target is increased to larger than 1 gram. The plot on the right of figure 5.15 shows that as the mass is increased, the ^{225}Ra saturation activity from the deuteron breakup route far exceeds that of the bremsstrahlung. This can be attributed to two factors. The first is that radium is a high Z material, and will therefore have a high photon attenuation coefficient $\mu(E_\gamma)$. As the target thickness increases, the photon flux will decrease exponentially. The same is true of neutrons, however the attenuation coefficient (or rather, the total macroscopic cross section) will be significantly less. Furthermore, it is worth noting that approximately half of the total (n,x) reaction cross

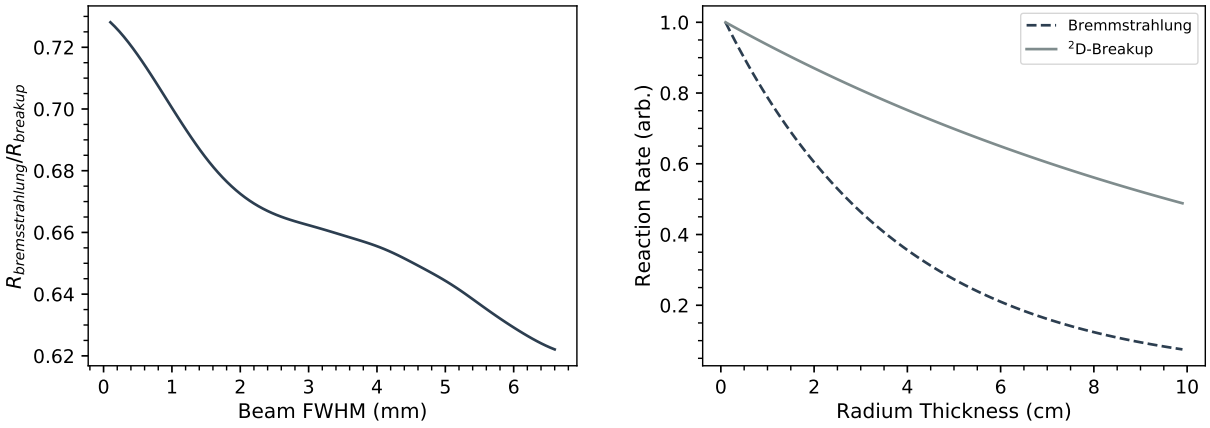

Figure 5.16: (left) Ratio of bremsstrahlung to deuteron breakup ^{225}Ra production rates, as a function of the incident beam FWHM radius. The simulated beam power was fixed at 25 kW, the incident energy (for each) was 40 MeV, and the target mass was 1 g. (right) Comparison of the attenuation in the ^{225}Ra production rate for both pathways, as a function of the radium target thickness. The incident energy used was 40 MeV.

section on ^{226}Ra is elastic scattering. Since this doesn't significantly decrease the energy of the neutrons, these scattered neutrons get a "second pass" at inducing (n,2n), if the radium target is large. This is in distinct contrast to the photons from bremsstrahlung, which on average lose almost all their energy. That being said, we have ignored any contributions from multiple neutron scattering for simplicity's sake.

The plot on the right of figure 5.16 shows how the relative reaction rate is attenuated for each pathway, with the relative reaction rate calculated according the following equation

$$R = R_0 \int_E \sigma(E)\phi(E) \cdot \exp\Big(- \Sigma_T(E) \cdot \Delta x\Big) dE$$

where Σ_T is equivalent to the attenuation coefficient μ for photons.

As the targets get larger, the solid angle of the additional material, relative to the beam, decreases. This geometric effect is the same for each target, and is one of the reasons that the saturation activity does not increase linearly with the sample mass. The other factor that differentiates the two pathways is that as the sample size increases, the average angle of emission increases, which will decrease the flux from bremsstrahlung significantly more than deuteron breakup because of how forward-focused the bremsstrahlung emissions are.

The same effect occurs by increasing the average beam width, for a fixed target size. As can be seen from a the plot on the left of figure 5.16, the bremsstrahlung production rates diminish faster than for deuteron breakup as the width of the beam is increased.

The interpretation of these results depends on a few factors. The main consideration is the assumption of a "realistic" ^{226}Ra target mass, as this has a significant implication on how bremsstrahlung performs relative to deuteron breakup, as well as how the two methods compare to the direct production routes. Because of how rare and hazardous radium targets are, this "realistic" target mass will likely be much less than the mass at which either pathway is limited by flux attenuation. The beam and sample geometry will also be important to consider. Deuteron breakup is generally more favorable over the range of geometries evaluated in this comparison. However, for example, a large-diameter, thin target placed a long distance away from the source may have different behavior.

Separation Scheme

One feature of both the (γ,n) and (n,2n) production pathways is that they produce ^{225}Ra, rather than ^{225}Ac directly. The consequence of this is that ^{225}Ac can be extracted almost completely free of the ^{227}Ac contaminant, based on a simple separation scheme.

Neither (γ,n) nor (n,2n) are expected to produce significant amounts of ^{227}Ac. For (γ,n), there is no direct pathway to ^{227}Ac, however the high energy photons could create a secondary field of neutrons from interactions with other materials in the production chamber, that would undergo a (n,γ) reaction and produce ^{227}Ra, which feeds into ^{227}Ac. Similarly, the neutrons from deuteron breakup are too high energy to induce significant (n,γ), however they could be thermalized by the environment and consequently be absorbed.

Because the half-life of ^{227}Ra, at 42.2 (5) minutes, is significantly shorter than the 14.9 (2) day ^{225}Ra activity, at the end-of-bombardment it will decay relatively quickly into ^{227}Ac before ^{225}Ac has significantly decayed in. This means that an initial actinium/radium chemical separation can be performed, and the separated actinium batch (containing the ^{227}Ac) can be disposed of.

This is depicted in figure 5.17, for a 10 day irradiation, with the initial separation depicted in blue. If the other 4 separations are performed at 18 day intervals, the total collected ^{225}Ac is about 75% of the initial ^{225}Ra activity. If there is not significant ^{227}Ra produced by (n,γ), and therefore the initial separation does not need to be thrown out, the total collected ^{225}Ac activity is about 105% that of the initial ^{225}Ra. If the actinium were to be continuously separated from the radium, the theoretical maximum of 150% of the initial ^{225}Ra activity could be obtained.

Thermal Considerations

One of the crucial differences between the bremsstrahlung production pathway and the deuteron breakup pathway is the difference in heat that is deposited in the radium target.

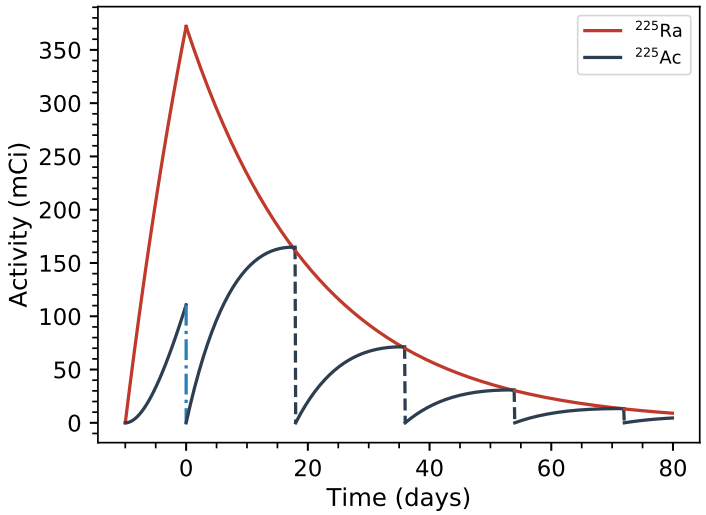

Figure 5.17: Potential ^{225}Ra/^{225}Ac separation scheme, relevant to both pathways. The blue dashed line indicates the initial separation, for which the actinium may need to be thrown out to improve the ^{225}Ac/^{227}Ac purity.

Unlike neutrons, which exclusively undergo nuclear interactions, photons primarily interact with matter by transferring energy to electrons. Because the bremsstrahlung emission spectrum has an approximately $1/E_\gamma$ shape, most of the photon flux is in the low energy portion of the spectrum, which is also the portion most likely to be absorbed in the radium target.

Let's again consider the simple 1D solution to the steady state heat equation, in which the maximum permissible beam power is determined by

$$P_{max} = \Delta u \cdot \frac{8\pi k \cdot r^2}{\eta \cdot t}$$

where we have introduced the parameter η to represent the fraction of the incident beam power that is absorbed by the radium target. This can be calculated using the NIST [60] energy-absorption coefficients μ_{en} according to

$$\eta = \frac{e}{P_{inc}} \int_{E_\gamma} \frac{dI_\gamma}{dE_\gamma} \cdot E_\gamma \cdot \Big(1 - \exp\big(-\mu_{en}(E_\gamma) \cdot \Delta x\big)\Big)\, dE_\gamma$$

where I_γ is the incident photon intensity, in photons/sec, and Δx is the target thickness.

This has been calculated for a 8.59 mm thick target, which corresponds to 10 grams of radium in a cylindrical geometry having proportions $r = t$, and has been plotted as a function of the incident beam energy in figure 5.18. This shows that the absorbed power is relatively high, ranging from about 2–4.5% over the energy range relevant to isotope production. This

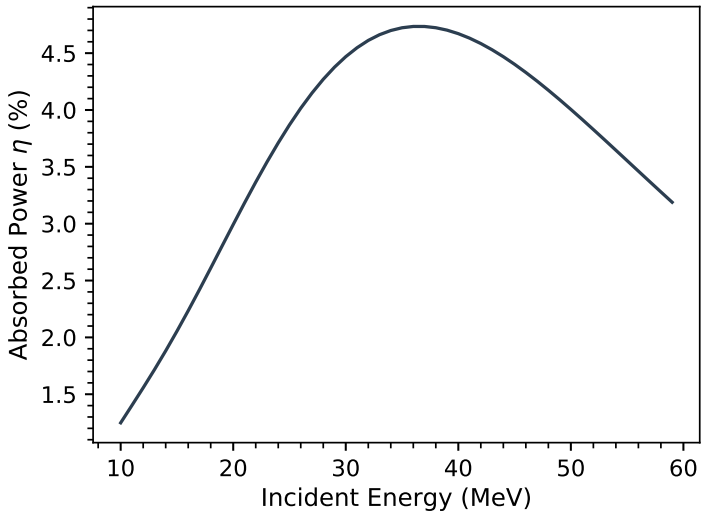

Figure 5.18: Fraction of absorbed power, η, as a function of the incident beam energy for the (γ,n) approach.

will certainly require an active cooling system, however it is not as limiting as the ^{226}Ra(p,2n) pathway, which absorbs between 50% of the incident power over the useful range of the (p,2n) cross section.

This also indicates that the optimal geometry for the bremsstrahlung pathway will depend on the limitations due to target cooling. If we were to keep the $r = t = 8.59$ mm aspect ratio for this example 10 g target, and limit the temperature rise to no more than 50 K, the maximum permissible power is only 290 W. This means that the target must be made significantly thinner (and consequently wider) in order to operate at a higher beam power, which will likely have a negative impact on the yields.

Producing Other Isotopes

One of the advantages of the secondary particle production pathways is that other targets can be simultaneously irradiated, creating multiple isotopes for other applications. This is particularly true for the deuteron breakup source, as the fast neutrons from breakup will not be significantly attenuated by even a modestly sized target. Additionally, while almost all 90% of the bremsstrahlung intensity is in the first 5–10°, many neutrons from deuteron breakup are emitted at larger angles. Because these large angle neutrons are primarily emitted from compound-evaporation processes, the average energy will be lower, which may be more suitable for some applications.

Figure 5.19 shows a comparison of the bremsstrahlung and deuteron breakup production

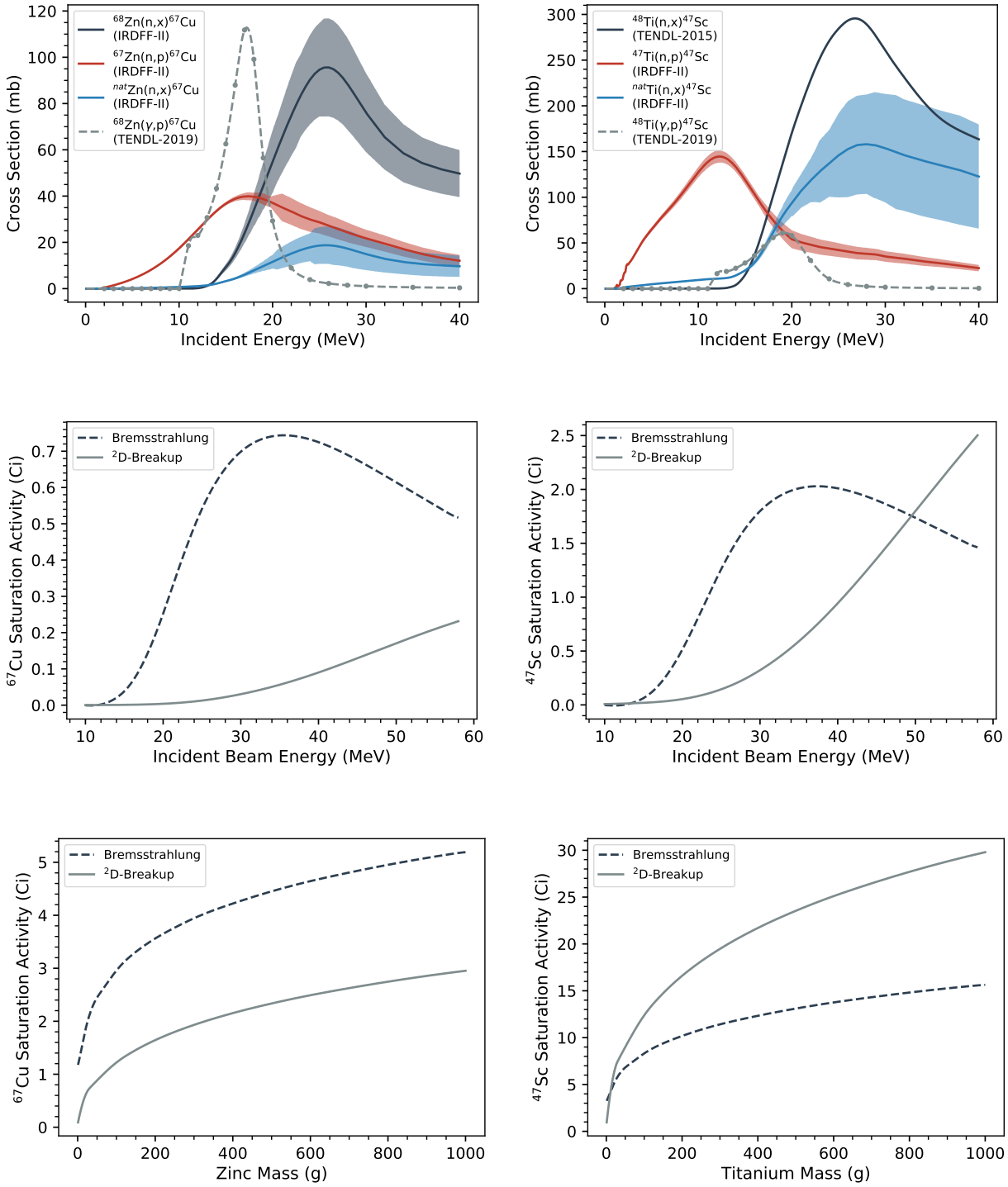

Figure 5.19: Comparison between bremsstrahlung and deuteron breakup for the production of ^{67}Cu and ^{47}Sc using natural zinc and titanium targets, respectively. (top) Comparison of (n,x) and (γ,p) cross sections on these targets. (middle) Comparison of the ^{67}Cu and ^{47}Sc saturation activities as a function of incident beam energy. (bottom) Comparison of the ^{67}Cu and ^{47}Sc saturation activities as a function of the mass of the natural targets.

rates for the therapeutic β^--emitting ^{67}Cu and ^{47}Sc isotopes, produced from natural zinc and titanium targets, respectively. These isotopes are considered challenging to produce, as the only proton production routes require high energy beams on gallium and vanadium targets. The calculation method in this comparison was exactly the same as described in the section on ^{225}Ac production, except that the target mass range was substantially larger because of the relative ease of obtaining natural zinc and titanium targets.

For the photo-nuclear pathways, the only reactions producing the isotope of interest were (γ,p) on ^{68}Zn and ^{48}Ti, for the production of ^{67}Cu and ^{47}Sc respectively. Both of these isotopes are reasonably abundant, so enriching the targets to increase the yields may not be economically worthwhile. For the neutron pathways, the largest cross sections are for the (n,np) reactions on the same target isotopes, so they would also not likely see any advantage for enriched targets.

In general, the systematic behaviors of these pathways are quite similar to ^{225}Ra production, except that the photon flux is not as significantly attenuated as for ^{226}Ra due to these targets being lower Z. The major difference is in the reaction cross sections. While photo-nuclear cross sections do not vary extremely for different isotopes, the neutron cross sections do. ^{68}Zn(n,np)^{67}Cu and ^{67}Zn(n,p)^{67}Cu in particular are quite small relative to the other neutron cross sections. This leads to the bremsstrahlung pathway outperforming deuteron breakup for the production of ^{67}Cu, regardless of the target mass or incident energy. However for the ^{47}Sc production, the opposite is the case. The (γ,p) cross section is not significantly different, however the (n,p) and (n,np) cross sections are almost three times what they were for Zn.

5.4 Conclusions

In this chapter, we have compared the predicted yields for several ^{225}Ac production pathways, which are all generally quite unique from one another. The ^{232}Th(p,x) production pathway requires a very high energy proton accelerator to be viable, but can produce high yields and does not suffer from the thermal or targetry constraints of the pathways based on a radium target. However the long term impacts of the ^{227}Ac impurity produced in this approach still need to be seen. The ^{226}Ra(p,2n) pathway initially appeared to have even higher yields, however it was shown that the thermal design constraints will likely impede this route significantly. The ^{232}Th(p,4n)^{229}Th pathway was the only one considered which produced the long-lived ^{229}Th generator for ^{225}Ac, but the total yields are likely too low to be of significant value.

Thick target bremsstrahlung and deuteron breakup sources were compared for the production of ^{225}Ra via the (γ,n) and (n,2n) reactions, respectively. The results of this comparison

depend significantly on the mass of radium to be irradiated. At one gram, the two pathways are roughly comparable. However at larger masses, the deuteron breakup pathway significantly out-performs bremsstrahlung. The opposite was shown to be the case, however, for ^{67}Cu production from natural zinc targets. This was a demonstration of how important the production cross sections are to the radioisotope yields. There was also a general trend of bremsstrahlung performing best at around 25–30 MeV incident electron energy, whereas the deuteron pathways showed the highest yield at over 50 MeV. This difference was attributed to the attenuation parameter τ, which is generally much higher for electrons than for deuterons. Also, the thermal limitations for the bremsstrahlung pathway were shown to be quite impactful on its scaling, as the low energy photons produced by this process have a high rate of absorption in radium.

Ultimately, what this comparison serves to show is how complex and nuanced the considerations are when optimizing a production pathway, or attempting to determine a "best" approach. There are many uncertainties that must be addressed in order to make this determination. For example, how much radium mass is considered "practical"? What ^{225}Ac/^{227}Ac radiopurity is acceptable for human use? Are there other radium compounds with better thermal conductivity? Even if these and other questions are answered, the engineering constraints surrounding each pathway are unique, and may impose unforeseen limitations. However it is the hope that this comparison will be useful in determining the right questions to ask, and in investigating what these limitations might be, so that these pathways can move forward in meeting the demand for the very exciting and promising isotope: ^{225}Ac.

Chapter 6

Conclusions

In this work, we have demonstrated the potential viability of a new pathway for ^{225}Ac production, which makes use of deuteron breakup as a high intensity, variable energy neutron source for which to produce ^{225}Ra, the parent isotope of ^{225}Ac, through the ^{226}Ra(n,2n) reaction. To support this, a hybrid model for the double-differential neutron spectrum from deuteron breakup was developed based on the work of Serber and Kalbach, and additional measurements of the neutron distribution from breakup on at thick beryllium target were performed for 33 and 40 MeV incident deuteron energies. The ^{226}Ra(n,2n) reaction cross section was also experimentally determined, averaged over the breakup spectra from 33 and 40 MeV deuterons, which was in relatively close agreement with the TENDL evaluation [125]. A comparison study of several promising ^{225}Ac production pathways was performed, showing that the ^{226}Ra(n,2n) route had comparable yields to the well-studied ^{232}Th(p,x)^{225}Ac pathway at the same beam power, so long as the radium target mass was in the 10–50 gram range, but with the added benefit of being free from ^{227}Ac contamination. The production routes based on irradiation of ^{226}Ra with photons or charged particle beams were shown to have thermal limitations, which could potentially be overcome with sophisticated cooling systems, or new radium target compounds such as RaB_6.

In addition, new measurements of the ^{139}La(p,6n) reaction were presented as a pathway for the production of ^{134}Ce, an *in vivo* generator of ^{134}La, which together act as a positron-emitting chemical analog for ^{225}Ac. Because ^{225}Ac does not emit positrons as part of its decay chain, ^{134}Ce could be used instead to provide a rapid biodistribution assay via positron emission tomography (PET). Additionally, several other ^{139}La(p,x) reaction cross sections were measured over the 35–60 MeV energy range, which serve a useful role in understanding the nuclear reaction mechanisms present at these energies.

It is the hope that this characterization of deuteron breakup and the demonstration of its use in ^{225}Ac production will result in a more widespread adoption of this technology,

both for isotope production, as well as the many scientific and industrial applications of an intense source of energetic neutrons. Fast neutron reactions in the 10's of MeV range have a unique position within the scope of isotope production, with the ability for (n,xn), (n,p) and (n,α) reactions to produce certain products that are virtually inaccessible to charged particle beams or nuclear reactors. This work has shown that deuteron breakup is an ideal neutron source for many of these pathways, and is a potentially valuable addition to any isotope production portfolio.

Additionally, this work has demonstrated the value of new measurement and modeling efforts in the field of nuclear data. Specifically, it was shown that different reaction modeling codes have widely varying predictions for pre-equilibrium, and that this process is very important for isotope production applications. Furthermore, the deuteron breakup modeling work highlighted discrepancies in existing measurements of this process, which were confirmed experimentally. Also, the discrepancy between the ENDF and TENDL predictions for the ^{226}Ra(n,2n) reaction was successfully resolved by new measurements presented in this work. All of this proves that there is both a need for new measurement and modeling efforts within the field of nuclear data, and a value to be gained from the applications perspective.

Future Work

This project has touched on a wide range of disciplines, from measurement and modeling in nuclear physics, to radiochemistry, to thermal hydraulic engineering. If the final result of this work is to develop a complete system for producing and purifying ^{225}Ac, the work involved in reaching that goal must delve into these disciplines even deeper. In the field of nuclear physics, further measurements of deuteron breakup on other light target materials, such as lithium, as well as at higher energies, should be performed to improve the understanding of this process. Neutron yields for lithium targets in particular should be about 30% higher than for beryllium, which would further increase the appeal of this neutron source for applications. Additionally, work on improving the predictive power of pre-equilibrium modeling should be performed, such as the recent work by Fox *et al.* [188].

In chapter 4 we performed a very basic comparison between two radium/actinium separation mechanisms. However a much more comprehensive study of these methods, comparing the recovery and separation factors as a function of pH, as well as different rinse sequences or solutions, is required to fully optimize this separation technique. Also, while the two ^{226}Ra(n,2n) cross section measurements performed at 33 and 40 MeV deuteron energies proved to be valuable data points, measurements at additional energies would further improve the optimization of this pathway.

Finally, if this pathway is to be pursued for large scale production, various engineering challenges must be overcome. One significant omission from this work is understanding how

internal scattering within a thick radium target would impact the yields, as well as how an external reflector could be utilized to boost the neutron flux on the target even further. This could be performed using a surrogate target, such as thorium, which is likely to have similar elastic scattering properties to radium (at high energies) but which is much safer to handle on an experimental level. Additionally, a cooling system must be optimized for the breakup target that allows the radium sample to be located as close as possible to the source, thus maximizing the neutron flux.

Outlook

The curative potential for ^{225}Ac based targeted alpha therapy is very exciting, and possibly represents a paradigm change in cancer treatment towards truly personalized nuclear medicine. What has been shown in this work is that there are many potential pathways through which ^{225}Ac can be produced, and although much work remains to be done, it is very conceivable that ^{225}Ac can be produced at scales relevant to widespread use. It is the hope that the results of this work will be useful in enabling new isotope production capabilities based on deuteron breakup, and that this can support the long term growth of actinium based cancer therapies. In the comparison study of actinium production pathways, it was shown that there are many uncertainties, caveats and nuances that must be acknowledged when comparing two pathways, and the results of that work will hopefully impact future planning decisions regarding alternative production approaches. Finally, it is my hope that I can continue to play a role in advancing the production of this valuable isotope, which has the potential to improve the quality of human life for years to come.

Bibliography

[1] J. K. Liu, "The history of monoclonal antibody development–progress, remaining challenges and future innovations," *Annals of medicine and surgery*, vol. 3, no. 4, pp. 113–116, 2014.

[2] A. F. Shaughnessy, "Monoclonal antibodies: magic bullets with a hefty price tag," *Bmj*, vol. 345, 2012.

[3] B. A. Teicher and R. V. Chari, "Antibody conjugate therapeutics: challenges and potential," *Clinical cancer research*, vol. 17, no. 20, pp. 6389–6397, 2011.

[4] C. Kratochwil, F. Bruchertseifer, F. L. Giesel, M. Weis, F. A. Verburg, F. Mottaghy, K. Kopka, C. Apostolidis, U. Haberkorn, and A. Morgenstern, "225Ac-PSMA-617 for PSMA-Targeted α-Radiation Therapy of Metastatic Castration-Resistant Prostate Cancer," *Journal of Nuclear Medicine*, vol. 57, no. 12, pp. 1941–1944, 2016.

[5] M. R Zalutsky and M. Pruszynski, "Astatine-211: production and availability," *Current radiopharmaceuticals*, vol. 4, no. 3, pp. 177–185, 2011.

[6] C. N. B. Harisankar, K. Agrawal, A. Bhattacharya, and B. R. Mittal, "F-18 fluorodeoxy-glucose and F-18 sodium fluoride cocktail PET/CT scan in patients with breast cancer having equivocal bone SPECT/CT," *Indian journal of nuclear medicine: IJNM: the official journal of the Society of Nuclear Medicine, India*, vol. 29, no. 2, p. 81, 2014.

[7] A.-M. Chacko and C. R Divgi, "Radiopharmaceutical chemistry with iodine-124: a non-standard radiohalogen for positron emission tomography," *Medicinal chemistry*, vol. 7, no. 5, pp. 395–412, 2011.

[8] "Targeted Cancer Therapies Fact Sheet." Accessed: 2021-04-30.

[9] A. Morgenstern, C. Apostolidis, and F. Bruchertseifer, "Supply and Clinical Application of Actinium-225 and Bismuth-213," *Seminars in Nuclear Medicine*, vol. 50, no. 2, pp. 119–123, 2020. Targeted alpha therapy.

[10] C. Kratochwil, F. Bruchertseifer, H. Rathke, M. Bronzel, C. Apostolidis, W. Weichert, U. Haberkorn, F. L. Giesel, and A. Morgenstern, "Targeted α-Therapy of Metastatic Castration-Resistant Prostate Cancer with 225Ac-PSMA-617: Dosimetry Estimate and Empiric Dose Finding," *Journal of Nuclear Medicine*, vol. 58, no. 10, pp. 1624–1631, 2017.

[11] V. Malhotra and M. C. Perry, "Classical Chemotherapy: Mechanisms, Toxicities and the Therapeutc Window," *Cancer Biology & Therapy*, vol. 2, no. sup1, pp. 1–3, 2003.

[12] Y. Luqmani, "Mechanisms of drug resistance in cancer chemotherapy," *Medical principles and practice*, vol. 14, no. Suppl. 1, pp. 35–48, 2005.

[13] F. Buchegger, F. Perillo-Adamer, Y. M. Dupertuis, and A. B. Delaloye, "Auger radiation targeted into DNA: a therapy perspective," *European journal of nuclear medicine and molecular imaging*, vol. 33, no. 11, pp. 1352–1363, 2006.

[14] D. Bleuel, R. Donahue, B. Ludewigt, and J. Vujic, "Designing accelerator-based epithermal neutron beams for boron neutron capture therapy," *Medical physics*, vol. 25, no. 9, pp. 1725–1734, 1998.

[15] J. E. Turner, *Atoms, radiation, and radiation protection*. John Wiley & Sons, 2008.

[16] R. Mayer, M. R. Hamilton-Farrell, A. J. van der Kleij, J. Schmutz, G. Granström, Z. Sicko, Y. Melamed, U. M. Carl, K. A. Hartmann, E. C. Jansen, *et al.*, "Hyperbaric oxygen and radiotherapy," *Strahlentherapie und Onkologie*, vol. 181, no. 2, pp. 113–123, 2005.

[17] M. R. Bhat, "Evaluated nuclear structure data file (ensdf)," in *Nuclear Data for Science and Technology* (S. M. Qaim, ed.), (Berlin, Heidelberg), pp. 817–821, Springer Berlin Heidelberg, 1992.

[18] R. Abergel and L. Arnedo-Sanchez, "Challenges of actinium coordination chemistry for nuclear medicine," *Journal of Medical Imaging and Radiation Sciences*, vol. 50, no. 4, p. S111, 2019.

[19] J. Szücs, M. Johns, and B. Singh, "Nuclear data sheets for A= 149," *Nuclear Data Sheets*, vol. 46, no. 1, pp. 1–185, 1985.

[20] A. Artna-Cohen, "Nuclear data sheets for A= 211," *Nuclear Data Sheets*, vol. 63, pp. 79–138, 1991.

[21] E. Browne, "Nuclear data sheets for A= 212," *Nuclear Data Sheets*, vol. 104, no. 2, pp. 427–496, 2005.

[22] M. Basunia, "Nuclear Data Sheets for A = 213," *Nuclear Data Sheets*, vol. 108, no. 3, pp. 633 – 680, 2007.

[23] E. Browne, "Nuclear Data Sheets for A= 215,219,223,227,231," *Nuclear Data Sheets*, vol. 93, no. 4, pp. 763–1061, 2001.

[24] A. Jain, R. Raut, and J. Tuli, "Nuclear Data Sheets for A = 225," *Nuclear Data Sheets*, vol. 110, no. 6, pp. 1409 – 1472, 2009.

[25] E. Deshayes, M. Roumiguie, C. Thibault, P. Beuzeboc, F. Cachin, C. Hennequin, D. Huglo, F. Rozet, D. Kassab-Chahmi, X. Rebillard, *et al.*, "Radium 223 dichloride for prostate cancer treatment," *Drug design, development and therapy*, vol. 11, p. 2643, 2017.

[26] G. Henriksen, D. R. Fisher, J. C. Roeske, Ø. S. Bruland, and R. H. Larsen, "Targeting of osseous sites with α-emitting 223Ra: comparison with the β-emitter 89Sr in mice," *Journal of Nuclear Medicine*, vol. 44, no. 2, pp. 252–259, 2003.

[27] V. Frantellizzi, L. Cosma, G. Brunotti, A. Pani, A. Spanu, S. Nuvoli, F. De Cristofaro, L. Civitelli, and G. De Vincentis, "Targeted Alpha Therapy with Thorium-227," *Cancer biotherapy & radiopharmaceuticals*, vol. 35, no. 6, pp. 437–445, 2020.

[28] J. Dahle, T. J. Jonasdottir, H. Heyerdahl, J. M. Nesland, J. Borrebæk, A. K. Hjelmerud, and R. H. Larsen, "Assessment of long-term radiotoxicity after treatment with the low-dose-rate alpha-particle-emitting radioimmunoconjugate 227Th-rituximab," *European journal of nuclear medicine and molecular imaging*, vol. 37, no. 1, pp. 93–102, 2010.

[29] T. A. Bailey, V. Mocko, K. M. Shield, D. D. An, A. C. Akin, E. R. Birnbaum, M. Brugh, J. C. Cooley, J. W. Engle, M. E. Fassbender, *et al.*, "Developing the ^{134}Ce and ^{134}La pair as companion positron emission tomography diagnostic isotopes for ^{225}Ac and ^{227}Th radiotherapeutics," *Nature Chemistry*, vol. 13, no. 3, pp. 284–289, 2021.

[30] S. Lever, J. Lydon, C. Cutler, and S. Jurisson, "9.20 - Radioactive Metals in Imaging and Therapy," in *Comprehensive Coordination Chemistry II* (J. A. McCleverty and T. J. Meyer, eds.), pp. 883–911, Oxford: Pergamon, 2003.

[31] S. Mirzadeh, K. Kumar, and O. A. Gansow, "The chemical fate of 212Bi-DOTA formed by β-decay of 212Pb (DOTA) 2," *Radiochimica Acta*, vol. 60, no. 1, pp. 1–10, 1993.

[32] A. K. Robertson, C. F. Ramogida, P. Schaffer, and V. Radchenko, "Development of 225Ac radiopharmaceuticals: TRIUMF perspectives and experiences," *Current radiopharmaceuticals*, vol. 11, no. 3, pp. 156–172, 2018.

[33] O. Bonne, Y. Krausz, M. Gorfine, H. Karger, Y. Gelfin, B. Shapira, R. Chisin, and B. Lerer, "Cerebral hypoperfusion in medication resistant, depressed patients assessed by Tc99m HMPAO SPECT," *Journal of affective disorders*, vol. 41, no. 3, pp. 163–171, 1996.

[34] C. Müller, C. Vermeulen, U. Köster, K. Johnston, A. Türler, R. Schibli, and N. P. van der Meulen, "Alpha-PET with terbium-149: evidence and perspectives for radiotheragnostics," *EJNMMI radiopharmacy and chemistry*, vol. 1, no. 1, pp. 1–5, 2017.

[35] "Cancer of the Prostate - Cancer Stat Facts." Accessed: 2021-04-30.

[36] J. Griswold, D. Medvedev, J. Engle, R. Copping, J. Fitzsimmons, V. Radchenko, J. Cooley, M. Fassbender, D. Denton, K. Murphy, A. Owens, E. Birnbaum, K. John, F. Nortier, D. Stracener, L. Heilbronn, L. Mausner, and S. Mirzadeh, "Large scale accelerator production of 225Ac: Effective cross sections for 78–192MeV protons incident on 232Th targets," *Applied Radiation and Isotopes*, vol. 118, pp. 366–374, 2016.

[37] F. Kondev, E. McCutchan, B. Singh, and J. Tuli, "Nuclear data sheets for A= 227," *Nuclear Data Sheets*, vol. 132, pp. 257–354, 2016.

[38] R. Abergel, D. An, A. Lakes, J. Rees, and S. Gauny, "Actinium Biokinetics and Dosimetry: What is the Impact of Ac-227 in Accelerator-Produced Ac-225?," *Journal of Medical Imaging and Radiation Sciences*, vol. 50, no. 4, p. S93, 2019.

[39] C. Apostolidis, R. Molinet, J. McGinley, K. Abbas, J. Möllenbeck, and A. Morgenstern, "Cyclotron production of Ac-225 for targeted alpha therapy," *Applied Radiation and Isotopes*, vol. 62, no. 3, pp. 383–387, 2005.

[40] G. Melville, H. Meriarty, P. Metcalfe, T. Knittel, and B. Allen, "Production of Ac-225 for cancer therapy by photon-induced transmutation of Ra-226," *Applied Radiation and Isotopes*, vol. 65, no. 9, pp. 1014–1022, 2007.

[41] M. Salutsky and H. Kirby, "The radiochemistry of radium," tech. rep., Mound Lab., Miamisburg, Ohio (Grace (WR) and Co., Clarksville, Md ..., 1964.

[42] W. Diamond and C. Ross, "Actinium-225 Production with an Electron Accelerator," *arXiv preprint arXiv:2101.00291*, 2021.

[43] A. Sonzogni, "Nuclear Data Sheets for A = 134," *Nuclear Data Sheets*, vol. 103, no. 1, pp. 1 – 182, 2004.

[44] F. Tárkányi, F. Ditrói, S. Takács, A. Hermanne, and M. Baba, "Activation cross sections of proton and deuteron induced nuclear reactions on holmium and erbium, related to the production of 161Er and 160Er medical isotopes," *Applied Radiation and Isotopes*, vol. 115, pp. 262 – 266, 2016.

[45] L. Bernstein, D. Brown, A. Hurst, J. Kelly, F. Kondev, E. Mccutchan, C. Nesaraja, R. Slaybaugh, and A. Sonzogni, "Nuclear Data Needs and Capabilities for Applications," 10 2015.

[46] N. Otuka, E. Dupont, V. Semkova, B. Pritychenko, A. Blokhin, M. Aikawa, S. Babykina, M. Bossant, G. Chen, S. Dunaeva, R. Forrest, T. Fukahori, N. Furutachi, S. Ganesan, Z. Ge, O. Gritzay, M. Herman, S. Hlavač, K. Katõ, B. Lalremruata, Y. Lee, A. Makinaga, K. Matsumoto, M. Mikhaylyukova, G. Pikulina, V. Pronyaev, A. Saxena, O. Schwerer, S. Simakov, N. Soppera, R. Suzuki, S. Takács, X. Tao, S. Taova, F. Tárkányi, V. Varlamov, J. Wang, S. Yang, V. Zerkin, and Y. Zhuang, "Towards a More Complete and Accurate Experimental Nuclear Reaction Data Library (EXFOR): International Collaboration Between Nuclear Reaction Data Centres (NRDC)," *Nuclear Data Sheets*, vol. 120, pp. 272 – 276, 2014.

[47] W. Hauser and H. Feshbach, "The Inelastic Scattering of Neutrons," *Phys. Rev.*, vol. 87, pp. 366–373, jul 1952.

[48] R. A. Boll, D. Malkemus, and S. Mirzadeh, "Production of actinium-225 for alpha particle mediated radioimmunotherapy," *Applied Radiation and Isotopes*, vol. 62, no. 5, pp. 667–679, 2005.

[49] A. K. Jain, S. Singh, S. Kumar, and J. K. Tuli, "Nuclear Data Sheets for A = 221," *Nuclear Data Sheets*, vol. 108, no. 4, pp. 883 – 922, 2007.

[50] F. Kondev, E. McCutchan, B. Singh, K. Banerjee, S. Bhattacharya, A. Chakraborty, S. Garg, N. Jovancevic, S. Kumar, S. Rathi, T. Roy, J. Lee, and R. Shearman, "Nuclear Data Sheets for A=217," *Nuclear Data Sheets*, vol. 147, pp. 382 – 458, 2018.

[51] J. Chen and F. Kondev, "Nuclear Data Sheets for A = 209," *Nuclear Data Sheets*, vol. 126, pp. 373 – 546, 2015.

[52] D. A. Mulford, D. A. Scheinberg, and J. G. Jurcic, "The Promise of Targeted alpha-Particle Therapy," *Journal of Nuclear Medicine*, vol. 46, pp. 199S———204S, jan 2005.

[53] C. Apostolidis, R. Molinet, G. Rasmussen, and A. Morgenstern, "Production of Ac-225 from Th-229 for Targeted alpha Therapy," *Analytical Chemistry*, vol. 77, no. 19, pp. 6288–6291, 2005. PMID: 16194090.

[54] A. J. Koning and D. Rochman, "Modern Nuclear Data Evaluation with the TALYS Code System," *Nuclear Data Sheets*, vol. 113, pp. 2841–2934, dec 2012.

[55] M. Herman, R. Capote, B. Carlson, P. Obložinský, M. Sin, A. Trkov, H. Wienke, and V. Zerkin, "EMPIRE: Nuclear Reaction Model Code System for Data Evaluation," *Nuclear Data Sheets*, vol. 108, no. 12, pp. 2655 – 2715, 2007. Special Issue on Evaluations of Neutron Cross Sections.

[56] S. A. Graves, P. A. Ellison, T. E. Barnhart, H. F. Valdovinos, E. R. Birnbaum, F. M. Nortier, R. J. Nickles, and J. W. Engle, "Nuclear excitation functions of proton-induced reactions (Ep=35–90MeV) from Fe, Cu, and Al," *Nuclear Instruments and Methods in Physics Research Section B: Beam Interactions with Materials and Atoms*, vol. 386, pp. 44 – 53, 2016.

[57] A. S. Voyles, L. A. Bernstein, E. R. Birnbaum, J. W. Engle, S. A. Graves, T. Kawano, A. M. Lewis, and F. M. Nortier, "Excitation functions for (p,x) reactions of niobium in the energy range of Ep = 40–90 MeV," *Nuclear Instruments and Methods in Physics Research Section B: Beam Interactions with Materials and Atoms*, vol. 429, pp. 53 – 74, 2018.

[58] IAEA, "Charged Particle Cross-Section Database for Medical Radioisotope Production: Diagnostic Radioisotopes and Monitor Reactions Final Report of a Co-ordinated Research Project," *International Atomic Energy Agency, Vienna, Austria*, may 2001.

[59] J. F. Ziegler, M. Ziegler, and J. Biersack, "SRIM – The stopping and range of ions in matter (2010)," *Nuclear Instruments and Methods in Physics Research Section B: Beam Interactions with Materials and Atoms*, vol. 268, no. 11, pp. 1818 – 1823, 2010. 19th International Conference on Ion Beam Analysis.

[60] M. J. Berger, J. H. Hubbell, S. M. Seltzer, J. Chang, J. S. Coursey, R. Sukumar, D. S. Zucker, and K. Olsen, "XCOM: Photon cross section database (version 1.5)," 2010.

[61] M. K. Covo, R. Albright, B. Ninemire, M. Johnson, A. Hodgkinson, T. Loew, J. Benitez, D. Todd, D. Xie, T. Perry, L. Phair, L. Bernstein, J. Bevins, J. Brown, B. Goldblum, M. Harasty, K. Harrig, T. Laplace, E. Matthews, A. Bushmaker, D. Walker, V. Oklejas, A. Hopkins, D. Bleuel, J. Chen, and S. Cronin, "The 88-Inch Cyclotron: A one-stop facility for electronics radiation and detector testing," *Measurement*, vol. 127, pp. 580 – 587, 2018.

[62] B. Singh, A. A. Rodionov, and Y. L. Khazov, "Nuclear Data Sheets for A = 135," *Nuclear Data Sheets*, vol. 109, no. 3, pp. 517 – 698, 2008.

[63] J. T. Morrell, "NPAT: Nuclear physics analysis tools," 2019–. [Online; accessed June 25, 2019.].

[64] G. Knoll, *Radiation Detection and Measurement*. John Wiley & Sons, Inc., 1999.

[65] H. Bateman, "The solution of a system of differential equations occurring in the theory of radioactive transformations," *In Proc. Campridge Philos. Soc.*, vol. 15, pp. 423 – 427, 1910.

[66] A. Hermanne, A. V. Ignatyuk, R. Capote, B. V. Carlson, J. W. Engle, M. A. Kellett, T. Kibédi, G. Kim, F. G. Kondev, M. Hussain, O. Lebeda, A. Luca, Y. Nagai, H. Naik, A. L. Nichols, F. M. Nortier, S. V. Suryanarayana, S. Takács, F. T. Tárkányi, and M. Verpelli, "Reference Cross Sections for Charged-particle Monitor Reactions," *Nuclear Data Sheets*, vol. 148, pp. 338–382, feb 2018.

[67] J.T. Goorley and M.R. James et. al., "Initial MCNP6 release Overview - MCNP6 version 1.0," *Los Alamos Report LA-UR-13-22934*, vol. 180, pp. 298–315, dec 2013.

[68] M. Blann and J. Bisplinghoff, "Code ALICE/LIVERMORE 82," 11 1982.

[69] F. Tárkányi, A. Hermanne, F. Ditrói, and S. Takács, "Activation cross section data of proton induced nuclear reactions on lanthanum in the 34–65 MeV energy range and application for production of medical radionuclides," *Journal of Radioanalytical and Nuclear Chemistry*, vol. 312, pp. 691–704, jun 2017.

[70] R. Alt, G. Beyer, V. Morozov, H. Musiol, T. Numinov, H. Tyrroff, H. Strusny, Z. Usmanova, V. Fominykh, H. Fuya, *et al.*, "On the 135Pr-135Ce Decay Scheme," *Izv. Akad. Nauk SSSR, Ser. Fiz.*, vol. 36, p. 744, 1972.

[71] R. Ma, E. S. Paul, D. B. Fossan, Y. Liang, N. Xu, R. Wadsworth, I. Jenkins, and P. J. Nolan, "Rotational bands in ^{135}ce: Collective prolate and oblate rotation," *Phys.Rev.*, vol. C41, p. 2624, 1990.

[72] H. C. Jain, S. Lakshmi, and P. K. Joshi, "Identification of chiral bands in ^{135}ce," in *Proc.Nuclei at the Limits*, 2005.

[73] D. Brink, "Individual particle and collective aspects of the nuclear photoeffect," *Nuclear Physics*, vol. 4, pp. 215 – 220, 1957.

[74] A. J. Koning and J. P. Delaroche, "Local and global nucleon optical models from 1 keV to 200 MeV," *Nuclear Physics A*, vol. 713, no. 3, pp. 231–310, 2003.

[75] Y. Khazov, A. Rodionov, and F. Kondev, "Nuclear Data Sheets for A = 133," *Nuclear Data Sheets*, vol. 112, no. 4, pp. 855 – 1113, 2011.

[76] A. Grütter, "Excitation functions for radioactive isotopes produced by proton bombardment of Cu and Al in the energy range of 16 to 70 MeV," *Nuclear Physics A*, vol. 383, no. 1, pp. 98 – 108, 1982.

[77] V. Aleksandrov, M. Semyonova, and V. Semyonov, "Excitation functions for radionuclides produced by (p, x) reactions of copper and nickel," *Atomnaya Energiya*, vol. 62, p. 411, 1987.

[78] S. Mills, G. Steyn, and F. Nortier, "Experimental and theoretical excitation functions of radionuclides produced in proton bombardment of copper up to 200 MeV," *International Journal of Radiation Applications and Instrumentation. Part A. Applied Radiation and Isotopes*, vol. 43, no. 8, pp. 1019 – 1030, 1992.

[79] R. Michel, R. Bodemann, H. Busemann, R. Daunke, M. Gloris, H.-J. Lange, B. Klug, A. Krins, I. Leya, M. Lüpke, S. Neumann, H. Reinhardt, M. Schnatz-Büttgen, U. Herpers, T. Schiekel, F. Sudbrock, B. Holmqvist, H. Condé, P. Malmborg, M. Suter, B. Dittrich-Hannen, P.-W. Kubik, H.-A. Synal, and D. Filges, "Cross sections for the production of residual nuclides by low- and medium-energy protons from the target elements C, N, O, Mg, Al, Si, Ca, Ti, V, Mn, Fe, Co, Ni, Cu, Sr, Y, Zr, Nb, Ba and Au," *Nuclear Instruments and Methods in Physics Research Section B: Beam Interactions with Materials and Atoms*, vol. 129, no. 2, pp. 153 – 193, 1997.

[80] M. Shahid, K. Kim, H. Naik, M. Zaman, S.-C. Yang, and G. Kim, "Measurement of excitation functions in proton induced reactions on natural copper from their threshold to 43MeV," *Nuclear Instruments and Methods in Physics Research Section B: Beam Interactions with Materials and Atoms*, vol. 342, pp. 305 – 313, 2015.

[81] E. Garrido, C. Duchemin, A. Guertin, F. Haddad, N. Michel, and V. Métivier, "New excitation functions for proton induced reactions on natural titanium, nickel and copper up to 70MeV," *Nuclear Instruments and Methods in Physics Research Section B: Beam Interactions with Materials and Atoms*, vol. 383, pp. 191 – 212, 2016.

[82] E. Browne and J. Tuli, "Nuclear Data Sheets for A = 137," *Nuclear Data Sheets*, vol. 108, no. 10, pp. 2173 – 2318, 2007.

[83] P. K. Joshi, B. Singh, S. Singh, and A. K. Jain, "Nuclear Data Sheets for A = 139," *Nuclear Data Sheets*, vol. 138, pp. 1 – 292, 2016.

[84] Y. Khazov, A. Rodionov, S. Sakharov, and B. Singh, "Nuclear Data Sheets for A=132," *Nuclear Data Sheets*, vol. 104, no. 3, pp. 497 – 790, 2005.

[85] K. Zuber and B. Singh, "Nuclear Data Sheets for A = 61," *Nuclear Data Sheets*, vol. 125, pp. 1 – 200, 2015.

[86] A. L. Nichols, B. Singh, and J. K. Tuli, "Nuclear Data Sheets for A = 62," *Nuclear Data Sheets*, vol. 113, no. 4, pp. 973 – 1114, 2012.

[87] B. Erjun and H. Junde, "Nuclear Data Sheets for A = 63," *Nuclear Data Sheets*, vol. 92, no. 1, pp. 147 – 252, 2001.

[88] C. D. Nesaraja, S. D. Geraedts, and B. Singh, "Nuclear Data Sheets for A = 58," *Nuclear Data Sheets*, vol. 111, no. 4, pp. 897 – 1092, 2010.

[89] M. S. Basunia, "Nuclear Data Sheets for A = 22," *Nuclear Data Sheets*, vol. 127, pp. 69 – 190, 2015.

[90] R. Firestone, "Nuclear Data Sheets for A = 24," *Nuclear Data Sheets*, vol. 108, no. 11, pp. 2319 – 2392, 2007.

[91] M. S. Basunia, J. T. Morrell, M. S. Uddin, A. S. Voyles, C. D. Nesaraja, L. A. Bernstein, E. Browne, M. J. Martin, and S. M. Qaim, "Resolution of a discrepancy in the γ-ray emission probability from the β decay of $^{137}\mathrm{Ce}^{g}$," *Phys. Rev. C*, vol. 101, p. 064619, Jun 2020.

[92] "Isotope Production Facility." Accessed: 2021-04-30.

[93] M. A. Mosby, J. W. Engle, K. R. Jackman, F. M. Nortier, and E. R. Birnbaum, "Determination of spallation neutron flux through spectral adjustment techniques," *Nuclear Instruments and Methods in Physics Research Section B: Beam Interactions with Materials and Atoms*, vol. 381, pp. 29–33, 2016.

[94] L. A. Bernstein, D. A. Brown, A. J. Koning, B. T. Rearden, C. E. Romano, A. A. Sonzogni, A. S. Voyles, and W. Younes, "Our future nuclear data needs," *Annual Review of Nuclear and Particle Science*, vol. 69, pp. 109–136, 2019.

[95] K. Ehrlich and A. Möslang, "IFMIF – An international fusion materials irradiation facility," *Nuclear Instruments and Methods in Physics Research Section B: Beam Interactions with Materials and Atoms*, vol. 139, no. 1, pp. 72–81, 1998.

[96] J. W. Norbury and T. C. Slaba, "Space radiation accelerator experiments–the role of neutrons and light ions," *Life Sciences in Space Research*, vol. 3, pp. 90–94, 2014.

[97] G. Potel, G. Perdikakis, B. Carlson, M. Atkinson, W. Dickhoff, J. Escher, M. Hussein, J. Lei, W. Li, A. Macchiavelli, *et al.*, "Toward a complete theory for predicting inclusive deuteron breakup away from stability," *The European Physical Journal A*, vol. 53, no. 9, pp. 1–16, 2017.

[98] Q. Ducasse, B. Jurado, M. Aïche, P. Marini, L. Mathieu, A. Görgen, M. Guttormsen, A.-C. Larsen, T. Tornyi, J. Wilson, *et al.*, "Investigation of the U238(d,p) surrogate reaction via the simultaneous measurement of γ-decay and fission probabilities," *Physical Review C*, vol. 94, no. 2, p. 024614, 2016.

[99] J. R. Oppenheimer, "The disintegration of the deuteron by impact," *Physical Review*, vol. 47, no. 11, p. 845, 1935.

[100] A. Helmholz, E. M. McMillan, and D. C. Sewell, "Angular Distribution of Neutrons from Targets Bombarded by 190-Mev Deuterons," *Physical Review*, vol. 72, no. 11, p. 1003, 1947.

[101] S. Dancoff, "Disintegration of the Deuteron in Flight," *Physical Review*, vol. 72, no. 11, p. 1017, 1947.

[102] R. Serber, "The production of high energy neutrons by stripping," *Physical Review*, vol. 72, no. 11, p. 1008, 1947.

[103] S. Nakayama, H. Kouno, Y. Watanabe, O. Iwamoto, and K. Ogata, "Theoretical model analysis of (d, xn) reactions on Be9 and C12 at incident energies up to 50 MeV," *Physical Review C*, vol. 94, no. 1, p. 014618, 2016.

[104] M. Ichimura, N. Austern, and C. Vincent, "Equivalence of post and prior sum rules for inclusive breakup reactions," *Physical Review C*, vol. 32, no. 2, p. 431, 1985.

[105] T. Udagawa and T. Tamura, "Derivation of breakup-fusion cross sections from the optical theorem," *Physical Review C*, vol. 24, no. 3, p. 1348, 1981.

[106] C. Kalbach, "Phenomenological model for light-projectile breakup," *Physical Review C*, vol. 95, no. 1, p. 014606, 2017.

[107] M. Avrigeanu and V. Avrigeanu, "Additive empirical parametrization and microscopic study of deuteron breakup," *Physical Review C*, vol. 95, no. 2, p. 024607, 2017.

[108] S. Nakayama, O. Iwamoto, Y. Watanabe, and K. Ogata, "JENDL/DEU-2020: deuteron nuclear data library for design studies of accelerator-based neutron sources," *Journal of Nuclear Science and Technology*, pp. 1–17, 2021.

[109] A. Arcones, D. W. Bardayan, T. C. Beers, L. A. Bernstein, J. C. Blackmon, B. Messer, B. A. Brown, E. F. Brown, C. R. Brune, A. E. Champagne, *et al.*, "White paper on nuclear astrophysics and low energy nuclear physics Part 1: Nuclear astrophysics," *Progress in Particle and Nuclear Physics*, vol. 94, pp. 1–67, 2017.

[110] J.-P. Meulders, P. Leleux, P. Macq, C. Pirart, and G. Valenduc, "Intensity measurements and shielding of a fast-neutron beam for biological and medical applications," *Nuclear Instruments and Methods*, vol. 126, no. 1, pp. 81–85, 1975.

[111] P. Pereslavtsev, U. Fischer, S. Simakov, and M. Avrigeanu, "Evaluation of d+ ^{6,7}Li data for deuteron incident energies up to 50 MeV," *Nuclear Instruments and Methods in Physics Research Section B: Beam Interactions with Materials and Atoms*, vol. 266, no. 16, pp. 3501–3512, 2008.

[112] A. Koning and J. Delaroche, "Local and global nucleon optical models from 1 keV to 200 MeV," *Nuclear Physics A*, vol. 713, no. 3-4, pp. 231–310, 2003.

[113] C. Kalbach, "Systematics of continuum angular distributions: Extensions to higher energies," *Physical Review C*, vol. 37, no. 6, p. 2350, 1988.

[114] C. Kalbach and F. Mann, "Phenomenology of continuum angular distributions. I. Systematics and parametrization," *Physical Review C*, vol. 23, no. 1, p. 112, 1981.

[115] M. Cronqvist, S. Mattsson, M. Rydehell, and Ö. Skeppstedt, "Moving source parametrization of neutron spectra produced in (α, xn) reactions," *Physica Scripta*, vol. 42, no. 4, p. 400, 1990.

[116] W. Hauser and H. Feshbach, "The inelastic scattering of neutrons," *Physical review*, vol. 87, no. 2, p. 366, 1952.

[117] M. Blann, "Hybrid model for pre-equilibrium decay in nuclear reactions," *Physical Review Letters*, vol. 27, no. 6, p. 337, 1971.

[118] M. Paul, M. Tessler, M. Friedman, S. Halfon, T. Palchan, L. Weissman, A. Arenshtam, D. Berkovits, Y. Eisen, I. Eliahu, *et al.*, "Reactions along the astrophysical s-process path and prospects for neutron radiotherapy with the Liquid-Lithium Target (LiLiT) at the Soreq Applied Research Accelerator Facility (SARAF)," *The European Physical Journal A*, vol. 55, no. 3, pp. 1–29, 2019.

[119] K. Harrig, B. Goldblum, J. Brown, D. Bleuel, L. Bernstein, J. Bevins, M. Harasty, T. Laplace, and E. Matthews, "Neutron spectroscopy for pulsed beams with frame overlap using a double time-of-flight technique," *Nuclear Instruments and Methods*

in Physics Research Section A: Accelerators, Spectrometers, Detectors and Associated Equipment, vol. 877, pp. 359–366, 2018.

[120] M. Saltmarsh, C. Ludemann, C. Fulmer, and R. Styles, "Characteristics of an intense neutron source based on the d+ Be reaction," *Nuclear Instruments and Methods*, vol. 145, no. 1, pp. 81–90, 1977.

[121] G. Schweimer, "Fast neutron production with 54 MeV deuterons," *Nuclear Physics A*, vol. 100, no. 3, pp. 537–544, 1967.

[122] K. Weaver, J. Anderson, H. Barschall, and J. Davis, "Neutron spectra from deuteron bombardment of D, Li, Be, and C," *Nuclear Science and Engineering*, vol. 52, no. 1, pp. 35–45, 1973.

[123] J. Brown, B. L. Goldblum, T. Laplace, K. Harrig, L. Bernstein, D. Bleuel, W. Younes, D. Reyna, E. Brubaker, and P. Marleau, "Proton light yield in organic scintillators using a double time-of-flight technique," *Journal of Applied Physics*, vol. 124, no. 4, p. 045101, 2018.

[124] A. Trkov, P. J. Griffin, S. Simakov, L. R. Greenwood, K. I. Zolotarev, R. Capote, D. L. Aldama, V. Chechev, C. Destouches, A. Kahler, *et al.*, "IRDFF-II: a new neutron metrology library," *Nuclear Data Sheets*, vol. 163, pp. 1–108, 2020.

[125] D. Rochman, A. J. Koning, J. C. Sublet, M. Fleming, E. Bauge, S. Hilaire, P. Romain, B. Morillon, H. Duarte, S. Goriely, *et al.*, "The TENDL library: Hope, reality and future," in *EPJ web of conferences*, vol. 146, p. 02006, EDP Sciences, 2017.

[126] J. H. Hubbell and S. M. Seltzer, "Tables of X-ray mass attenuation coefficients and mass energy-absorption coefficients 1 keV to 20 MeV for elements Z= 1 to 92 and 48 additional substances of dosimetric interest," tech. rep., National Inst. of Standards and Technology-PL, Gaithersburg, MD (United States, 1995.

[127] J. T. Morrell, "Curie: A python toolkit to aid in the analysis of experimental nuclear data," 2019–. [Online; accessed April 25, 2021.].

[128] "MDPP-16 Applications." [Online; accessed April 25, 2021.].

[129] "EJ-301, EJ-309 - Neutron/Gamma PSD Liquid Scintillators." Accessed: 2021-04-30.

[130] A. Voyles, M. Basunia, J. Batchelder, J. Bauer, T. Becker, L. Bernstein, E. Matthews, P. Renne, D. Rutte, M. Unzueta, *et al.*, "Measurement of the 64Zn, 47Ti(n,p) cross

sections using a DD neutron generator for medical isotope studies," *Nuclear Instruments and Methods in Physics Research Section B: Beam Interactions with Materials and Atoms*, vol. 410, pp. 230–239, 2017.

[131] J. Chen, B. Singh, and J. A. Cameron, "Nuclear data sheets for A= 44," *Nuclear Data Sheets*, vol. 112, no. 9, pp. 2357–2495, 2011.

[132] S.-C. Wu, "Nuclear data sheets for A= 46," *Nuclear Data Sheets*, vol. 91, no. 1, pp. 1–116, 2000.

[133] T. Burrows, "Nuclear data sheets for A= 47," *Nuclear Data Sheets*, vol. 108, no. 5, pp. 923–1056, 2007.

[134] T. Burrows, "Nuclear data sheets for A= 48," *Nuclear Data Sheets*, vol. 107, no. 7, pp. 1747–1922, 2006.

[135] M. Bhat, "Nuclear data sheets for A= 57," *Nuclear Data Sheets*, vol. 85, no. 3, pp. 415–536, 1998.

[136] B. Singh, "Nuclear data sheets for A= 64," *Nuclear Data Sheets*, vol. 108, no. 2, pp. 197–364, 2007.

[137] E. Browne and J. Tuli, "Nuclear data sheets for A= 65," *Nuclear Data Sheets*, vol. 111, no. 9, pp. 2425–2553, 2010.

[138] H. Junde, H. Xiaolong, and J. Tuli, "Nuclear data sheets for A= 67," *Nuclear data sheets*, vol. 106, no. 2, pp. 159–250, 2005.

[139] T. Johnson and W. Kulp, "Nuclear data sheets for a= 87," *Nuclear Data Sheets*, vol. 129, pp. 1–190, 2015.

[140] G. Mukherjee and A. Sonzogni, "Nuclear data sheets for A= 88," *Nuclear Data Sheets*, vol. 105, no. 2, pp. 419–556, 2005.

[141] B. Singh, "Nuclear data sheets for A= 89," *Nuclear Data Sheets*, vol. 85, no. 1, pp. 1–170, 1998.

[142] J. Blachot, "Nuclear data sheets for A= 111," *Nuclear Data Sheets*, vol. 77, no. 2, pp. 299–432, 1996.

[143] J. Blachot, "Nuclear data sheets for A= 113," *Nuclear Data Sheets*, vol. 111, no. 6, pp. 1471–1618, 2010.

[144] J. Blachot, "Nuclear data sheets for A= 114," *Nuclear Data Sheets*, vol. 113, no. 2, pp. 515–714, 2012.

[145] J. Blachot, "Nuclear data sheets for a= 115," *Nuclear Data Sheets*, vol. 113, no. 10, pp. 2391–2535, 2012.

[146] N. Pfannkuchen, N. Bausbacher, S. Pektor, M. Miederer, and F. Rosch, "In vivo evaluation of [225Ac] Ac-DOTAZOL for α-therapy of bone metastases," *Current radiopharmaceuticals*, vol. 11, no. 3, pp. 223–230, 2018.

[147] N. A. Thiele and J. J. Wilson, "Actinium-225 for targeted α therapy: Coordination chemistry and current chelation approaches," *Cancer biotherapy & radiopharmaceuticals*, vol. 33, no. 8, pp. 336–348, 2018.

[148] C. Kratochwil, F. L. Giesel, M. Stefanova, M. Benešová, M. Bronzel, A. Afshar-Oromieh, W. Mier, M. Eder, K. Kopka, and U. Haberkorn, "PSMA-targeted radionuclide therapy of metastatic castration-resistant prostate cancer with 177Lu-labeled PSMA-617," *Journal of Nuclear Medicine*, vol. 57, no. 8, pp. 1170–1176, 2016.

[149] L. O'Connor and J. Perkin, "Cross-sections for the reactions 226Ra(n,2n)225Ra and 226Ra(n,3n)224Ra with $14 \cdot$ 5 MeV neutrons," *Journal of Inorganic and Nuclear Chemistry*, vol. 13, no. 1-2, pp. 5–12, 1960.

[150] M. B. Chadwick, M. Herman, P. Obložinskỳ, M. E. Dunn, Y. Danon, A. Kahler, D. L. Smith, B. Pritychenko, G. Arbanas, R. Arcilla, *et al.*, "ENDF/B-VII. 1 nuclear data for science and technology: cross sections, covariances, fission product yields and decay data," *Nuclear data sheets*, vol. 112, no. 12, pp. 2887–2996, 2011.

[151] D. R. McAlister and E. P. Horwitz, "Selective separation of radium and actinium from bulk thorium target material on strong acid cation exchange resin from sulfate media," *Applied Radiation and Isotopes*, vol. 140, pp. 18–23, 2018.

[152] T. Mastren, V. Radchenko, A. Owens, R. Copping, R. Boll, J. R. Griswold, S. Mirzadeh, L. E. Wyant, M. Brugh, J. W. Engle, *et al.*, "Simultaneous separation of actinium and radium isotopes from a proton irradiated thorium matrix," *Scientific reports*, vol. 7, no. 1, pp. 1–7, 2017.

[153] G. J.-P. Deblonde, A. Ricano, and R. J. Abergel, "Ultra-selective ligand-driven separation of strategic actinides," *Nature communications*, vol. 10, no. 1, pp. 1–9, 2019.

[154] J. Fitzsimmons, B. Foley, B. Torre, M. Wilken, C. S. Cutler, L. Mausner, and D. Medvedev, "Optimization of Cation Exchange for the Separation of Actinium-225

from Radioactive Thorium, Radium-223 and Other Metals," *Molecules*, vol. 24, no. 10, p. 1921, 2019.

[155] R. Duffield, R. A. Schmitt, and R. Sharp, "Yield-mass Distributions in the Photofission of Radium and Other Heavy Elements," tech. rep., General Atomic Div., General Dynamics Corp., San Diego, Calif., 1958.

[156] V. Radchenko, J. W. Engle, J. J. Wilson, J. R. Maassen, F. M. Nortier, W. A. Taylor, E. R. Birnbaum, L. A. Hudston, K. D. John, and M. E. Fassbender, "Application of ion exchange and extraction chromatography to the separation of actinium from proton-irradiated thorium metal for analytical purposes," *Journal of Chromatography A*, vol. 1380, pp. 55–63, 2015.

[157] A. Adelmann, J. Alonso, L. Calabretta, A. Calanna, D. Campo, J. Yang, J. Kim, and S. Jeong, "Proposal for a high power deuteron cyclotron at RISP," *Proc. HIAT*, pp. 45–47, 2015.

[158] Y. Akovali, "Nuclear data sheets for A= 226," *Nuclear data sheets*, vol. 77, no. 2, pp. 433–470, 1996.

[159] M. S. Basunia, "Nuclear data sheets for A= 210," *Nuclear Data Sheets*, vol. 121, pp. 561–694, 2014.

[160] A. Artna-Cohen, "Nuclear data sheets for A= 228," *Nuclear Data Sheets*, vol. 80, no. 3, pp. 723–786, 1997.

[161] S. Singh, A. Jain, and J. K. Tuli, "Nuclear data sheets for A= 222," *Nuclear Data Sheets*, vol. 112, no. 11, pp. 2851–2886, 2011.

[162] S. Singh and B. Singh, "Nuclear data sheets for A= 224," *Nuclear Data Sheets*, vol. 130, pp. 127–182, 2015.

[163] A. K. Jain and B. Singh, "Nuclear data sheets for a= 218," *Nuclear Data Sheets*, vol. 107, no. 4, pp. 1027–1074, 2006.

[164] A. Artna-Cohen, "Nuclear Data Sheets for A= 216,220," *Nuclear Data Sheets*, vol. 80, no. 1, pp. 157–226, 1997.

[165] E. Browne, "Nuclear Data Sheets for A= 215,219,223,227,231," *Nuclear Data Sheets*, vol. 93, no. 4, pp. 763–1061, 2001.

[166] S.-C. Wu, "Nuclear data sheets for a= 214," *Nuclear Data Sheets*, vol. 110, no. 3, pp. 681–748, 2009.

[167] K. N. Kmak, D. A. Shaughnessy, and J. Vujic, "Measurement of the Th230(p,2n)Pa229 and Th230(p,3n)Pa228 reaction cross sections from 14.1 to 16.9 MeV," *Physical Review C*, vol. 103, no. 3, p. 034610, 2021.

[168] M. Rahman, B. Szpunar, and J. Szpunar, "The induced anisotropy in thermal conductivity of thorium dioxide and cerium dioxide," *Materials Research Express*, vol. 4, no. 7, p. 075512, 2017.

[169] L. A. Akhmedova-Azizova and I. M. Abdulagatov, "Thermal conductivity of aqueous CaCl 2 solutions at high temperatures and high pressures," *Journal of Solution Chemistry*, vol. 43, no. 3, pp. 421–444, 2014.

[170] P. Loboda, H. Kysla, S. Dub, and O. Karasevs' Ka, "Mechanical properties of the monocrystals of lanthanum hexaboride," *Materials Science*, vol. 45, no. 1, p. 108, 2009.

[171] C. Jost, J. R. Griswold, S. H. Bruffey, S. Mirzadeh, D. Stracener, and C. Williams, "Measurement of cross sections for the 232Th(p,4n)229Pa reaction at low proton energies," in *AIP conference proceedings*, vol. 1525, pp. 520–524, American Institute of Physics, 2013.

[172] R. Alvarez, "Managing the uranium-233 stockpile of the United States," *Science & Global Security*, vol. 21, no. 1, pp. 53–69, 2013.

[173] Y. Wu, "Overview of High Intensity Gamma-ray Source-Capabilities and Future Upgrades," in *2013 International Workshop on Polarized Sources, Targets and Polarimetry*, 2013.

[174] N. Mordasov, D. Ivashchenko, A. Chlenov, and A. Astakhov, "Simulation of methods for a rapid determination of the energy spectrum of bremsstrahlung from electron accelerators," *Technical physics*, vol. 49, no. 9, pp. 1213–1220, 2004.

[175] H. Koch and J. Motz, "Bremsstrahlung cross-section formulas and related data," *Reviews of modern physics*, vol. 31, no. 4, p. 920, 1959.

[176] L. Schiff, "Energy-angle distribution of thin target bremsstrahlung," *Physical review*, vol. 83, no. 2, p. 252, 1951.

[177] H. Bethe, L. Maximon, and F. Low, "Bremsstrahlung at High Energies," *Physical Review*, vol. 91, no. 2, p. 417, 1953.

[178] W. Heitler, "The Quantum Theory of Radiation," Oxford University Press, London, 1954.

[179] H. A. Bethe, "Moliere's theory of multiple scattering," *Physical review*, vol. 89, no. 6, p. 1256, 1953.

[180] T. Tabata and R. Ito, "A generalized empirical equation for the transmission coefficient of electrons," *Nuclear Instruments and Methods*, vol. 127, no. 3, pp. 429–434, 1975.

[181] H. Ferdinande, G. Knuyt, R. Van de Vijver, and R. Jacobs, "Numerical calculation of absolute forward thick-target bremsstrahlung spectra," *Nuclear Instruments and Methods*, vol. 91, no. 1, pp. 135–140, 1971.

[182] A. O'Dell Jr, C. Sandifer, R. Knowlen, and W. George, "Measurement of absolute thick-target bremsstrahlung spectra," *Nuclear Instruments and Methods*, vol. 61, no. 3, pp. 340–346, 1968.

[183] L. B. Levy, R. G. Waggener, W. D. McDavid, and W. H. Payne, "Experimental and calculated bremsstrahlung spectra from a 25-MeV linear accelerator and a 19-MeV betatron," *Medical physics*, vol. 1, no. 2, pp. 62–67, 1974.

[184] S. S. Dietrich and B. L. Berman, "Atlas of photoneutron cross sections obtained with monoenergetic photons," *Atomic Data and Nuclear Data Tables*, vol. 38, no. 2, pp. 199–338, 1988.

[185] R. B. Firestone, "The Origin of the Giant Dipole Resonance," *arXiv preprint arXiv:2009.03356*, 2020.

[186] A. Veyssiere, H. Beil, and R. Bergere, "Study of the photofission and photoneutron processes in the giant dipole resonance of ^{232}th, ^{238}u, and ^{237}np.," tech. rep., CEN, Saclay, France);(and others), 1973.

[187] J. Caldwell, E. Dowdy, B. Berman, R. Alvarez, and P. Meyer, "Giant resonance for the actinide nuclei: Photoneutron and photofission cross sections for U235, U236, U238, and Th232," *Physical Review C*, vol. 21, no. 4, p. 1215, 1980.

[188] M. B. Fox, A. S. Voyles, J. T. Morrell, L. A. Bernstein, A. M. Lewis, A. J. Koning, J. C. Batchelder, E. R. Birnbaum, C. S. Cutler, D. G. Medvedev, *et al.*, "Investigating high-energy proton-induced reactions on spherical nuclei: Implications for the preequilibrium exciton model," *Physical Review C*, vol. 103, no. 3, p. 034601, 2021.

Appendix A

HEIFER Breakup Target Design

Included below are additional schematics and photos of the target which was designed and manufactured for the experiment to measure the ^{226}Ra(n,2n) cross section. It has been given the nickname of the "HEIFER" target, as the High-Energy Irradiation Facility for Emerging Radionuclides. Not included in the drawings are the 4–6 mm of beryllium plates which served as the actual breakup target itself. The beryllium plates used in this experiment were approximately 2.5×2.5 cm squares, of approximately 2 mm thickness.

The HEIFER target served to securely mount these plates at the end of the beamline, provide a vacuum boundary, and provide cooling for the approximately 150 W of beam power that was being deposited in the target. Additionally, the HEIFER target held the radium capsule in close proximity, and had a machined recess close behind the capsule for the placement of neutron monitor foils. Once the target was securely fastened to the beamline, and the beamline was pumped down to vacuum levels (10^{-7}–10^{-6} torr), a chilled-water cooling plate was clamped on to the back. The target and mounting screws were composed of 6061-aluminum alloy, and the rubber o-ring used to provide the vacuum seal was a Buna-N composite.

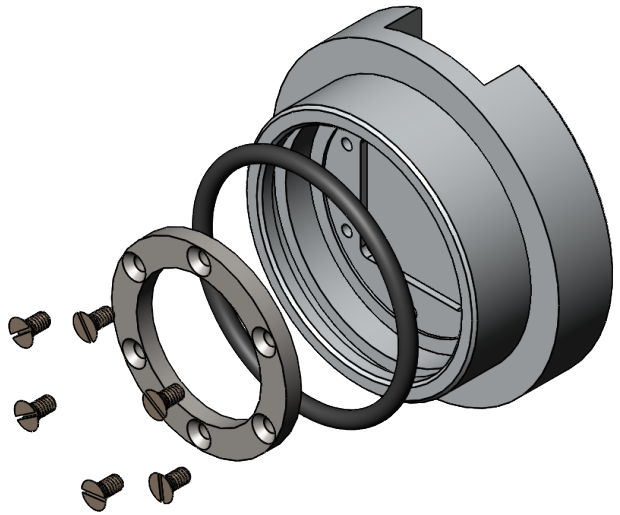

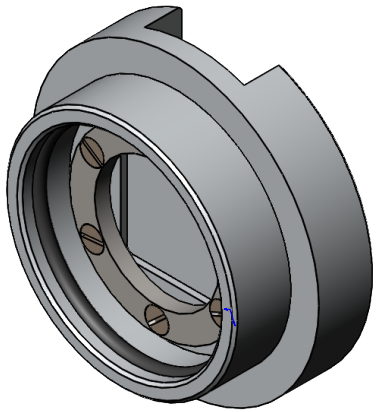

		UNLESS OTHERWISE SPECIFIED:		NAME	DATE
		DIMENSIONS ARE IN INCHES TOLERANCES: 0.002' FRACTIONAL ± ANGULAR: MACH ± BEND ± TWO PLACE DECIMAL ± THREE PLACE DECIMAL ±	DRAWN	JM	10/23
			CHECKED		
			ENG APPR.		
			MFG APPR.		
		INTERPRET GEOMETRIC TOLERANCING PER:	Q.A.		
		MATERIAL Aluminum	COMMENTS:		
NEXT ASSY	USED ON	FINISH			
APPLICATION		DO NOT SCALE DRAWING			

LBLN

TITLE:

Beamstop Assembly

SIZE	DWG. NO.	REV
A		

SCALE: 1:2 | SHEET 1 OF 4

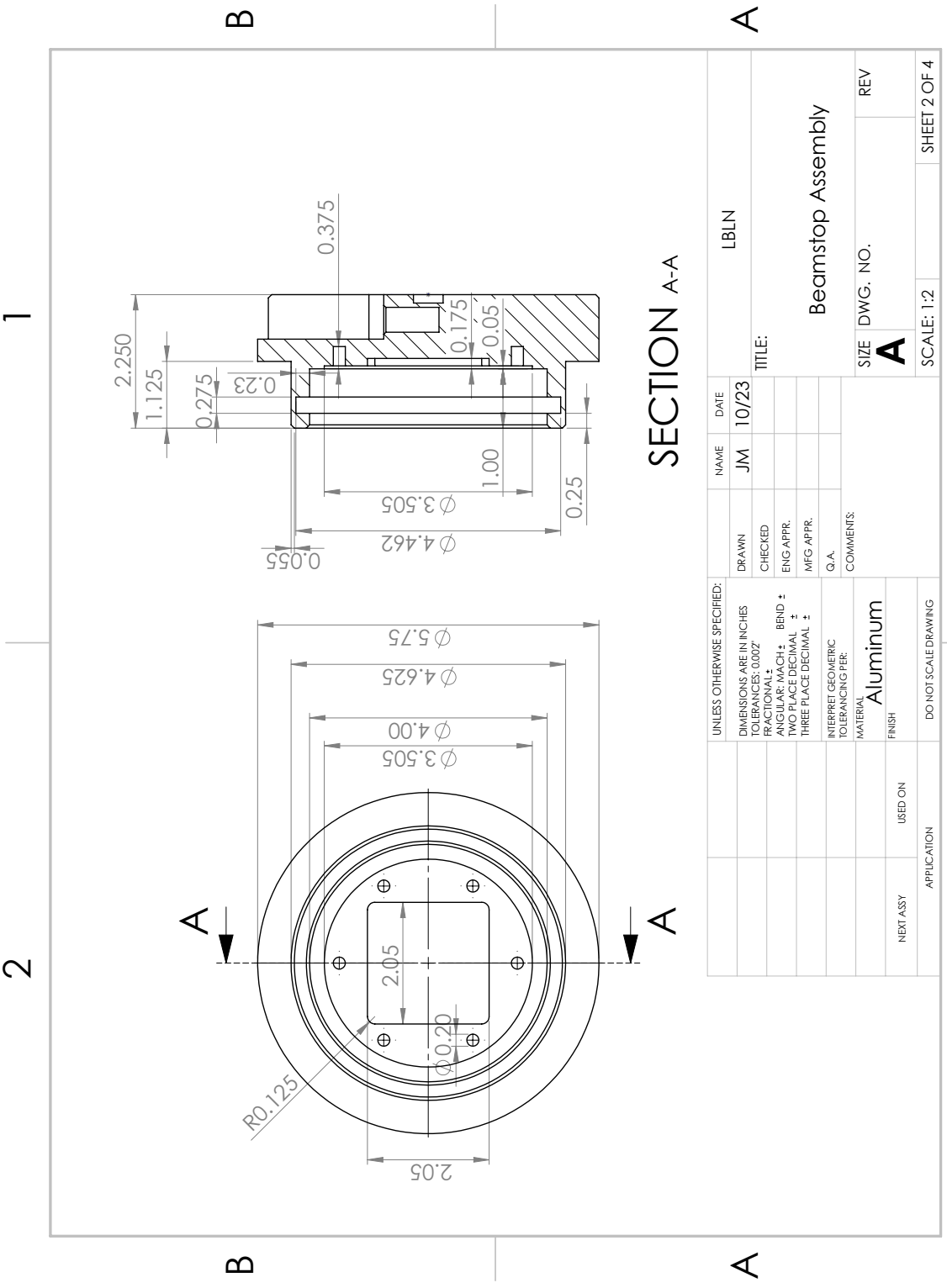

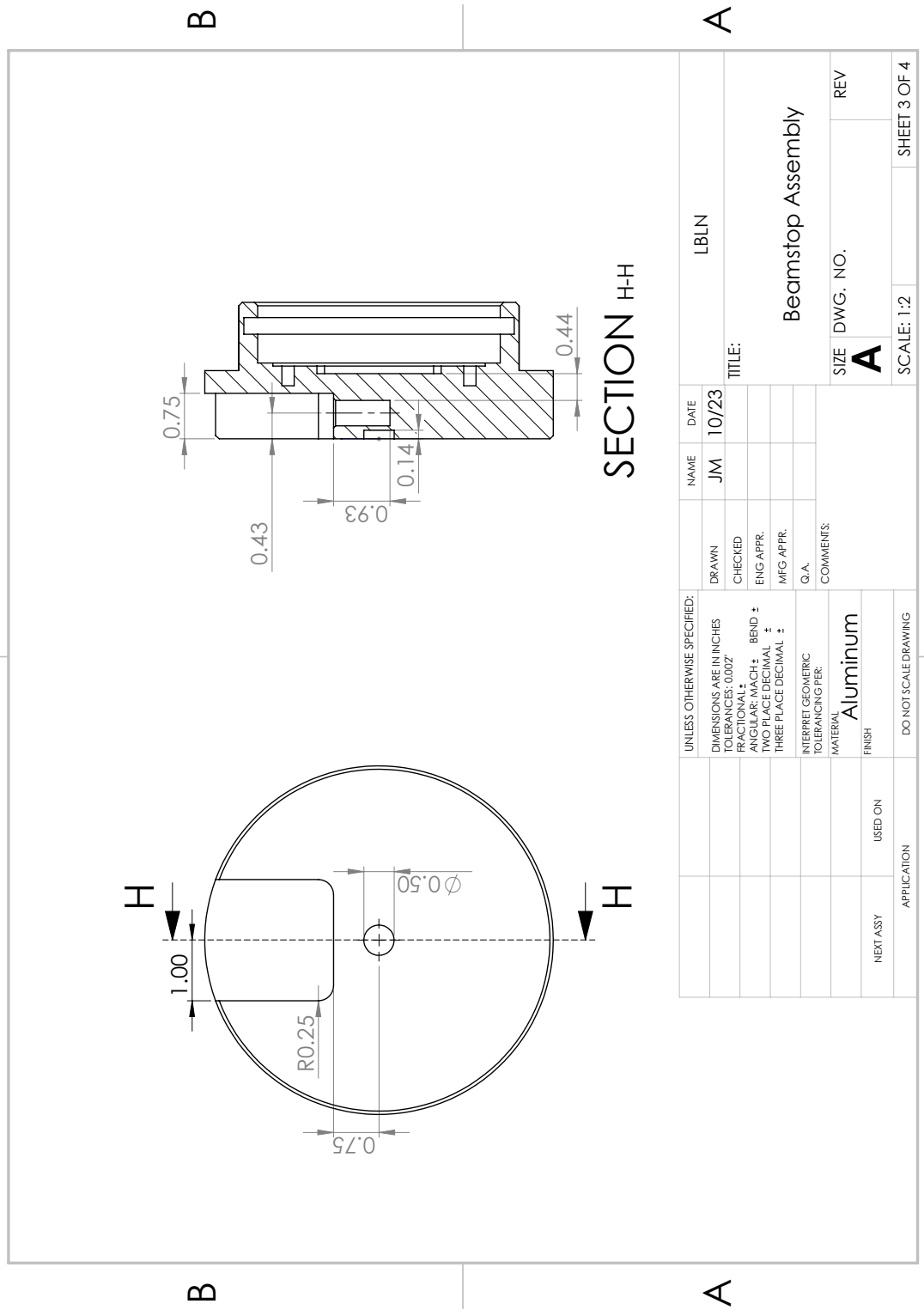
SECTION H-H
0.75
0.44
0.14
0.93
0.43
H
H
Ø0.50
1.00
R0.25
0.75
LBLN
Beamstop Assembly
SIZE A
DWG. NO.
REV
SCALE: 1:2
SHEET 3 OF 4
UNLESS OTHERWISE SPECIFIED:
DIMENSIONS ARE IN INCHES
TOLERANCES: 0.002"
FRACTIONAL ±
ANGULAR: MACH ± BEND ±
TWO PLACE DECIMAL ±
THREE PLACE DECIMAL ±
INTERPRET GEOMETRIC TOLERANCING PER:
MATERIAL Aluminum
FINISH
DO NOT SCALE DRAWING
DRAWN JM 10/23
CHECKED
ENG APPR.
MFG APPR.
Q.A.
COMMENTS:
NEXT ASSY
USED ON
APPLICATION
SOLIDWORKS Educational Product. For Instructional Use Only.

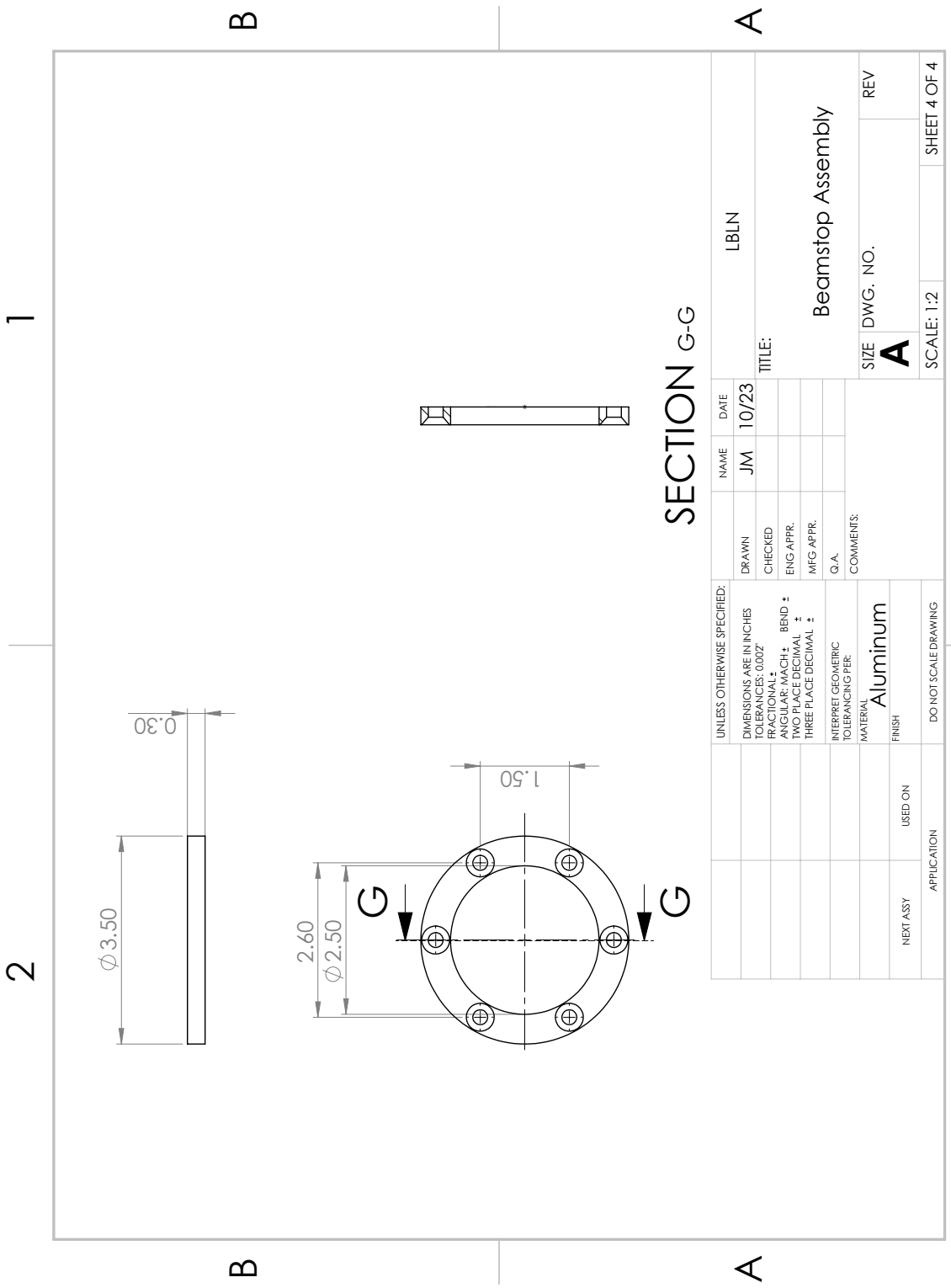
SECTION G-G
0.30
1.50
2.60
Ø2.50
Ø3.50
G
G
LBLN
Beamstop Assembly
SIZE A
DWG. NO.
REV
SCALE: 1:2
SHEET 4 OF 4
UNLESS OTHERWISE SPECIFIED:
DIMENSIONS ARE IN INCHES
TOLERANCES: 0.002"
FRACTIONAL ±
ANGULAR: MACH ± BEND ±
TWO PLACE DECIMAL ±
THREE PLACE DECIMAL ±
INTERPRET GEOMETRIC TOLERANCING PER:
MATERIAL Aluminum
FINISH
DO NOT SCALE DRAWING
DRAWN JM 10/23
CHECKED
ENG APPR.
MFG APPR.
Q.A.
COMMENTS:
NAME
DATE
TITLE:
NEXT ASSY
USED ON
APPLICATION
SOLIDWORKS Educational Product. For Instructional Use Only.

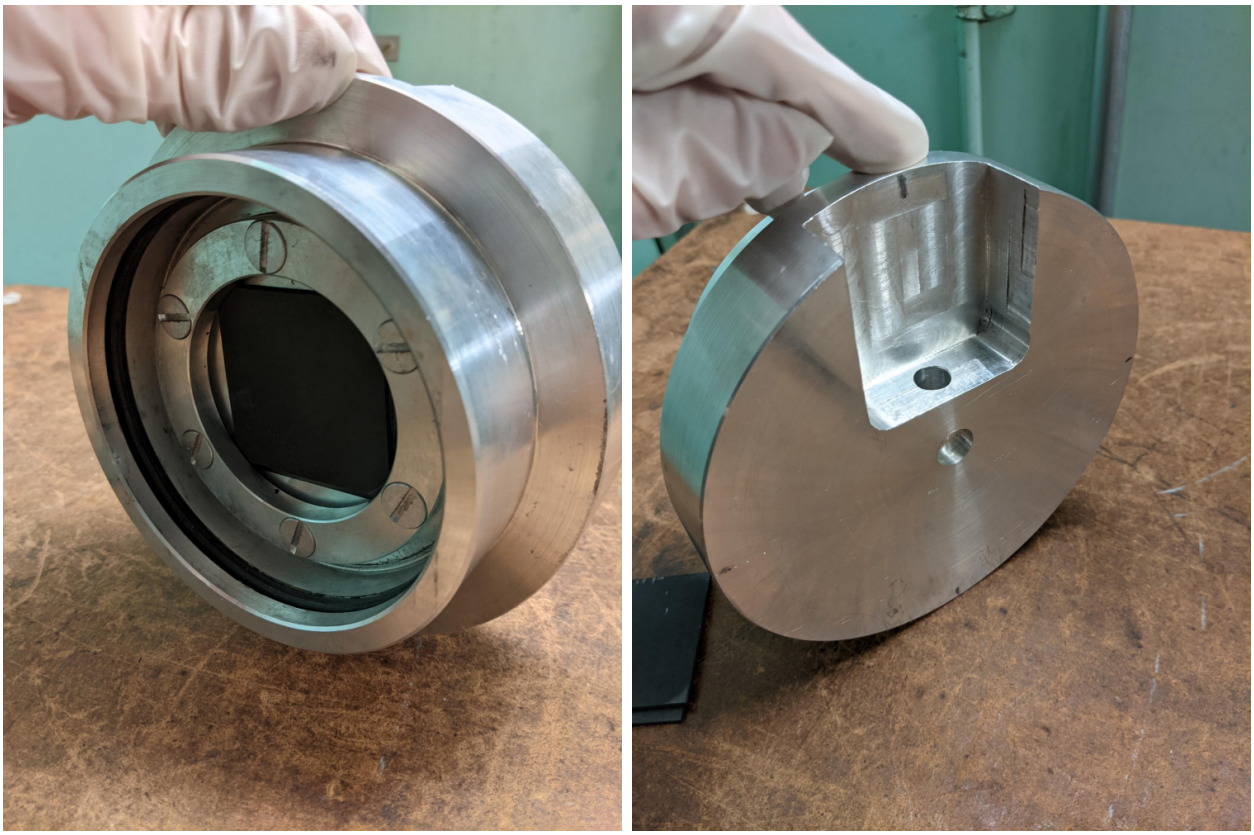

Figure A.1: Photos of the HEIFER breakup target. Graphite targets are loaded in these photos, however beryllium was used in the ^{225}Ac production experiment.

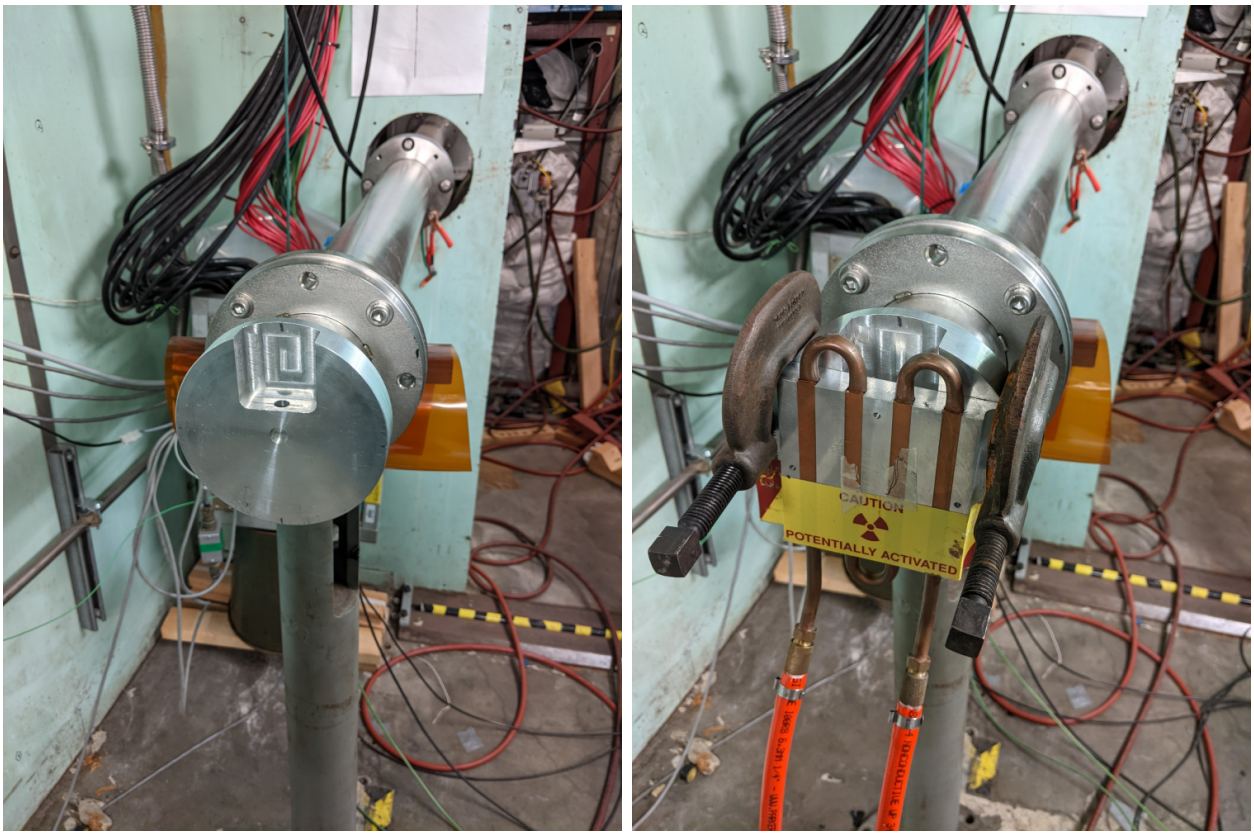

Figure A.2: Photos of the HEIFER target mounted onto the beam pipe, with and without the clamp-on water cooler.